AD-A284 826

AFIT/DS/ENP/94-03

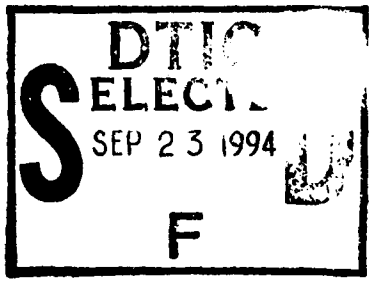

A THREE REGION ANALYSIS OF A BOUNDED PLASMA USING PARTICLE IN CELL AND FLUID TECHNIQUES

DISSERTATION

Don F. Nichols, Captain, USAF

AFIT/DS/ENP/94-03

2185

94-30536

DTIC QUALITY INSPECTED 3

Approved for Public Release; Distribution Unlimited

94 9 22 063

The views expressed in this dissertation are those of the author and do not reflect the official policy or position of the Department of Defense or the U.S. Government.

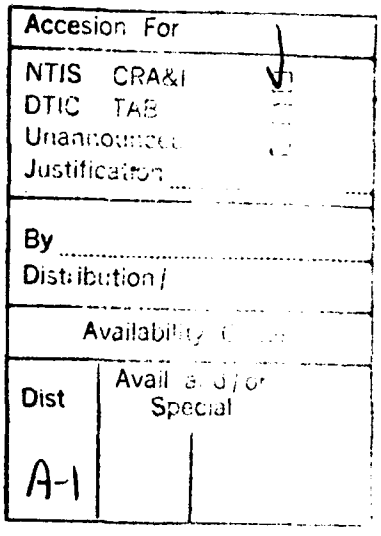

AFIT/DS/ENP/94-03

A THREE REGION ANALYSIS OF A BOUNDED PLASMA USING PARTICLE IN CELL AND FLUID TECHNIQUES

DISSERTATION

Presented to the Faculty of the School of Engineering

of the Air Force Institute of Technology

Air University

In Partial Fulfillment of the

Requirements for the Degree of

Doctor of Philosophy

Don F. Nichols, B.S., M.S.

Captain, USAF

September 1994

Approved for Public Release; Distribution Unlimited

AFIT/DS/ENP/94-03

A THREE REGION ANALYSIS OF A BOUNDED PLASMA USING PARTICLE IN CELL AND FLUID TECHNIQUES

Don F. Nichols, B.S., M.S.
Captain, USAF

Approved:

Dr. William Bailey	30 Aug 94
Dr. Alan Garscadden	19th August 1994
Dr. Denis E. Beller	21 aug 94
Dr. Dennis W. Quinn	31 AUG 94
Dr. Thomas Mahefkey	19 Aug '94

Accepted:

J. S. Przemieniecki 31 Aug 94
J. S. Przemieniecki, Senior Dean

Preface

We need power. The future of near earth and distant space utilization is only just begun; as we reach out into our solar system and beyond, our need for compact, lightweight power systems will quickly outstrip available technology. There are a number of promising technologies waiting in the wings, but none at a state of readiness permitting its selection as the power technology of choice -- there is still too much to be understood about performance and optimization.

One emerging technology is thermionic power conversion. Power producing devices using this technology are called thermionic converters, and operate on very simple principles. Yet much is unknown as to the dynamics of their operation, and available computer simulation codes are unable to correctly model their performance. To help 'push back the frontiers of understanding' for this technology, I chose to design a computational model of the power producing region in a thermionic converter, using a technique which, to the best of my knowledge, has never been used before to model any device. My preparatory analysis produced a new collisionless sheath theory, extending previous theories to apply across the entire range of collisionless sheaths -- from those with very large potential barriers and small plasma temperatures to those with large plasma temperatures and small potential barriers. While developed

specifically for the analysis of sheaths in thermionic converters, there are many other applications possible -- such as low-voltage probe theory -- which have yet to be explored.

The hybrid PIC-Fluid technique worked well under conditions consistent with the assumptions used in its development, and represents a substantial advance toward the development of a physics-based, wall-to-wall model of an ignited mode thermionic converter. Future incorporation of the enhancements I identified in this effort will make my hybrid technique suitable for modeling thermionic converters.

A number of people and organizations contributed to my research effort. I would like to gratefully acknowledge the support of the Thermionic System Evaluation Test (TSET) project of the USAF Phillips Laboratory. They provided partial funding of this effort, and their comments and experience with thermionic systems were very helpful. I am deeply in debt to Dr. William Bailey, my faculty adviser, for his guidance and patience as we struggled with many of the issues and peculiarities associated with thermionic power conversion -- the hours we spent discussing (sometimes with great passion) the physics of the converter and the meaning of the equations with which we modeled it were the most profitable times of my doctoral experience.

I darkened a great many faculty doors as I struggled to develop our model and understand the thermionic converter. Many of those doors did not

belong to members of my committee, yet their owners lent me their ears and brains to help in my work. In particular, I thank Dr. Kirk Mathews, Dr. Dennis Quinn, and Dr. David Weeks for listening when I had to explain what I didn't understand, and for their ideas to help illuminate my darkness.

As it so often seems to be the case, my family has borne the brunt of my frustrations and disappointments, while usually not being able to understand or fully enjoy the successes of my time here. There are no words to express how much my wife, Kathy, and my children, Jason, Mark and Hannah, have meant to me. The future awaits us.

Finally, mentioned last not as an afterthought, but in the position of greatest honor, I thank Jesus for bringing me to this point in my life and for all that we have yet to accomplish. He is my very breath; if there is anything good or noble in me, it is because He has cultivated it. He gives my life meaning, and for that I will be grateful forever.

Table of Contents

	Page
Preface	iii
List of Figures	ix
List of Tables	xii
List of Symbols	xiii
Abstract	xv
I. Introduction and Background	1
Geometry and Physics of an Ignited Mode Thermionic Converter	5
Operating Conditions	19
Methods of Analysis for Thermionic Converters	21
Newtonian Kinematics -- Self Consistent Particle Simulations	21
The Convective Scheme	28
Kinetic Theory	31
The Fluid Equations	32
Phenomenological Models	37
Conclusion	38
II. A Closed Collisionless Sheath Theory for Low Voltage Sheaths	40
Introduction	40
Past Models	40
The Collisionless Sheath Model	43
Charged Particle Density In The Sheath	45
Emission Electrons (Cathode only)	45
Plasma Electrons	46
Plasma Ions	48
Total Charge Density	48
Calculation of the Electric Field in the Sheath	49
Boundary Conditions	50
Closing the System of Equations	51
Discussion	54
Comparison of Results for Space Charge Limited Conditions	54
Comparison of Cathode Sheaths in the Obstructed Mode	61

Page

Comparison to Particle In Cell (PIC) Calculation for Cathode Sheaths 62
PIC Comparisons for the Anode (Non Emitting Electrode) Sheath 66
Collisionality 67
Conclusion 69

III. A Hybrid PIC-Fluid Model 71

Introduction 71
The PIC Module 72
The Fluid Module 82
Interfacing the Sectors 93
The PIC-PIC Interface 96
The FLUID-FLUID Interface 99
The PIC-WALL Interface 102
The FLUID-WALL Interface 104
The PIC-FLUID Interface 104
Program Description 109
Simulation Level Description 110
Sector Level Description 112
The PF User Interface 114
Validation of the PIC-Fluid Hybrid Code 119
Conclusion 128

Chapter IV. Application to Modeling of Thermionic Converters 129

Introduction 130
The Observed Electron Velocity Distribution 131
Response of the Model to Departure from the Assumed Velocity Distribution 140
Alternative Interface Formulation 146
Recommendations to Make the Hybrid Model Robust 153
Conclusion 157

V. Conclusion and Recommendations 158

Recommendations for Future Work 160

Appendix A: Discontinuities in the Multi-Sector Approach 165

Appendix B: Correction to the Injection Velocity Adjustment Scheme Used in PDP1 178

Page

Appendix C: An Expression for the Height of the Space Charge Barrier in a Closely Spaced Thermionic Converter 182

Appendix D: Velocity Space Transform for Elastic Scattering 187

References 193

Vita 198

List of Figures

Figure	Page
1. Conceptual Description of a Thermionic Converter (a), and Potential Diagram for an Ideal Converter (b)	6
2. J-V Curves for Ideal Converter and Ignited Mode Converter.	8
3. Potential Diagram of an Effective Potential Barrier for an Ideal Converter	9
4. Potential Diagram for a Thermionic Converter with a Space Charge	10
5. Potential Diagram Sequence for the Ignition of a Cesium Converter	12
6. Potential Diagram of Cesium Converter at the Transition Point	15
7. Potential Diagram of the Obstructed Regime	16
8. Comparison Between TECMDL F Calculation and Experimental Data	17
9. Ignition Process in a Thermionic Converter Using Simplified Ionization Kinetics in a PIC Calculation	28
10. Potential Profiles Considered	43
11. Comparison of the Results of Previous Sheath Theories to the Present Theory	57
12. Comparison of Analytic Profiles to those from PIC Calculation	68
13. PDP1 Velocity Space Transformation	79
14. Relationship of Sectors and Interfaces in the Hybrid Model	94
15. Time-step Sequence for PIC-PIC Calculation	97
16. Time Sequencing in Fluid Calculation	101
17. Simulation Level Program Execution	111

Figure	Page
18. Calculation of the Electric Field Using Various Combinations of Techniques	124
19. Expansion of Time Averaged Electric Field Calculated using Various Techniques	125
20. Electron Density as Calculated by Various Combinations of Techniques	126
21. Ion Density as Calculated by Various Combinations of Techniques	127
22. Velocity Phase-Space Plot of a Maxwellian Velocity Distribution	132
23. Observed Phase Space Plot of Electron Velocity Distribution at Plasma-Sheath Boundary	132
24. A Drifting Half-Maxwellian Velocity Distribution	134
25. Velocity Distribution Resulting from the Isotropic Redistribution of the Energy in a Drifting Half-Maxwellian	136
26. Velocity Distribution When Half-Maxwellian Distribution Not Fully Redistributed by Collisions	137
27. Comparison of Distribution Function Based on Directed Flux Matching to Our Implementation	149
28. Spatial Discretization Using Major and Minor Grid Points	166
29. Discontinuity in Electron and Ion Densities at Interfaces	168
30. The Electric Field in the Presence of Discontinuities in the Charge Density	169
31. PIC Calculation of Electric Field	171
32. Range of Influence of Superparticle Motion on Calculated Value of Electric Field	172
33. Kink in Electric Field Arising From Discontinuity in the Charge Density at an Interface	176
34. PIC Leap-Frog Scheme	179

Figure	Page
35. Space Charge Potential Diagram for Stagnating Monoenergetic Electron Beam	182
36. Space Charge Potential Diagram with a Potential Minimum	185
37. Elastic Scatter Coordinate Frames	187
38. Particle Frame Superimposed on Laboratory Frame	188
39. Three Rotations of the Transformation Matrix	190

List of Tables

Table		Page
1.	Typical Thermionic Converter Characteristics	20
2.	Comparison to P&AC Analysis in the Obstructed Mode	62
3.	Calculated Sheath Characteristics for an Obstructed Mode Cathode	64
4.	Calculated Sheath Characteristics for an Saturated Mode Cathode	65
5.	Calculated Sheath Characteristics: Electron Retaining Anode Sheath	66
6.	Divergence in Directed Fluxes for a Beam-Plasma Velocity Distribution	146
7.	Non-Conservation at PIC-FLUID Interface -- 5% Beam	151

List of Symbols

α	the fraction of the plasma electron density at the sheath edge moving towards the sheath , also used for fraction of total density in the beam component of a beam+Maxwellian velocity distribution
μ	the incident flux of cesium atoms at the surface of a thermionic emitter (sec^{-1} cm^{-2})
υ	the collision frequency (Hz)
ρ	the net charge density (Coulombs $meter^{-3}$)
Φ	the sheath potential (volts)
ε_0	the permittivity of free space
Φ_E	emitter (cathode) work function (eV)
Φ_{eff}	the effective work function of the electrode (electron volts)
μ_e	the electron mobility (volt $meter^2$ $second^{-1}$)
μ_i	the ion mobility (volt $meter^2$ $second^{-1}$)
ΔV	the height of the potential barrier between the electrode potential and the potential $-V_E$ (volts)
A	Richardson's constant (1.204×10^6 amp $meter^{-2}$)
Da	the ambipolar diffusion coefficient (amp $meter^4$ $Coulomb^{-1}$)
d	the width of the inter-electrode gap (meters)
E	the electric field (volts $meter^{-1}$)
E_E	kT_E/e (volts)
E_e	kT_e/e (volts)
e	the elementary charge (1.602×10^{-19} Coulomb)
J_E	the electron emission current density from the cathode or the virtual cathode (amps $meter^{-2}$)
J_{e0}	the plasma electron current density in the limit as the electrode potential fall vanishes (amps $meter^{-2}$)
J_{ep}	the plasma electron current density that escapes to the electrode (amps $meter^{-2}$)
J_{ext}	the external circuit current divided by the electrode area (amp $meter^{-2}$)

J_i	ion current density (amp meter^{-2})
J_R	the electron emission current density predicted by the Richardson-Dushman Equation (amps meter^{-2})
k	Boltzmann's constant (1.38×10^{-23} Joules Kelvin^{-1})
M_{COLL}	the rate of change of energy due to collisions (eV/sec)
n_E	emission electron density (meter^{-3})
$n_e(V)$	the total electron density in the sheath due to plasma electrons ($n_e^+(V)$ + $n_e^-(V)$) (meter^{-3})
$n_e^+(V)$	the density of electrons moving away from the sheath at potential -V (meter^{-3})
$n_e^-(V)$	the density of electrons moving towards the sheath at potential -V (meter^{-3})
n_{e0}	the total electron density at the sheath edge due to plasma electrons (meter^{-3})
n_i	ion density (meter^{-3})
n_{i0}	ion density at the sheath edge (meter^{-3})
n_{max}	the maximum electron density in the plasma (meter^{-3})
q	species charge (Coulombs)
S_{COLL}	the net ionization rate (sec^{-1})
T	generic species temperature (eV)
T_E	the electrode temperature (Kelvin)
T_e	the plasma electron temperature (Kelvin)
$\bar{v}$	the average speed of a Maxwellian velocity distribution $\left(\sqrt{\frac{8kT_e}{\pi m_e}}\right)$ (meters sec^{-1})
V	the negative of the value of the potential (volts)
V_E	the magnitude of the potential at which the emission current density is specified (the cathode or virtual cathode)
V_0	the drop in potential corresponding to the average initial ion kinetic energy at the sheath edge (volts)
x_0	the location of the plasma/sheath boundary (sheath thickness in meters)

Abstract

A detailed collisionless sheath theory and a three-region collisional model of a bounded plasma are presented, and the suitability of the collisional model for analysis of ignited mode thermionic converters is analyzed. heath theory extends previous analyses to regimes in which the sheath potential and electron temperatures are comparable in magnitude. In all operating regimes typical of an ignited mode thermionic converter, the predicted sheaths extend several mean-free paths. The apparent collisionality of the sheaths prompted development of a collisional, three-region model of the converter plasma. By interfacing Particle-in-Cell regions (for the sheaths) and fluid regions (for the bulk of the plasma), a time-dependent, wall-to-wall model of the plasma in the inter-electrode space is created. The components of the model are tested and validated against analytic solutions and against one another, then applied to the analysis of an ignited mode thermionic converter. Under ignited mode operating conditions, the electron velocity distribution at the plasma/sheath boundary is found to be inconsistent with that assumed in the model development, and the calculation diverges. The observed distribution is analyzed and a new basis set of distribution functions is suggested that should permit application of the hybrid model to ignited mode thermionic converters.

A THREE REGION ANALYSIS OF A BOUNDED PLASMA USING PARTICLE IN CELL AND FLUID TECHNIQUES

I. Introduction and Background

Power systems employing thermionic power conversion transform heat into electrical energy using a device called a thermionic converter. Systems using this device operate efficiently at high temperatures and require relatively small radiators for thermal management. The compact, light-weight radiators make thermionic power systems attractive for space operations, as they give rise to substantial savings in launch costs over lower temperature, lower efficiency systems that require larger, more massive radiators. Mission integration studies performed by the space power group of the Phillips Laboratory indicate that thermionic systems could meet projected requirements for compact, lightweight power in a power range as low as 25-40 kilowatts(40:94). Prior to its dissolution, the Soviet Union developed several thermionic space nuclear power systems, and the United States has recently purchased electrically heated versions of the Soviet systems for test and evaluation, to learn from their experience. (38:1251-1256). As interest in thermionics has grown, a number of projects have been initiated in the United States to provide a foundation for the development of

thermionic converters. These projects include engineering development of thermionic converters (18:1225-1234,26:1219-1223), testing and modeling of thermionic switches (39), and design studies for thermionic space power systems in the 10-100 kilowatt power class (11:1235-1240, 31:951-956, 43:973-980). Yet in spite of the recent interest, many aspects of the converter characteristics are not fully understood. The complexity of the physical processes involved in the device make detailed analytic models impossible, and past numerical analyses have been frustrated, as none have been able to predict some of the important performance details -- particularly the current-voltage relationship of the converter in the obstructed regime of operation (to be described later in this chapter) (36:21).

At the crux of any model of a thermionic converter is a description (or calculation) of the conditions within the power production region of the device, that is, the inter-electrode space. In the past, numerical models have typically divided this space into three regions: two narrow regions just outside the electrodes (the "sheaths") and a much larger bulk plasma region in the middle of the inter-electrode space. Very different physical processes dominate in these regions and different approximations are used to describe them. Past models have typically used collisionless treatments for the sheath regions, and matched the conditions at the sheath boundaries to collisional treatments for the bulk of

the inter-electrode gap(36:23-26), but recent analysis by McVey et al. has called into question the use of a collisionless sheath model (36:33).

In this work, a detailed collisionless sheath theory and a three-region collisional model of a bounded plasma are developed, and the suitability of the collisional model for ignited mode thermionic converters is investigated. The sheath theory extends previous analyses to regimes in which the sheath potential and electron temperatures are comparable in magnitude -- as is the case for ignited mode thermionic converters. In all operating regimes typical of an ignited mode thermionic converter, the predicted sheaths extend several electron-atom and ion-atom mean-free paths into the inter-electrode space. The apparent collisionality of the sheaths prompted development of a collisional, three-region model of the converter plasma. By interfacing Particle-in-Cell (PIC) regions (for the sheaths) to fluid regions (for the bulk of the plasma), a time-dependent, wall-to-wall model of the plasma in the inter-electrode space is created that places no restrictions on the structure, magnitude or extent of the sheaths.

In the remainder of this chapter, a brief description of the geometry, physics and operating conditions typical of planar, cesium vapor thermionic converters is presented. Previous modeling approaches are then reviewed, along with their shortcomings. In Chapter II, the collisionless sheath theory is presented and validated by comparison to collisionless PIC calculations. The

theory is then used calculate the thickness of the sheaths for comparison to the scattering mean-free-paths.

The wall-to-wall collisional model is formulated in Chapter III. No new analytic techniques are developed, rather, existing techniques which have proven their usefulness and reliability are interfaced together in a new and unique way. The PIC technique used for modeling the sheaths is briefly reviewed, followed by a presentation of the fluid equations used for modeling the plasma in the bulk of the inter-electrode space. Finally, the interfaces necessary to enable a hybrid approach are discussed, and an overview of the computer program and user interface is given. The model is validated by comparison to both analytic solutions and to calculations based on very different computational techniques.

In Chapter IV, the results of an application of the model under conditions similar to those found in an ignited mode thermionic converter are presented. Under those conditions, it is shown that the electron velocity distribution in the plasma at the sheath edge differs significantly from that for which the model was formulated, and the calculation diverges. The divergence of the calculation is analyzed, and suggestions are made for changes to the model which will enable its application to ignited mode thermionic converters.

Finally, in Chapter V, conclusions and recommendations for future work are presented.

Geometry and Physics of an Ignited Mode Thermionic Converter.

Before describing the geometry and physics of the thermionic converter, it may be helpful to distinguish between this device and a similar device, the thermionic diode. The thermionic converter is a power-producing device. It converts heat into electricity using electrons emitted from a heated metal surface and collected on a cooler metal surface. A thermionic diode, on the other hand, is a powered device. The voltage across a diode is an applied voltage that draws the emission electrons from the cathode to the anode. While a diode may operate with a voltage across the electrodes of 100 volts, the voltage in a thermionic converter is typically on the order of 0.5 volts.

In a converter, the voltage available to drive a load is self-generated, and arises from two sources. First, the work function of the anode is frequently smaller than that of the cathode, as in Figure 1(b). In this case, all of the electrons emitted from the cathode have the potential to do work equal to the difference between the cathode and anode work functions. Second, the electrons from the cathode carry significant amounts of kinetic energy. Therefore, even when the combination of the anode work function and the load voltage in the external circuit is greater than the cathode work function, current can still flow between the cathode and the anode; the emitted electrons simply lose kinetic energy as they move towards the anode and gain potential energy. One final note; in the literature the distinction between the terms "thermionic converter"

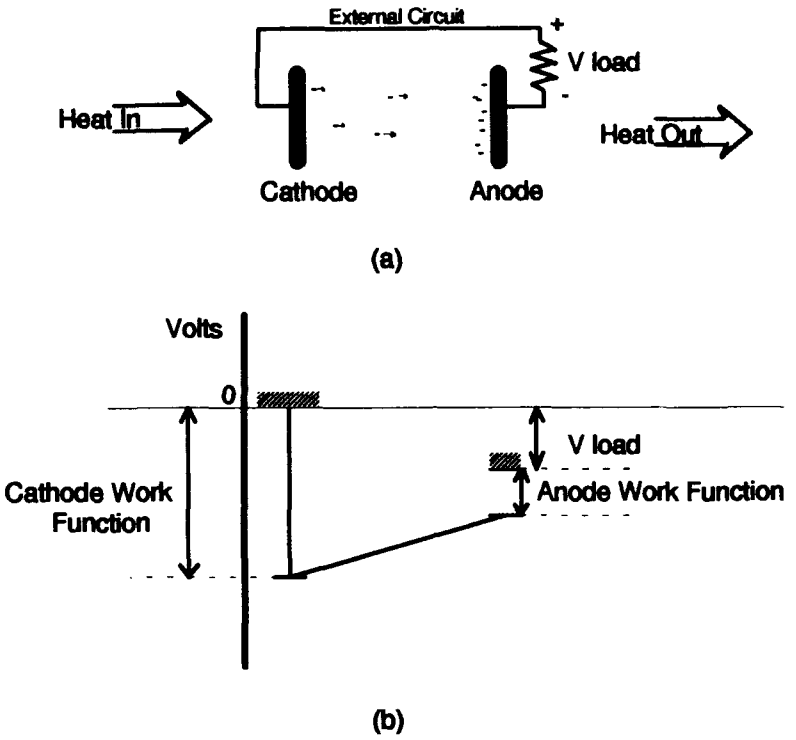

Figure 1. Conceptual Description of a Thermionic Converter (a), and Potential Diagram for an Ideal Converter (b).

and "thermionic diode" is often not made, and the term "diode" is often used when "converter" is meant. This work is only concerned with thermionic converters, and the discussion is limited to power producing devices.

The most intuitive way to discuss the geometry and physics of thermionic converters is to begin with a description of a simplified, or "ideal" converter, and then to describe how an actual converter differs from this ideal case. To help in the discussion, frequent references will be made to the drawings and diagrams presented in Figure 1 (a) and (b), and Figure 2. Figure 1 illustrates the geometry and potential profiles of an ideal converter, and the relationship

between the electrode work functions, the voltage across the inter-electrode space, and the voltage across the load in the external circuit. Figure 2 illustrates the relationship between the current in the external circuit and the load voltage. This relationship is often called the current - voltage characteristic, and when plotted is referred to as a "J-V curve" in the literature.

The operation of an ideal thermionic converter is conceptually simple. As illustrated in Figure 1 (a) and (b), a metallic surface, the cathode, is heated to a high temperature. A second cooler surface, the anode, is mounted close to the first. When heated, some of the electrons in the cathode gain enough energy to overcome the cathode work function and enter the inter-electrode space with the potential energy equivalent of the cathode work function. The electrons pass across the inter-electrode space, exchanging potential energy for kinetic energy, until they arrive just outside the anode surface. At the anode, their excess kinetic and thermal energy, as well as the energy resulting from traversing the anode work function, is rejected as waste heat. The external circuit extracts work from the electrons through the potential drop across the load ("V load" in Figure 1) and returns the electrons to the cathode.

In an ideal converter, the cathode surface emits a thermionic electron current density according to Richardson's equation: (46:172)

$$J_s = AT_s^2 \exp(\frac{-\Phi_{eff}}{kT_s}) \qquad (1)$$

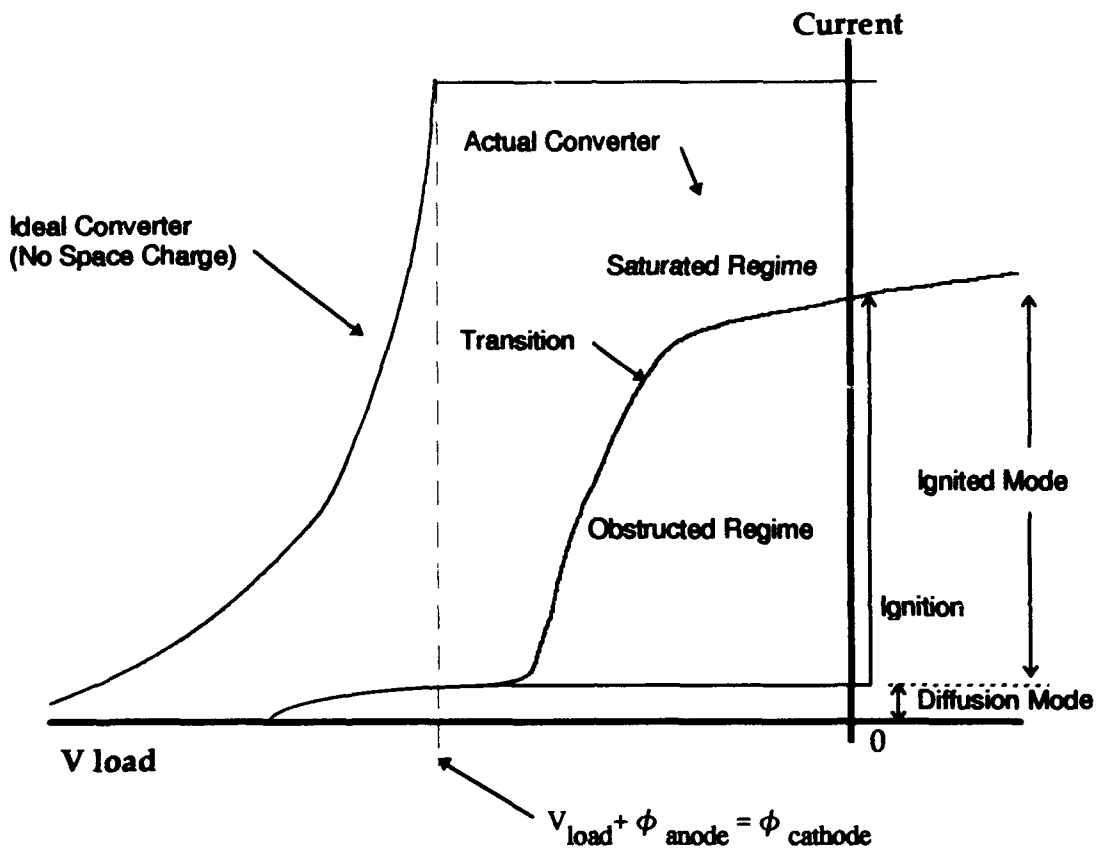

Figure 2. J-V Curves for Ideal Converter and Ignited Mode Converter. (46:1194)

where J_s is the surface emission current density, A is Richardson's constant, T_s is the temperature of the surface, k is Boltzmann's constant, and Φ_{eff} is the effective potential barrier the emitted electrons have to overcome (in an actual converter, the anode emits electrons as well, but the emission current density is usually negligible because the anode is much cooler than the cathode). If the sum of the load voltage and the collector (anode) work function is less than the emitter (cathode) work function, as in the device illustrated in Figure 1 (b), the effective potential barrier for the emission electrons is simply the emitter work function,

and a constant current flows in the circuit, independent of load voltage. This relationship accounts for the flat portion of the ideal converter J-V curve to the right of the vertical dashed line in Figure 2.

If the load voltage is increased so that the sum of the load voltage and the collector work function is greater than the emitter work function (as illustrated in Figure 3), an effective potential barrier exists between the cathode and the anode that is greater than the emitter work function. The emission electrons have to overcome this potential barrier to get from the cathode to the anode. As the load voltage is increased, the effective barrier increases and the current in the external circuit drops exponentially, eventually vanishing as the open circuit voltage is reached. This relationship accounts for the exponentially decaying portion of the ideal converter J-V curve to the left of the vertical dashed line in Figure 2.

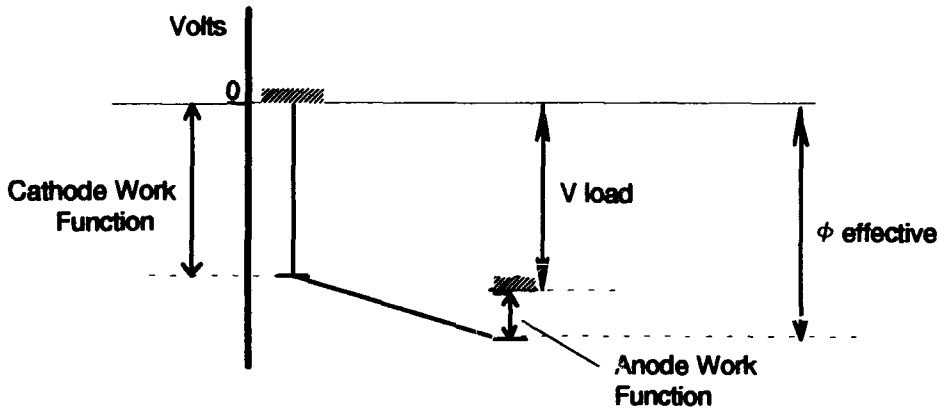

Figure 3. Potential Diagram of an Effective Potential Barrier for an Ideal Converter.

While the above description applies to an ideal converter, the real world is seldom so simple. As the electrons move into the gap between the electrodes, a negative charge density develops as illustrated in Figure 4. This charge density (called a space charge) repels the electrons emitted from the cathode, and the actual net current density delivered to an external circuit is substantially less than the emission current density.

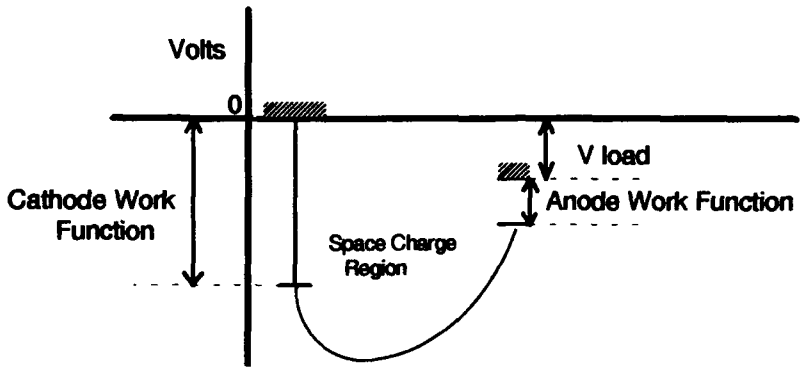

Figure 4. Potential Diagram for a Thermionic Converter with a Space Charge.

For a parallel plate diode, Langmuir (27:456) showed that the space charge limits the current density to a maximum given by:

$$J = \frac{\sqrt{2}}{9\pi}\sqrt{\frac{e}{m_e}}\frac{V^{\frac{3}{2}}}{x^2} = 2.33\times10^{-6}\frac{V^{\frac{3}{2}}}{x^2}\ amp/cm^2 \qquad (2)$$

where V is the magnitude of the accelerating potential (in volts) across the electrode gap, and x is the distance (in cm) between the electrodes. Langmuir's result is for a powered diode. A similar derivation for an un-powered diode is

presented in Appendix C and results in the same expression for the space charge limited current density with V replaced by the difference between the cathode and anode work functions. For a typical vacuum thermionic converter, the bare work function difference is only on the order of a few volts. With a typical gap dimension of 0.05 cm, this leads to a maximum current density on the order of a milliamp/cm^2, compared to a typical emission current density of tens of amp/cm^2.

To reduce the space charge limitations, a vapor is introduced into the gap, typically an alkali metal such as cesium. Upon contact with the hot, high work function emitter surface, the cesium atoms are ionized, producing a positive ion current density given by the Saha-Langmuir formulation (47:1196):

$$J_{is} = e\mu\left[1+2\exp\left(\frac{V_i-\Phi_E}{kT_E}\right)\right]^{-1} \qquad (3)$$

where μ is the incident flux of cesium atoms at the surface of the emitter ($\mu \cong 1.3 \times 10^{20}\, p$ cm^{-2} s^{-1}, for a cesium pressure of p torr), e is the charge on the cesium ion, V_i is the ionization energy of the cesium atom (3.9 eV), T_E and Φ_E are the emitter temperature and work function, respectively, and k is Boltzmann's constant.

The positive ions move into the gap under the influence of the space charge potential gradient. The positive ion density eventually begins to significantly compensate the negative space charge. This mode of operation,

with surface ionization of the cesium as the dominant source of ions, is represented in Figure 2 by the portion of the J-V curve labeled *diffusion mode.*

Under certain circumstances, stepwise volume ionization of the cesium atoms can become the dominant source of ions(3:5-7) and the converter enters what is known as the *ignited mode* of operation. A thorough description of the process of ignition is presented by Baksht (3:327-330) and summarized below. For emitter temperatures below about 1600 K, the current-voltage characteristic of a converter is discontinuous. As the load voltage is lowered an abrupt transition (called "ignition") takes place between the diffusion mode of operation and the ignited mode. The point on the J-V curve at which this process occurs is labeled 'Ignition' in Figure 2. The temporal evolution of the inter-electrode potential during ignition is illustrated in Figure 5.

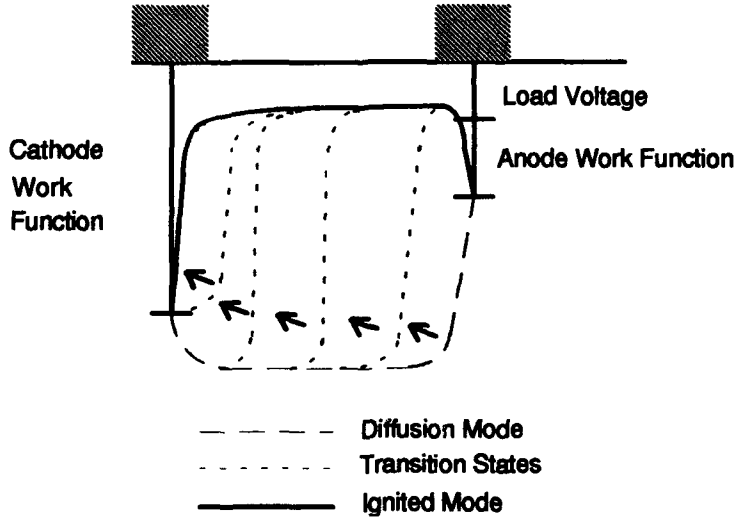

Figure 5. Potential Diagram Sequence for the Ignition of a Cesium Converter.

As the ignition voltage is approached, a large potential drop develops adjacent to the anode. The magnitude of the potential drop increases as the load voltage is decreased; if the load voltage is made sufficiently small, electrons traveling to the anode pick up enough energy to ionize the cesium vapor. When the rate of ion production in the vicinity of the anode exceeds the rate at which the ions move towards the cathode, the positive ion density in the vicinity of the anode sheath increases. The electrons produced by the ionization are swept to the anode, leaving a relatively *positive* space charge between the anode and the bulk of the plasma. This increases the potential through which the electrons fall, increasing electron kinetic energy and the ionization rate of the cesium vapor. Once initiated, the ignition process is self-sustaining, and the location of the large potential gradient sweeps across the inter-electrode gap. Steady state operation is achieved once the rate at which ions are lost to the electrodes just balances the net generation rate of ions in the bulk of the plasma. This mode of operation of the converter is known as the *ignited mode,* and is the focus of this research effort.

At higher emitter temperatures (1600-2000 K), the above description is only slightly modified(3:326); the potential gradient outside the anode extends farther into the inter-electrode space, and electrons begin to pick up energy well before they enter the pre-anode region. Also, the discontinuity between the current - voltage characteristic of the diffusion regime and the ignited regime

becomes less pronounced. Still, the build-up of positive space charge begins adjacent to the anode and the change in the form of the potential occurs basically as described above.

The ignited mode displays two distinct regimes of operation, divided by the point labeled 'Transition' in Figure 2. At current densities greater than at the transition point, the device operates in what is known as the 'saturated regime'. In this regime the emission current density is 'saturated' in the sense that essentially all the thermionic electrons emitted from the cathode surface enter the plasma due to the accelerating electric field at the cathode surface (the current in the external circuit is still somewhat less than for an ideal converter, however, because of losses due to the finite resistance of the plasma). The accelerating field at the cathode surface lowers the effective work function and produces an additional electron current density through what is known as the Schottky effect (3:25), giving rise to a small increase in current density for voltages positive with respect to the point marked 'Transition' on the J-V curve presented in Figure 2. The normal operating point for an ignited mode thermionic converter is just above the "knee", just to the right of the point of transition (47:1196-1201), as this results in maximum efficiency. At the point of transition the electric field at the emitter vanishes. A potential diagram for operation at the transition point is given in Figure 6.

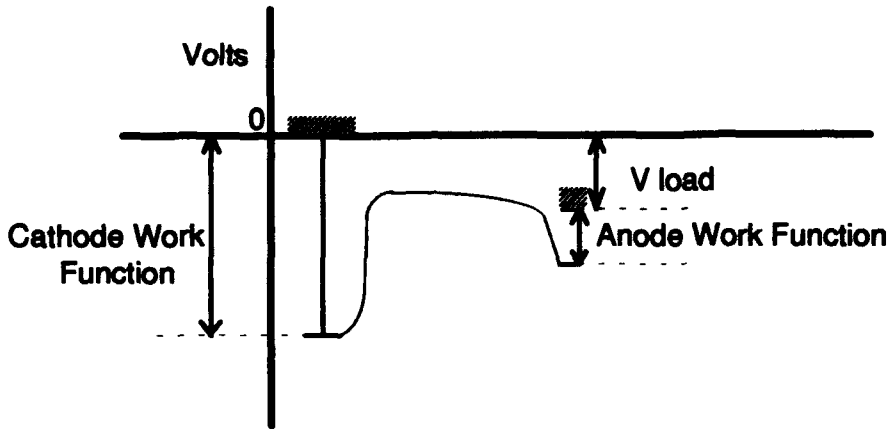

Figure 6. Potential Diagram of Cesium Converter at the Transition Point.

At larger load voltages, (the obstructed regime) volume ionization is not sufficient to fully neutralize the space charge, and current in the external circuit drops dramatically. Some uncertainty exists as to the structure and development of the potential profile in this regime. According to Baksht (3:298, 333-335), a retarding field develops just outside the cathode, as illustrated in Figure 7, giving rise to what is known as a double sheath. The location in the sheath where the field first vanishes is then known as the virtual cathode. The double sheath serves to preserve the temperature of the electrons in the plasma by reducing the loss of hot electrons to the cathode and by preventing the electrons at the low end of the emitter electron velocity distribution from entering the plasma. Thus it serves as a sort of thermal insulator.

By keeping the electron temperature high, the ionization rate can be maintained -- but only over a very narrow load voltage range. The plasma is heated mainly by the energy of the injected electrons; as the double sheath

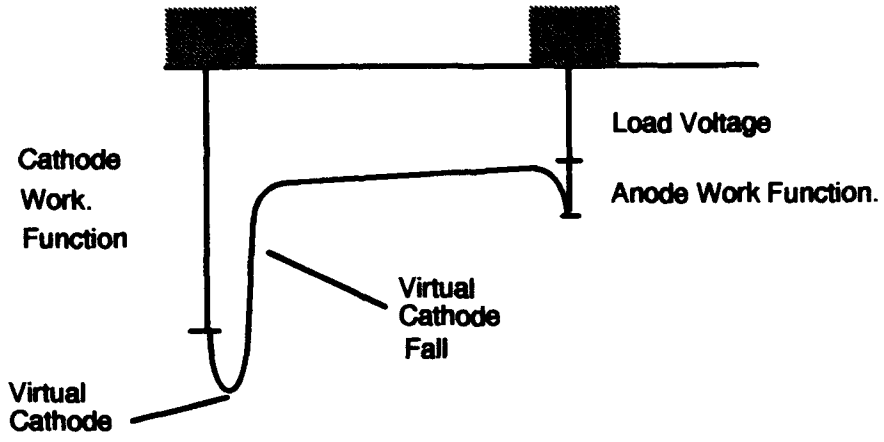

Figure 7. Potential Diagram of the Obstructed Regime.

grows it reduces the electron injection current density into the plasma. Thus, the plasma heating rate declines as the load voltage continues to increase. At sufficiently large load voltages, the reduction in the plasma heating rate overwhelms the insulating effect of the double sheath. Once volume ionization is insufficient to maintain the relatively positive (with respect to the cathode) potential in the inter-electrode space, the operation of the converter reverts to the diffusion mode.

Baksht's model of the obstructed regime, summarized above, closely parallels that given by Rasor, and implemented in a widely used phenomenological computational model of planar thermionic converters called TECMDL (36:79, 46:176-180). The trouble with Baksht's and Rasor's models is they result in an exponential relationship between the load voltage and the current in the external circuit. Figure 8 presents a comparison of an

experimental J-V curve to one predicted using TECMDL; TECMDL does a good job of predicting the performance of ignited mode converters at the point of maximum power production (just above the "knee" or bend in the J-V curve), but the slope of the experimental J-V curve is much greater in the obstructed regime than predicted by TECMDL. The literature speaks of this disagreement between theory and the experimental data as the "faster-than-Boltzmann" or "faster-than-exponential" rise.

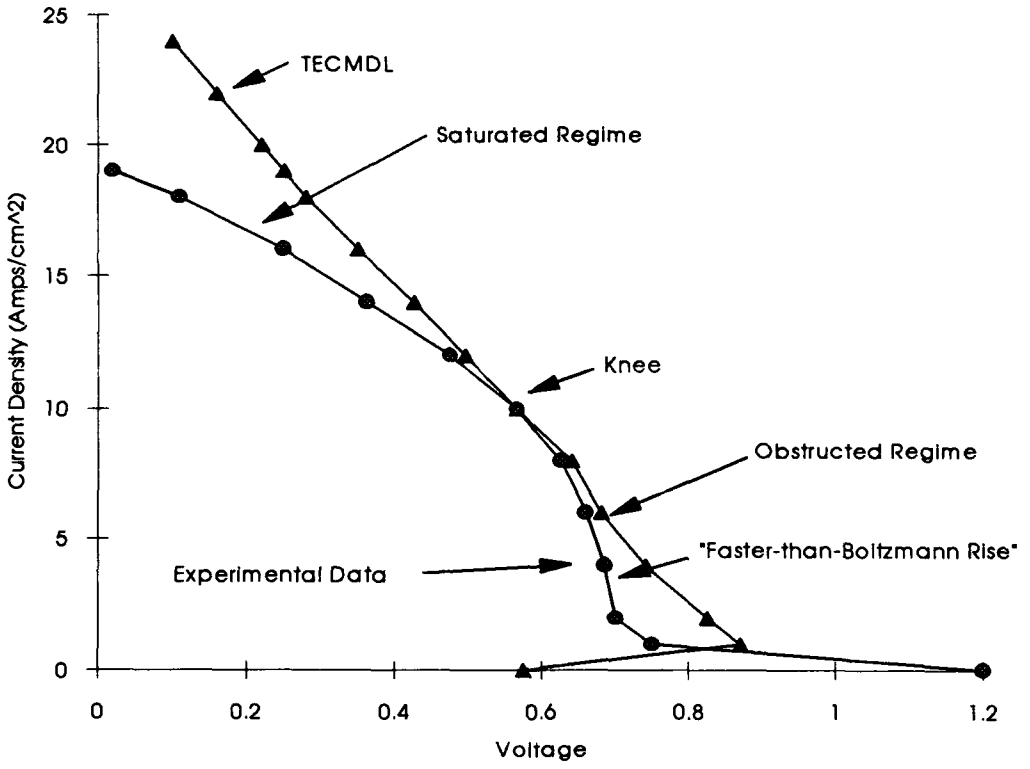

Figure 8. Comparison Between TECMDL F Calculation and Experimental Data (36:23).

Because of the disagreement between theory and experiment, other models describing the evolution of the potential profile in the obstructed regime have been sought. In the saturated regime of operation, the discharge generally covers the entire electrode surface, both at the anode and at the cathode (3:327). Britt (6) has suggested that the areal cross section of the ignited region between the electrodes begins to contract at the point of transition, so that the discharge no longer covers the emitter and collector surfaces. Eventually, he suggested, the discharge region for planar converters reduces to a sphere just barely contacting the emitter and collector surfaces. Once contact is lost with one of the surfaces, the sphere becomes unstable and the discharge is extinguished. He based this suggestion on filtered optical observations he had made of the discharge in a planar thermionic converter.

Baksht (3:327-331) mentions this phenomena, but says the contraction of the discharge only occurs for emitters with low temperatures (T_E<1600-1700 K) and that the onset of contraction begins after the formation of the virtual cathode. The observed discrepancy between TECMDL and experimental data shown in Figure 8 is for a thermionic converter operating with an emitter temperature of 1800 K. At emitter temperatures above 1700 K, Baksht says the discharge does not contract, but is stable throughout the entire obstructed regime(3:335). Thus, based on Baksht's analysis, one wouldn't expect constriction to be the cause of the observed discrepancy.

Another explanation for the rapid drop-off in current in the obstructed regime was made by Main, who suggested that ion trapping in the double sheath -- caused by charge exchange collisions and neglected in the collisionless sheath models -- might cause the faster-than-exponential decrease in the current in the obstructed regime(33:317). According to Main, the trapping of ions increases the plasma density close to the emitter, resulting in a loss of ionization energy to the emitter. This loss reduces the ionization rate and increases the voltage drop across the plasma, steepening the current-voltage characteristic in the obstructed regime(33:317). Main did not quantify the amount of trapping which might occur in an actual thermionic diode, but instead performed a parametric study in which he arbitrarily defined a trapping parameter which he then varied to determine the effects of various amounts of trapped ions. McVey et al., however, performed analyses in which they numerically calculated the equilibrium trapping and escape rates and found that the inclusion of ion trapping in their model actually decreased the slope of the J-V curve in the obstructed regime, rather than increase it (36:33).

Operating Conditions.

Having reviewed the basic principles of operation for thermionic converters, it is helpful to note the typical conditions under which thermionic converters operate. Plasma conditions vary widely across the many different

configurations possible for thermionic converters and diodes. The current design emphasis in the United States is on ignited-mode converters with cesium pressures of about 1 torr. Typical operating conditions for converters in this class are given in Table 1, based on general information found in the literature.

Table 1. Typical Thermionic Converter Characteristics

Cesium Pressure (torr):	1-2
Plasma Frequency (Hz):	10^{10} - 10^{11}
Electron Density (m-3):	10^{18} - $5x10^{19}$
Converter Gap (mm):	0.5
Debye Length (mm):	$4x10^{-3}$ - $5x10^{-4}$
Particles in a Debye Sphere:	~225 - 31
Elec-Atom Collision rate (Hz):	10^{6}-10^{7}
Elec-Elec Collision rate (Hz):	10^{8} - 10^{9}
Sheath Character:	Collisionless?
Bulk Character:	Collisional
Cathode Temp (K):	1700-1900
Anode Temp (K):	800-900

Cathode temperatures are typically 1700 - 1900 K with anode temperatures of 800-900 K. Current densities range from 3 to 15 amps/cm^2 at a converter output voltage of about 0.5 volt. In the ignited mode, the dominant process for ionizing the cesium atoms is multi-step ionization, with an excitation threshold for the first excited state of 1.4 eV (42:667). As the typical plasma electron temperature is about 0.3 eV, only the electrons in the high-energy tail of the electron velocity distribution participate in the ionization process. The

dominant collisional processes in the plasma are elastic scattering off of the atoms (for the electrons), Coulomb collisions (for both electrons and ions), and charge-exchange with the neutrals (for the ions) (3:55-66). Under certain conditions, three-body recombination of the ions and electrons can become a significant ion loss mechanism (42:656). Coulomb collisions between the emission electrons and the plasma electrons provides the principal heating mechanism for the plasma (3:167,193-196).

Methods of Analysis for Thermionic Converters.

A number of analytical approaches have been taken to model thermionic converters. Broadly, they can be described as belonging to one of four classes: Newtonian Kinematics, Kinetic Theory, Fluid Equations, and Phenomenological Methods. Each of these approaches will be described in the pages that follow, along with their principal advantages and disadvantages.

Newtonian Kinematics -- Self Consistent Particle Simulations (5:65-85). Perhaps the most basic and conceptually simple theory available for the description of plasmas falls back to Newton's second law: Force = mass x acceleration, coupled with Maxwell's equations and a circuit model. Each particle in the system is represented in a six dimensional phase space (three spatial and three velocity dimensions); currents and fields are calculated using Maxwell's equations and a circuit equation, and the resulting forces are applied

to the particles to move them through phase space. The most obvious drawback to such a scheme is that the number of particles which must be followed can be quite large, and the maximum time-step for particle movement can be quite small. For high pressure thermionic plasmas of interest, one may be considering 10^{13}-10^{14} electrons and ions in the system, not to mention neutrals and excited species, with limiting time-steps of on the order of picoseconds. The memory requirements make it impossible to track that many particles with today's level of computer technology, and the run-times for problems of interest make such schemes extremely unattractive.

To make particle simulations more tractable, a number of simplifications have to be made. For example, the number of particles is reduced by tracking a single 'superparticle' which may represent 10^8 actual particles, rather than tracking the individual particles themselves. In many cases, neutral species density can be treated as a spatially varying but temporally constant and not tracked explicitly. Charge densities and resultant electric fields can be calculated at points on a spatial grid rather than at the exact location of the superparticles. In many cases symmetry can be used to reduce the problem being modeled to an equivalent one or two dimensional problem.

Methods using these simplifications are variously referred to as Particle In Cell (PIC) or Cloud In Cell (CIC) codes, or simply particle simulations, and are finding wide application in the plasma processing industry(51:725-732). A nice

summary of the rather extensive application of PIC techniques to simple bounded plasma systems has recently been given by Kuhn (24:512-513,526-533). There are no theoretical limitations to the application of particle simulations, rather, the limitations tend to be computational. To resolve the electric fields within the plasma, the spatial grid spacing must be less than a Debye length. In regions where the Debye length has no precise definition, such as the highly non-Maxwellian sheath regions in a thermionic converter where the electrons exhibit beam-like behavior, the grid spacing must be small enough so that the electric field can be properly resolved. To correctly model the transport of particles through the plasma, the time-step must be small enough that very few particles cross more than one spatial cell boundary during a time-step. Combined with the constraint that the cell size must be less than a Debye length, this constraint on the time-step leads to a maximum theoretical time-step of the order of the inverse of the plasma frequency, although the actual time-step may be much shorter in small devices.

In addition to the small time-step, there are a number of considerations that make a wall-to-wall model of a thermionic converter using PIC techniques unattractive. Collisions are handled in the PIC and CIC approaches using Monte Carlo techniques, and are usually limited to interactions between charged and neutral particles. Charged particle interactions are assumed to be implicitly accounted for by the interactions of the particles with the calculated fields. This

presents a problem in one dimension, as it underpredicts energy transfer by Coulomb collisions between the electrons (10:422). In a one dimensional PIC simulation, beam electrons interact with plasma electrons only through the electric fields. Because the electric field in one dimension can only accelerate or retard the motion of an electron along the principal dimension, the series of small angle deflections that characterize the interaction between beam and plasma electrons in three dimensions does not occur. Thus, electron-electron collisions cannot result in a transfer of kinetic energy from the component of the beam electrons' velocity along the principal axis to the transverse component, nor to the transverse velocity components of the plasma electrons' velocity vectors. Without this energy transfer mechanism, the relaxation time to a Maxwellian velocity distribution is unrealistically long.

In a thermionic converter, the cathode emission electrons typically gain an energy of 0.5 to 1.0 eV when traversing the cathode sheath. This energy is deposited in the plasma as the injection electrons cool to the plasma electron temperature (typically 0.3 eV) and is the principal energy source for ionization (3:167). In the ignited mode, thermalization of the emission electrons occurs primarily as a result of electron-electron collisions (41:280, 3:193-196, 42:657, 49:298), although other processes, such as collisionless damping, inelastic scattering off of excited atoms and, for the high energy electrons, excitation of ground state atoms to the first excited state may play a role. Because the one

dimensional PIC technique handles energy relaxation through electron-electron interactions poorly, the thermalization of the emission electrons and heating of the plasma would be underpredicted if the technique were used in the bulk plasma regions.

Another concern regarding the use of a PIC approach for modeling the bulk region of the plasma in a thermionic converter has to do with the ionization kinetics of cesium. The ionization of cesium is a multi-step process, with an excitation threshold for the first step of 1.4 eV (42:656-667). Because the plasma electron temperature is typically 0.26 eV, only 1 percent of the electrons in the simulation (those in the high energy tail of the velocity distribution) have enough energy to participate directly in the ionization process. Thus, for every electron which could lead to an ionization in a given time-step, 100 non-ionizing electrons must be tracked in the simulation. Scoping calculations performed using a PIC simulation and single-step ionization indicate that greater than 100,000 superparticles must be tracked to achieve statistically significant ionization rates. Tracking this many particles in a simulation results in extremely long run-times (several seconds per picosecond time-step). Furthermore, because the ionization process in cesium is multi-step, excited state species must be tracked as well. Tracking the excited state species would involve modeling excitation and de-excitation of the excited state species, and the collisions between the excited state species and the other particles in the

simulation (electrons, ions, neutrals and other excited state species). The associated computational overhead using particle techniques quickly becomes excessive.

Finally, there is a difficulty associated with the recombination process. Three-body recombination of electrons and ions in a thermionic converter plasma can be the dominant loss mechanism for ions (42:656). Representing three-body recombination properly in a PIC calculation would require the introduction of particle-particle-particle interactions and add significant complexity to the calculation. The statistics associated with the event would require large numbers of particles to be tracked, again increasing the already long run-time of a calculation.

While there are many difficulties associated with the PIC approach, it has its strengths as well, the biggest of which is that the technique is not tied to any assumed form for the particle velocity distributions, or to any assumptions regarding the potential profile or boundary conditions. It is easily implemented in regions where multi-step ionization and recombination may not be significant, and where the principle collision events for electrons are elastic and inelastic scatter off of the neutrals. As mentioned previously, PIC techniques have been used extensively in the modeling of RF discharges and simple bounded plasma systems. The PIC approach has been used to model thermionic diodes using simplified device physics (ignoring ionization and recombination, for example,

or using a fill gas with single step ionization), especially low pressure devices, and the results are qualitatively, and in some cases quantitatively interesting. An example is the work of Burger (8:658-666), who used PIC techniques to examine the effects of elastic collisions on the unstable behavior of nearly collisionless, low-pressure thermionic diodes, and showed that the inclusion of collisions eliminated the instability associated with multiple solutions to the potential profile for a given injection current density. Later in this dissertation, PIC simulations of an ideal diode will be reported that reproduced analytic values for the voltage across the inter-electrode space to within 0.01%. In scoping studies early in this effort, a PIC simulation of the ignition process was performed using single step ionization and an emitter temperature of 1800 K. The ignition process and development of the potential profile followed closely that discussed earlier in this chapter, as illustrated in Figure 9 (In the figure, traces 1-5 represent the development of the potential profile in response to an abrupt change in current; traces 6-8 are steady state profiles labeled in order of increasing current).

PIC techniques were also used in this effort to model collisionless sheaths and were able to reproduce analytic results quite accurately, as will be discussed in the evaluation of the collisionless sheath theory. These experiences with PIC techniques led to the conclusion that a PIC method could work quite well for

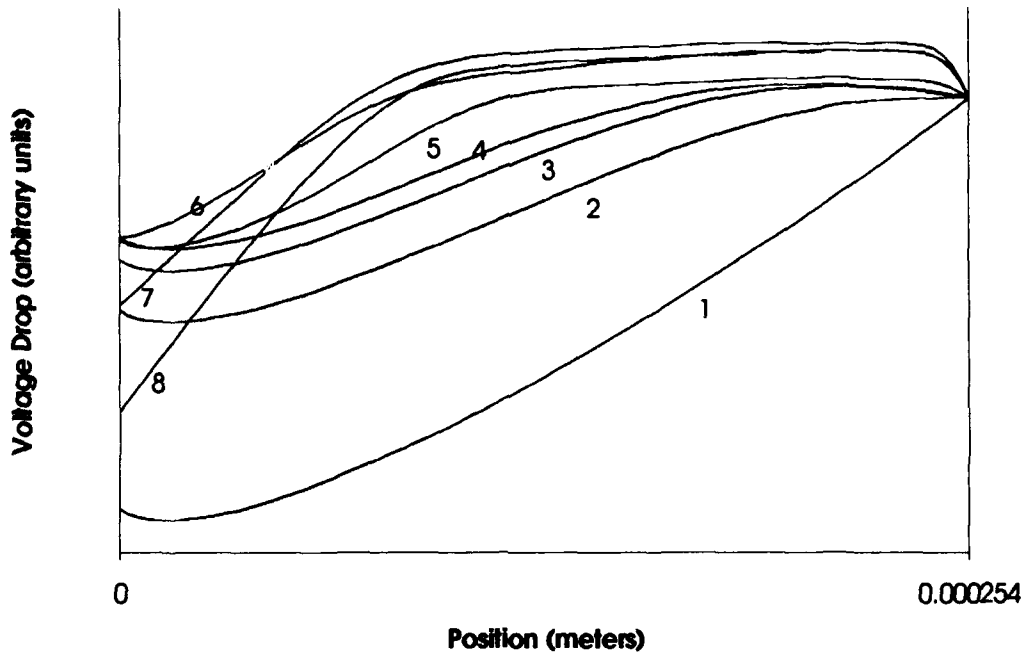

Figure 9. Ignition Process in a Thermionic Converter Using Simplified Ionization Kinetics in a PIC Calculation.

modeling the sheath regions, if successfully mated to a more suitable technique for the bulk of the plasma.

The Convective Scheme. Closely related to the particle simulation methods is the Convective Scheme(CS), recently developed by Hitchon et al. at the University of Wisconsin (16:79-95). In this method, according to Hitchon, the movement of charged species is tracked in terms of phase space (velocity and position) density, rather than in terms of discrete particles. Simply put, the acceleration of particles in a particular phase space cell is calculated based on the fields acting at the position of each face of the cell. The trajectory of each cell

through phase space is calculated for a single time-step, and the uncollided portion of its contents distributed into the cells it overlaps at the end of the time-step. The fraction of the cell contents that would have undergone collisions at each cell crossing is also calculated using Monte Carlo techniques, and the results of the collisions distributed accordingly. Coulomb collisions are handled by fitting the actual calculated velocity distribution to a finite sum of Maxwellian distributions using a least squares fit. The rate of energy transfer between the distributions is then directly calculated based on conservation of total energy, and new temperatures for each distribution are calculated. The change in density in each phase space cell in the original distribution is then calculated and the density adjusted accordingly. Maxwell's equations are then used in conjunction with the circuit equations to compute the new value of the fields based on the new charge density distribution(36:36-43).

The CS tracks particle densities rather than indivisible 'superparticles'. This allows for the modeling of large variations in particle densities without having to track large numbers of particles, and results in a smoother movement of density from cell to cell, hence less statistical noise. The tracking of particle density in phase space does carry the extra overhead of discretizing velocity space, not required in the particle simulations, but for many applications the extra overhead may be more than compensated by the reduction in the number of movements (either 'superparticle' or particle density) being tracked.

As the name implies, the CS is best suited for situations in which convection (collisionless transport) dominates over diffusion (16:83), that is, when the mean free path of the particles being tracked is much greater than the dimensions of the spatial cells. Because the density within each cell is moved through phase space as a collective unit, the size of a spatial cell must be such that only a small fraction of its contents undergo a collision when moving across its dimension. As with the particle simulation schemes, the cell size must also be smaller than a Debye length to accurately calculate the fields in the plasma. In addition, the time-step appropriate for the scheme must be less than the minimum collision time for the particles being modeled, and less than the inverse of the plasma frequency to adequately model particle transport through the plasma. These considerations restrict efficient applications to relatively low density systems, because at high densities the number of cells required becomes excessive. These restrictions are no greater, however, than those involving the PIC technique, and many of the conditions under which PIC techniques are applied appear suitable for CS treatment.

Wright Laboratories recently issued a report on an effort to develop a more accurate one dimensional "wall-to-wall" model of a thermionic converter using the convective scheme (45:89). The thrust of the effort was initially to develop the model, use it to determine the phenomena governing the shape of the J-V curve and the details of the sheath structures, and then develop a new,

fast phenomenological model based on the detailed model as a successor to TECMDL, a widely used phenomenological model of thermionic converters. If they achieved this goal, they planned to extend the model to 2D in cylindrical coordinates, what the project termed a "semi 3D" model. Unfortunately, the funding for the project was terminated before the model could be completed (36:45).

Kinetic Theory. The distribution of particles in phase space can be described by the solution of a conservation equation known as the Boltzmann equation:

$$\left.\frac{\partial f}{\partial t}\right|_c = \frac{\partial f}{\partial t} + \mathbf{v} \bullet \frac{\partial f}{\partial \mathbf{X}} + \frac{q}{m}\left\langle \mathbf{E} + \frac{\mathbf{v} \times \mathbf{B}}{c} \right\rangle \bullet \frac{\partial f}{\partial \mathbf{V}}. \qquad (4)$$

where the left hand side represents the time rate of change of the velocity distribution function in phase space due to collisions, f is the particle distribution function in phase space, **E** is the electric field vector, **B** the magnetic field vector, and **v** is the particle velocity vector. The equations for the different species of particles present in the plasma are coupled through the collisional term, and the resulting set of equations can be nonlinear and difficult to solve. If an appropriate form of the collisional term is known, this equation can be solved numerically for the distribution function using standard finite difference techniques.

The numerical solution is generally computationally expensive due to time-step limitations imposed by the Courant-Freidrichs-Levy(CFL) criterion.

As an example, the maximum time-step allowable in the CS and particle approaches is the inverse of the plasma frequency, 10^{-10} to 10^{-11} seconds for the high pressure converter. The CFL criterion would limit the time-step to the time it takes the fastest particle in the system to cross a single spatial cell (16:79). The time it takes for a 3000 K electron to traverse a Debye length in a high pressure converter is about 10^{-12} seconds, more than an order of magnitude smaller than for plasma frequency limited PIC or CS methods. In addition, velocity distributions in the sheaths can be nearly discontinuous at some points leading to numerical diffusion (36:35-36), so finite differencing of the Boltzmann equation is usually avoided. Some work was recently performed, however, in an attempt to develop a model based on the finite differencing of the Bernstein-Greene-Kruskal (BGK) version of the Boltzmann transport equation, but the problems mentioned above were encountered (45:86-87).

The Fluid Equations. In many cases the motions of particles in the plasma are not correlated over long distances, and the particle species in the plasma can be treated as interpenetrating fluids, characterized by and responding to macroscopic phenomena. A set of equations describing the macroscopic behavior of the plasma (density, temperature, flux) can be obtained by taking various velocity moments (integrals weighted by powers of the velocity) of the Boltzmann equation (Equation (4)). The resulting equations are known as the fluid equations. There are a variety of approaches used in implementing a fluid approach, and the approach discussed here is that followed by Golant, Zhilinsky

and Sakharov (13:155-180). The zeroth, first and second moments of the Boltzmann equation are taken with an assumed form for the velocity distribution and an equation of state (the ideal gas law), giving rise to the continuity, momentum transfer and energy equations, respectively. These equations are used along with Maxwell's equations and appropriate boundary conditions to provide a closed set of coupled nonlinear equations describing the macroscopic conditions in a plasma. The final set of equations is solved numerically using explicit or implicit finite differencing techniques.

For the fluid description to be valid, fluid-like behavior of the species modeled must dominate particle-like behavior (9:108). As already mentioned, the motions of particles must not be correlated over long distances. In addition, the collisional mean free path should be less than the scale of change of macroscopic quantities. These constraints insure that the description of the local condition of a plasma -- including the collision frequencies used to calculate ionization rates, momentum and energy transfer -- depends on local fields, densities and gradients. Finally, the number of particles in a sphere with a radius of a Debye length must be large (>>1) to ensure a small (with respect to interparticle forces) distance between particles. This last condition is simply a restatement of the plasma approximation, and allows the plasma to be treated as an ideal gas, consistent with the assumed equation of state(23:4).

Along with the considerations mentioned above, the rate coefficients (energy and momentum transfer between species, creation and loss of particles) and such average values as the fluid velocity, energy density and heat flux depend upon the functional form of the velocity distributions for which they were calculated. Whenever the assumed functional form of the velocity distributions differs significantly from the form of the distribution in the actual device being modeled, the results of the calculations are subject to error. In the bulk region of the ignited mode thermionic plasmas considered here, this form is said to be close to that given by a Maxwell-Boltzmann velocity distribution (42:657, 46:188). Norcross and Stone attribute this form to the short relaxation time for distribution of energy among electrons by electron-electron collisions(42:657).

Many models of thermionic converters have been formulated based on a fluid treatment of the bulk of the plasma in the inter-electrode space mated to a collisionless treatment of the sheaths. An early model was developed by Warner in 1968. Warner used transport equations derived from simplifications of the first three moments of the Boltzmann equation, solved self-consistently with Poisson's equation for the potential in the plasma (53:269-275, 54:931-938). At the cathode and anode, his model used expressions for calculating the current density to the electrode that can be derived from a collisionless sheath theory, using the assumption of a Maxwellian velocity distribution at the sheath edge

and a large sheath potential (see Chapter II, Equation (16) on page 48). His model predicted the approximate form of the current - voltage characteristic observed in experimental thermionic converters, but could not match the detailed behavior of the characteristic and did not treat the obstructed regime.

Lawless, in 1981 (30:II.2-II.16), developed a more detailed fluid model of the plasma in a thermionic converter that included a treatment of the obstructed regime and used a detailed treatment of the collisional processes in a cesium plasma (30:III.9). Like Warner, his model was based on the first three moments of the Boltzmann equation, solved self-consistently with Poisson's equation for the plasma potential, and his model for the bulk of the plasma was matched to a collisionless model for the sheaths.

Like Warner's model, Lawless' model did not correctly predict the detailed behavior of the current-voltage characteristic. Lawless used his model to examine the "faster-than-Boltzmann rise" of the current - voltage characteristic in the obstructed regime(see Figure 8 on page 17), and found that it could be accounted for in one dimension by altering the dependence in his model of the ionization rate constant to include the electron density as well as temperature. From this he deduced that a more detailed accounting of the ionization kinetics could lead to a more accurate description of the current - voltage characteristic without resorting to a two dimensional model.

In 1986, Lawless and Lam(29:1875-1889) developed a simplified version of Lawless' model and produced J-V curves for comparison to experimental data, using the ionization rate correlations of Norcross and Stone (42) and, again, relying on a collisionless model of the sheaths. They were able to reduce their description of the plasma to three governing algebraic equations. The J-V curves resulting from the solution of these equations were still unable to reproduce the detailed behavior of experimental curves.

In 1989, a new three region model was created at Wright Laboratories in an attempt at developing a converter model with better fidelity to experimental data than TECMDL (45:73-84) (TECMDL was introduced previously and is discussed on page 37). This new model explicitly treated the sheath regions using the Vlasov equation (a collisionless form of the Boltzmann equation), assuming the sheath thickness to be much smaller than an ion or electron mean free path. The bulk plasma was treated with an existing fluid model code, developed at Rasor Associates to model a pulse ionization converter. Details of the fluid model were not provided (in reference 45), but the fluid model was said to use a system of transport differential equations for electrons, ions and electron energy (196:22). This new code was used to model a standard converter, operating in the ignited mode, but performed no better than did TECMDL. Explicit modeling of the sheath did indicate, however, that the

assumption of collisionless sheaths may be incorrect, and that obstructed regime sheath thickness can extend to the order of an ion mean free path (45:84).

Phenomenological Models. Depending on the regime to be modeled, simplifications to the fluid description of a plasma may be made by combining empirical correlations with the more detailed analytic treatment. The resulting phenomenological models work very well as long as the regime of interest is narrowly defined, but predict performance relatively poorly at the regime boundaries. In general, these models treat the sheaths as infinitesimally thin and provide the flux and potential drop through the sheath as boundary conditions for their model of the bulk of the inter-electrode gap. The sheath boundary conditions are usually determined from collisionless analyses of the potential in the sheath given some assumed potential profiles; the results are thus tied to the assumptions going into the sheath formalisms, such as when the transition to the obstructed regime occurs, how the height of the potential barrier is determined, how thick the sheath actually is and whether the sheath is truly collisionless.

Perhaps the most widely used model of ignited mode thermionic converters has been the phenomenological model TECMDL, developed in 1965 by McVey, Britt and Rasor (46), and continually refined up to the present(45:67). This model was based on a more fundamental fluid treatment, said to originate from the first-principles treatment of Baksht, mated to a collisionless treatment of the sheaths (46:186,197), which are assumed to be infinitesimally thin.

TECMDL does a good job at predicting the performance of thermionic converters at the nominal operating point -- that is, the point of maximum power production, just above the "knee" on the J-V curve. But, as already mentioned, the actual shape of the J-V curve produced by TECMDL is incorrect. As illustrated in Figure 8 on page 17, the predicted J-V curve tends to fall off too slowly in the obstructed regime, and rise too quickly in the saturated regime.

Conclusion.

In this chapter we've briefly reviewed the operation of high-pressure, ignited mode thermionic converters and looked at some of the modeling that has been done in the past. While some models (TECMDL, fr example) do a good job of predicting the performance of ignited mode converters at the normal operating point, the fact that none of the models created to date do a very good job at predicting the behavior of ignited thermionic converters across either the saturation or obstructed regimes leads us to question the validity of the assumptions that went into the models. In particular, all the models reviewed used the results of collisionless sheath theories as boundary conditions for their treatments of the bulk plasma. It is of interest, then, to examine the structure predicted by a collisionless sheath model to see if such a treatment is appropriate. In the next chapter, a model is developed of collisionless anode and cathode sheaths consistent with the potentials, fields and temperatures

found in ignited thermionic converters. Using this model, an analysis of the predicted sheath structures is performed.

II. A Closed Collisionless Sheath Theory for Low Voltage Sheaths

Introduction.

All of the models of thermionic converters reviewed in the last chapter had two things in common: they used collisionless treatments for the cathode and anode sheaths, and they were not able to properly characterize the behavior of the current-voltage relationship in the saturated and obstructed regimes. In this chapter a detailed collisionless model of the cathode and anode sheaths is developed and validated. Based on this model, the suitability of the collisionless approach for modeling the sheaths in high-pressure thermionic converters is examined. To begin, the models of Langmuir, Prewett and Allen, and Main are reviewed, then elements of all three approaches are combined and extended to form a closed and consistent sheath theory. The predictions of this theory are compared to closed forms of previous analyses, and the theory is validated by comparison to PIC results. Finally, the sheath structures predicted by the theory are examined by comparing the predicted sheath thickness to the electron and ion mean free paths.

Past Models.

In 1929, Langmuir developed a theory that predicted the ratio of the thermionic electron emission current density to the plasma ion current density under space charge limited conditions in a hot cathode sheath, and calculated

the electric field and potential profiles, parameterized in terms of the ratio of the random electron current density to the ion current density (28:140-175). He assumed both the ion current density from the plasma and the electron current density emitted from the cathode were space charge limited, so the electric field at the sheath/plasma boundary and at the cathode vanished. Langmuir's analysis explicitly considered the initial velocity distribution of the cathode electrons, and assumed the ions entered the sheath with a fixed but unspecified initial velocity. To simplify his analysis, he assumed a cathode fall potential that was large when compared to the plasma and cathode emission electron temperatures. His results showed the inclusion of the initial velocities of the ions and electrons limited the emission current density to a fraction of that predicted when the initial velocities were ignored.

In 1976, Prewett and Allen (44:435-446) revisited the sheath theory of Langmuir, again assuming a relatively large cathode potential fall. Unlike Langmuir, they ignored the initial velocity of the cathode emission electrons, but they extended his work by explicitly calculating the initial ion velocity required to cause the electric field to vanish at the plasma/sheath boundary. Further, they extended the analysis to include cathode emission current densities that were not space charge limited (non-zero electric fields at the cathode). Their work assumed the cathode fall was known apriori, and their results were parameterized in terms of its value.

More recently, in 1984, Main developed a sheath theory (35) that extended previous sheath analyses by explicitly considering the asymmetry of the electron velocity distribution at the sheath edge in the presence of a small cathode voltage . Like Langmuir, Main explicitly considered the initial velocity distribution of the cathode electrons. Main went further, however, and also

considered an initial velocity distribution for the ions from the plasma as well. He assumed the ions entered the sheath with a 'chopped' Maxwellian velocity distribution – that is, a distribution function that vanishes below some lower cutoff velocity, and is Maxwellian above that velocity. He didn't explicitly calculate the value of the cutoff, but showed a velocity cutoff is necessary for a self consistent sheath solution to exist(35:3.16). Physically, the velocity cutoff insures a minimum drift velocity and average energy for the ions at the sheath edge, consistent with a generalized version of the Bohm criterion(35:3.11). Main parameterized his equations in terms of the potential drop between the plasma/cathode sheath boundary and the cathode surface, and used his model to examine the influence of trapped ions and ion reflection on the emission current density. He didn't explicitly calculate the value of the electric field in the sheath, or the average ion velocity required to cause the electric field at the plasma/sheath boundary to vanish.

The analyses of Langmuir, Prewett and Allen, and Main all fall somewhat short in providing a self consistent, closed set of equations for calculating the sheath characteristics in low voltage plasma modeling. The assumptions of relatively large cathode falls in Prewett and Allen and in Langmuir's work preclude their use, and the parameterization by Prewett and Allen, and by Main in terms of undetermined potential differences in the sheath require additional information about the potential profile to enable closure.

The Collisionless Sheath Model.

The model developed here is designed to be applicable to three potential profiles found in the cesium plasma sheaths of low voltage, ignited mode thermionic converters. These profiles are illustrated in Figure 10, in which J_E represents the electron emission current density from the cathode in cases (a) and (b), and from the virtual cathode in case (c), V_E is the electron potential at which the emission current density is specified -- either at the cathode or, in case (c), the virtual cathode potential, and x_0 is the location of the plasma/sheath boundary. Note that the notation in this analysis of the collisionless sheath basically follows Langmuir's notation. Structures and densities are calculated in terms of the electron potential, which is defined as the negative of the normal potential; an electron at a large electron potential has a large potential energy.

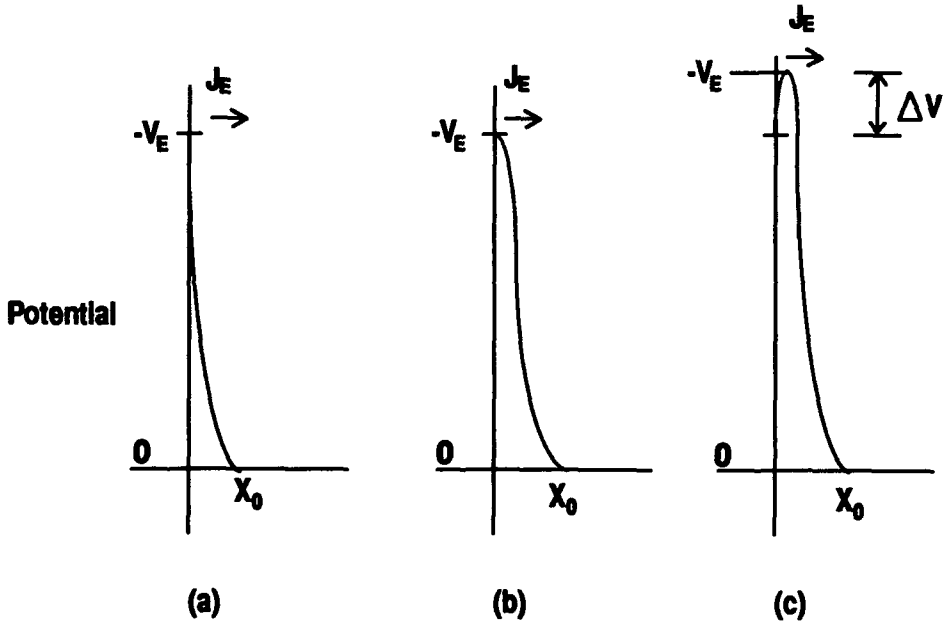

Figure 10. Potential Profiles Considered by Sheath Model.

The profile represented by case (a) is a single, electron repelling sheath such as exists at the cathode in the "saturation" regime of operation of a thermionic diode. This potential profile is also characteristic of the cool anode with an electron-repelling sheath. The emission current density is usually negligible at the anode and will be ignored in this analysis. Cases (b) and (c) apply strictly to the hot cathode. Case (b) represents an electron repelling sheath with the electric field at the cathode surface equal to zero, as occurs at the transition point in a thermionic diode. Case (c) exhibits the formation of a virtual cathode, with an electron potential barrier between the true cathode and the point where the electric field first vanishes (the 'virtual' cathode). This profile is believed to occur in the obstructed regime of operation of a thermionic converter(46:175).

In case (b), the current density entering the plasma from the electrode is the thermionic current density predicted by Equation (1), the Richardson-Dushman equation(46:172). In case (a), for a hot cathode, J_E is actually greater than the value predicted by the Richardson equation because of the electric field at the cathode surface. The increase in the emission current density results from what is known as the Schottky effect -- the presence of the accelerating electric field reduces Φeff such that

$$\Phi eff = \Phi cathode - \sqrt{\frac{e^3 E}{4\pi \varepsilon_0}} \qquad (5)$$

where e is the electronic charge, ε_0 is the permittivity of free space, and E is the electric field at the cathode (3:25). In case (c), J_E is substantially less than that predicted by Richardson's equation because of the potential barrier just outside the cathode. The barrier reduces the emission current density, effectively

increasing the work function by the height of the potential barrier:

$\Phi eff = \Phi cathode + e\Delta V$.

Charged Particle Density In The Sheath

Ignoring surface emission of ions and the possibility of ion trapping in the obstructed regime (case (c)), the charged particle density in the sheath and at the sheath edge can be broken into three components: emission electrons from the cathode, plasma electrons, and plasma ions. Each of these contributions must be considered separately in calculating the charge density for use with Poisson's equation.

Emission Electrons (Cathode only). If the emission electrons from the cathode are represented by a single sided Maxwellian velocity distribution, then their density at the maximum electron potential (V_E: see Figure 10.) is the emission current density divided by the average electron velocity:

$$n_E(V_E) = \frac{J_E}{e}\sqrt{\frac{\pi m_e}{2kT_E}}. \qquad (6)$$

Between electron potential V_E and the sheath/plasma boundary, the emission electron density can be found by integrating over velocity space the contribution of each differential density element with initial velocity within dv_x about v_x to the density at electron potential V, where the new velocity of the differential density element is given by $v_x' = (v_x^2 + 2 e (V_E - V)/m_e)^{1/2}$, resulting in the expression:

$$n_E(V) = 2n_E(V_E)\int_0^{\infty}\sqrt{\frac{m_e}{2\pi kT_E}}\frac{Exp\left[-\frac{m_e v_x^2}{2kT_E}\right]}{\left(v_x^2 + \frac{2e}{m_e}(V_E - V)\right)^{1/2}} v_x dv_x \qquad (7)$$

Or, with a substitution for v_x' and dv_x'

$$n_E(V) = n_E(V_E)Exp\left[\frac{V_E - V}{E_E}\right]\left(1 - Erf\left[\left(\frac{V_E - V}{E_E}\right)^{1/2}\right]\right) \qquad (8)$$

where $E_E = \frac{kT_E}{e}$.

At the sheath edge the potential vanishes, and the emission electron density becomes:

$$n_E(0) = n_E(V_E)Exp\left[\frac{V_E}{E_E}\right]\left(1 - Erf\left[\left(\frac{V_E}{E_E}\right)^{1/2}\right]\right) \qquad (9)$$

Plasma Electrons. At the edge of a plasma in which the electron temperature is comparable to the sheath height, the fraction of electrons with energy great enough to escape over the potential barrier is significant. Following Main's analysis(35), the total electron density in the sheath due to plasma electrons is :

$$n_e(V) = n_e^+(V) + n_e^-(V) \qquad (10)$$

where $n_e^-(V)$ is the density of electrons moving from the plasma towards the sheath at electron potential V, and $n_e^+(V)$ is the density of electrons from the plasma moving away from the sheath towards the plasma at electron potential V.

Taking the reflection of electrons by the sheath potential into account, and assuming a Maxwellian electron velocity distribution in the plasma with temperature T_e, the density of electrons moving towards the electrode is:

$$n_e^-(V) = 2n_e^-(0) \int_{\sqrt{\frac{2Ve}{m}}}^{\infty} \sqrt{\frac{m_e}{2\pi kT_e}} \frac{Exp\left[-\frac{m_e v_x^2}{2kT_e}\right]}{\left(v_x^2 - \frac{2eV}{m_e}\right)^{1/2}} v_x dv_x \tag{11}$$

and, for electrons moving away from the electrode:

$$n_e^+(V) = 2n_e^-(0) \int_{\sqrt{\frac{2Ve}{m}}}^{\sqrt{\frac{2V_E e}{m}}} \sqrt{\frac{m_e}{2\pi kT_e}} \frac{Exp\left[-\frac{m_e v_x^2}{2kT_e}\right]}{\left(v_x^2 - \frac{2eV}{m_e}\right)^{1/2}} v_x dv_x \tag{12}$$

where $n_e^-(0)$ is $n_e^-(V)$ evaluated at V=0.

Then the fraction (α) of the plasma electron density at the sheath edge moving towards the sheath is given by:

$$\alpha \equiv \frac{n_e^-(0)}{n_e^-(0) + n_e^+(0)} = \left(1 + Erf\left[\left(\frac{V_E}{E_e}\right)^{1/2}\right]\right)^{-1} \tag{13}$$

where $E_e \equiv \frac{kT_e}{e}$.

Substituting $\alpha\, n_e(0)$ for $n_e^-(0)$, the plasma electron density is given by:

$$n_e(V) = n_{e0}\alpha \exp\left(\frac{-V}{E_e}\right)\left(1 + Erf\left[\left(\frac{V_E - V}{E_e}\right)^{1/2}\right]\right) \tag{14}$$

where $n_{e0} \equiv n_e(0)$. The plasma current density that escapes over the electrode potential is:

$$J_{ep} = e\frac{\bar{v}}{2}\alpha\ n_e(0)\ Exp\left[\frac{-V_E}{E_e}\right] \tag{15}$$

where $\bar{v} \equiv \sqrt{\frac{8kT_e}{\pi m_e}}$. In the limit of a large electrode potential, $\alpha \Rightarrow ½$, and the above expression reduces to the familiar:

$$J_{ep} = e\frac{\bar{v}}{4} n_e(0)\, Exp\left[\frac{-V_E}{E_e}\right] \tag{16}$$

Plasma Ions. Given a monoenergetic ion current density (J_i) with initial kinetic energy eV_0 at the plasma/sheath boundary, the ion density after falling through an additional potential drop of V is simply(28:160):

$$n_i(V) = n_{i0}\left(1+\frac{V}{V_0}\right)^{-½} \tag{17}$$

where

$$n_{i0} \equiv \frac{J_i}{e}\sqrt{\frac{m_i}{2V_0 e}} \tag{18}$$

is the density of the ions entering the sheath.

Total Charge Density. Combining the equations for ion and electron densities, and Poisson's equation (noting that the potential is the negative of the electron potential V), the charge density in the cathode sheath is given by:

$$\varepsilon_0\frac{\partial}{\partial x}\frac{\partial V}{\partial x} = \rho = \frac{en_{i0}}{\left(1+\frac{V}{V_0}\right)^{½}} - J_E\sqrt{\frac{\pi m_e}{2eE_E}}Exp\left[\frac{V_E - V}{E_E}\right]\left(1-Erf\left[\left(\frac{V_E - V}{E_E}\right)^{½}\right]\right) - en_{e0}\alpha\, Exp\left[\frac{-V}{E_e}\right]\left(1+Erf\left[\left(\frac{V_E - V}{E_e}\right)^{½}\right]\right) \tag{19}$$

and the charge density in the anode sheath is given by:

$$\rho = \frac{en_{i0}}{\left(1+\frac{V}{V_0}\right)^{½}} - en_{e0}\alpha\, Exp\left[\frac{-V}{E_e}\right]\left(1+Erf\left[\left(\frac{V_E - V}{E_e}\right)^{½}\right]\right) = \varepsilon_0\frac{\partial}{\partial x}\frac{\partial V}{\partial x} \tag{20}$$

Calculation of the Electric Field in the Sheath

The electric field may now be calculated as a function of electron potential between the sheath/plasma boundary and the electron potential maximum V_E by integrating Gauss' Law ($\nabla \bullet E = \rho/\epsilon_0$) over the electron potential, resulting in the expression:

$$\frac{1}{2}E^2 = \int_0^V \frac{\rho(\eta)}{\varepsilon_0} d\eta \tag{21}$$

Two functions, Erm and Erp, are introduced to facilitate the discussion. These functions are defined as follows:

$$Erm[x] = Exp[x]\left(1 - Erf\left[\sqrt{x}\right]\right) \tag{22}$$

$$Erp[x] = Exp[x]\left(1 + Erf\left[\sqrt{x}\right]\right) \tag{23}$$

and have the following helpful properties :

$$\frac{d}{dx}Erm[x] = \left(Erm[x] - \frac{1}{\sqrt{\pi x}}\right) \tag{24}$$

$$\frac{d}{dx}Erp[x] = \left(Erp[x] + \frac{1}{\sqrt{\pi x}}\right) \tag{25}$$

$$\int Erm[x]dx = Erm[x] + 2\sqrt{\frac{x}{\pi}} + C \tag{26}$$

$$\int Erp[x]dx = Erp[x] - 2\sqrt{\frac{x}{\pi}} + C \tag{27}$$

where C is an integration constant.

Using the requirement for charge neutrality at the plasma boundary to express en_{e0} in terms of J_E and J_i :

$$en_{e0} = \left[J_i\sqrt{\frac{m_i}{2V_0 e}} - J_E\sqrt{\frac{\pi m_e}{2eE_E}}\,Erm\left[\frac{V_E}{E_E}\right]\right] \tag{28}$$

and assuming the electric field is negligible at the sheath/plasma boundary, Equation (21) can be evaluated using the expression in Equation (19) for the

charge density to arrive at the following expression for the electric field between the cathode (or, if one exists, virtual cathode) and the sheath edge:

$$\frac{\varepsilon_0}{2}E^2 = J_i\sqrt{\frac{m_i}{2V_0 e}}2V_0\left(\sqrt{1+\frac{V}{V_0}}-1\right)+$$
$$J_E E_E\sqrt{\frac{\pi m_e}{2eE_E}}\left(Erm\left[\frac{V_E-V}{E_E}\right]+\sqrt{\frac{4(V_E-V)}{\pi E_E}}-Erm\left[\frac{V_E}{E_E}\right]-\sqrt{\frac{4V_E}{\pi E_E}}\right)+$$
$$\left(J_i\sqrt{\frac{m_i}{2V_0 e}}-J_E\sqrt{\frac{\pi m_e}{2eE_E}}Erm\left[\frac{V_E}{E_E}\right]\right)\frac{E_e}{Erp\left[\frac{V_E}{E_e}\right]}\times$$
$$\left(Erp\left[\frac{V_E-V}{E_e}\right]-\sqrt{\frac{4(V_E-V)}{\pi E_e}}-Erp\left[\frac{V_E}{E_e}\right]+\sqrt{\frac{4V_E}{\pi E_e}}\right) \qquad (29)$$

Equations (28) & (29) can be used to calculate the field in the anode sheath by setting the emission current density (J_E) and the terms it multiplies to zero.

Boundary Conditions

Charge neutrality at the sheath edge dictates $\rho=0$ at $V=0$. Inserting this boundary condition into Equations (19) & (20) yields :

$$\frac{n_{i0}}{n_{e0}} = \frac{J_E}{en_{e0}}\sqrt{\frac{\pi m_e}{2eE_E}}Erm\left[\frac{V_E}{E_E}\right]+1 \qquad (30)$$

at the cathode sheath/plasma boundary, and:

$$n_{i0}=n_{e0} \qquad (31)$$

at the anode sheath/plasma boundary.

Invoking the additional condition, $\frac{d\rho}{dV}=0$ at $V=0$ (2:463), together with Equation (30) results in an expression for V_0, the potential drop corresponding

to the ion velocity at the sheath edge:

$$V_0 = \frac{\frac{J_E}{en_{e0}}\sqrt{\frac{\pi m_e}{2eE_E}}Erm\left[\frac{V_E}{E_E}\right]+1}{\frac{2J_E}{eE_E n_{e0}}\sqrt{\frac{\pi m_e}{2eE_E}}\left[Erm\left[\frac{V_E}{E_E}\right]-\sqrt{\frac{E_E}{\pi V_E}}\right]+\frac{2}{E_e}\left[1+\sqrt{\frac{E_e}{\pi V_E}}\left(Erp\left[\frac{V_E}{E_e}\right]\right)^{-1}\right]} \quad (32)$$

at the cathode sheath/plasma boundary, and:

$$V_0 = \left(\frac{2}{E_e}\left[1+\sqrt{\frac{E_e}{\pi V_E}}\left(Erp\left[\frac{V_E}{E_e}\right]\right)^{-1}\right]\right)^{-1} \quad (33)$$

at the anode sheath/plasma boundary.

Closing the System of Equations

Closure of the system of equations requires a knowledge of boundary conditions of the application being modeled, including electron and ion temperatures, and the ion current density at the sheath edge. For conditions in a typical ignited mode, thermionic converter using a cesium plasma, the ion current density at the sheath edge can be approximated by summing the transport equations for electrons and ions to arrive at the following relations:

$$Ji = \left(1+\frac{\mu_i}{\mu_e}\right)^{-1}\left(\frac{\mu_i}{\mu_e}J_{ext}+\pi eD_a\frac{n_{max}}{d}\right) \quad (34)$$

for the ion current density at the cathode, and:

$$Ji = \left(1+\frac{\mu_i}{\mu_e}\right)^{-1}\left(\pi eD_a\frac{n_{max}}{d}-\frac{\mu_i}{\mu_e}J_{ext}\right) \quad (35)$$

for the ion current density at the anode hese equations, μ_i and μ_e are the ion and electron mobilities, d is the width of the inter-electrode gap, D_a is the ambipolar diffusion coefficient, J_{ext} is the external circuit current divided by the electrode area, and n_{max} is the maximum electron density in the plasma. The

electron density profile in the plasma is approximated by $n \approx n_{max} \sin\left(\frac{\pi x}{d}\right)$ to calculate the diffusion contribution to the ion current density. Current continuity at the cathode surface, combined with Equation (15) for J_{ep}, yields an expression for the plasma electron density at the cathode sheath edge:

$$n_{e0} = \frac{2}{ev} Erp\left[\frac{V_E}{E_e}\right]\left(J_E + J_i - J_{ext}\right) \tag{36}$$

and at the anode sheath edge:

$$n_{e0} = \frac{2}{ev} Erp\left[\frac{V_E}{E_e}\right]\left(J_i - J_{ext}\right) \tag{37}$$

Combining this result with the expression for charge neutrality, Equation (30), establishes the ion density at the sheath boundary:

$$n_{i0} = \frac{J_E}{e}\sqrt{\frac{\pi m_e}{2eE_E}}\, Erm\left[\frac{V_E}{E_E}\right] + n_{e0} \tag{38}$$

at the cathode sheath/plasma boundary, and:

$$n_{i0} = n_{e0} \tag{39}$$

at the anode sheath/plasma boundary.

Rewriting Equation (32) using Equation (30), and the definition $V_0 \equiv \frac{J_i^2 m_i}{2e^3 n_{i0}^2}$, the following condition is derived relating the cathode fall, V_E, to the emission current density, J_E:

$$\frac{J_i^2 m_i}{e} = \frac{\left(en_{i0}\right)^3}{\frac{J_E}{E_E}\sqrt{\frac{\pi\, m_e}{2eE_E}}\left[Erm\left[\frac{V_E}{E_E}\right] - \sqrt{\frac{E_E}{\pi\, V_E}}\right] + \frac{en_{e0}}{E_e}\left[1 + \sqrt{\frac{E_e}{\pi\, V_E}}\left(Erp\left[\frac{V_E}{E_e}\right]\right)^{-1}\right]} \tag{40}$$

at the cathode, and:

$$\frac{J_i^2 m_i}{e} = E_e\left(en_{e0}\right)^2\left[1 + \sqrt{\frac{E_e}{\pi\, V_E}}\left(Erp\left[\frac{V_E}{E_e}\right]\right)^{-1}\right]^{-1} \tag{41}$$

at the anode.

For the anode case, Equation (41) together with Equations (35) and (37) fix the anode potential fall, V_E. Another independent equation is needed for the cathode, however, because there are two unknowns, V_E and J_E.

The second relation can be derived by evaluating the electric field at the cathode and specifying its value in the obstructed and saturated regimes. In the obstructed regime, the electric field vanishes at the virtual cathode. In the saturated regime, the electric field, together with the emission current density, satisfies the relation prescribing the Schottky-enhanced emission current density:

$$J_E = AT_E^{\,2} Exp\left[\frac{-\Phi_E}{kT_E}\right] Exp\left[\frac{\sqrt{eE}}{\sqrt{4\pi\varepsilon_0}E_E}\right]$$

$$\frac{\varepsilon_0}{2}E^2 = \frac{\varepsilon_0}{2e^2}\left(\sqrt{4\pi\varepsilon_0}E_E Ln\left[J_E\left(AT_E^{\,2} Exp\left[\frac{-\Phi_E}{kT_E}\right]\right)^{-1}\right]\right)^4 \qquad (42)$$

where Φ_E is the emitter (cathode) work function, and E is the electric field at the cathode. Imposing these constraints on Equation (29) (evaluated at the cathode) yields the second independent equation V_E and J_E must satisfy:

$$2en_{i0}V_0\left(\sqrt{1+\frac{V_E}{V_0}}-1\right)+J_E E_E\sqrt{\frac{\pi m_e}{2eE_E}}\left(1-Erm\left[\frac{V_E}{E_E}\right]-\sqrt{\frac{4V_E}{\pi E_E}}\right)+$$

$$\frac{en_{e0}E_e}{Erp\left[\frac{V_E}{E_e}\right]}\left(1-Erp\left[\frac{V_E}{E_e}\right]+\sqrt{\frac{4V_E}{\pi E_e}}\right)=\begin{cases}\dfrac{\varepsilon_0}{2e^2}\left(\sqrt{4\pi\varepsilon_0}E_E Ln\left[\dfrac{J_E}{J_R}\right]\right)^4 \\ 0\end{cases} \qquad (43)$$

where J_R is the current density predicted by Richardson's equation (Equation (1)) and the upper equation in the brace on the right hand side applies to a device operating in the saturated regime while the lower applies in the obstructed regime.

Equations (40) and (43) can be solved simultaneously for J_E and V_E, using the definitions of J_i, n_{io}, n_{eo} and V_0 presented above, for given values of Φ_E, T_e, T_i, and n_{max}. Once the relationship for the electric field as a function of electron potential is known, the sheath thickness can found by numerically evaluating the formula:

$$x_0 = V_E/100 \int^{V_E} (E(V))^{-1}\, dV. \qquad (44)$$

in which the sheath thickness is defined as the distance in which the electron potential falls to 1 % of its maximum value V_E.

Discussion

Comparison of Results for Space Charge Limited Conditions. Under conditions in which the electric field vanishes at the cathode as well as at the plasma / sheath boundary, both the emission current density of electrons from the cathode (or virtual cathode) and the ion current density from the plasma are space charge limited. Evaluating Equation (43) for this case, substituting in for the electron and ion densities in terms of the electron and ion current densities, establishes a relationship between the electron current density from the cathode and the ion current density from the plasma, similar to the one derived by Langmuir in 1929:

$$\frac{J_E}{J_i} = \sqrt{\frac{m_i}{m_e}} \frac{\sqrt{\frac{E_E}{\pi V_0}}\left[-2V_0\left(\sqrt{1+\frac{V_E}{V_0}}-1\right) - E_e\left(\frac{1+\sqrt{\frac{4V_E}{\pi E_e}}}{Erp\left[\frac{V_E}{E_e}\right]}-1\right)\right]}{E_E\left[1-\sqrt{\frac{4V_E}{\pi E_E}}-Erm\left[\frac{V_E}{E_E}\right]\right] - E_e\left(\frac{1+\sqrt{\frac{4V_E}{\pi E_e}}}{Erp\left[\frac{V_E}{E_e}\right]}-1\right)Erm\left[\frac{V_E}{E_E}\right]} \tag{45}$$

It is interesting to evaluate this relationship over a range of cathode fall voltages, and compare the result to the similar results based on Langmuir's and Prewett and Allen's analyses for the case where the electric field vanishes at the cathode. To make this comparison, both Langmuir's and Prewett and Allen's analyses must first be closed. For Langmuir's analysis, closure is achieved simply by specifying a value for V_0. For simplicity, the value calculated using the model developed above is used. To close Prewett and Allen's analysis, the same procedure used to close the analysis presented above is used; known electron temperatures and a consistent ion current density and external circuit current are assumed. Unknown are the emission current density, the cathode fall voltage, the electron and ion density at the sheath edge, and the initial ion energy. The constraint of current continuity is used to eliminate the electron density, expressing it in terms of the cathode fall, the ion and emission current densities, and the current in the external circuit. Next, the condition of charge neutrality at the plasma-sheath boundary is used to eliminate the ion density, expressing it, too, in terms of the cathode fall, the ion and emission current densities, and the current in the external circuit. This leaves the initial ion energy, the emission current density and cathode fall as unknowns. The initial

ion energy is eliminated by equating Prewett and Allen's expression for the initial ion energy, (44:439 Equation (26)) to the definition of the ion energy in terms of the ion current density, derived from Equation (18). This gives an equation relating the emission current density to the cathode fall. A second equation relating the emission current density to the cathode fall is obtained from the constraint that the electric field (44:440 Equation (28)) vanishes at the cathode, and the system of equations is closed.

To compare the closed form of Prewett and Allen's analysis to present analysis and to Langmuir's, the value of J_E/n_{e0} that causes the electric field to vanish at the cathode is determined, and used to calculate V_0 for use in the expression for $\frac{J_E}{J_i}\sqrt{\frac{m_e}{m_i}}$ (Prewett and Allen 44:441 Equation (31), Langmuir (28:162) Equation (66)). Figure 11 presents the results of our comparison by plotting the normalized ratio of the emission to ion current density as a function of the cathode fall voltage. Also plotted in the figure is the result of a version of the present analysis which ignores the asymmetry of the plasma electron velocity distribution at the sheath edge.

As already mentioned, since Langmuir didn't specify a value for V_0, the value of V_0 calculated for this analysis was used in his equations, however, use of Prewett and Allen's value in Langmuir's equation makes no significant difference in the results presented here.

The results of the analysis by Prewett and Allen differ significantly from both Langmuir's and the present analysis, even at large cathode fall voltages. The principle reason for the difference is that Prewett and Allen neglected the temperature of the emission electrons. The symmetric analysis is essentially Langmuir's analysis with his series expansions replaced with the full analytic

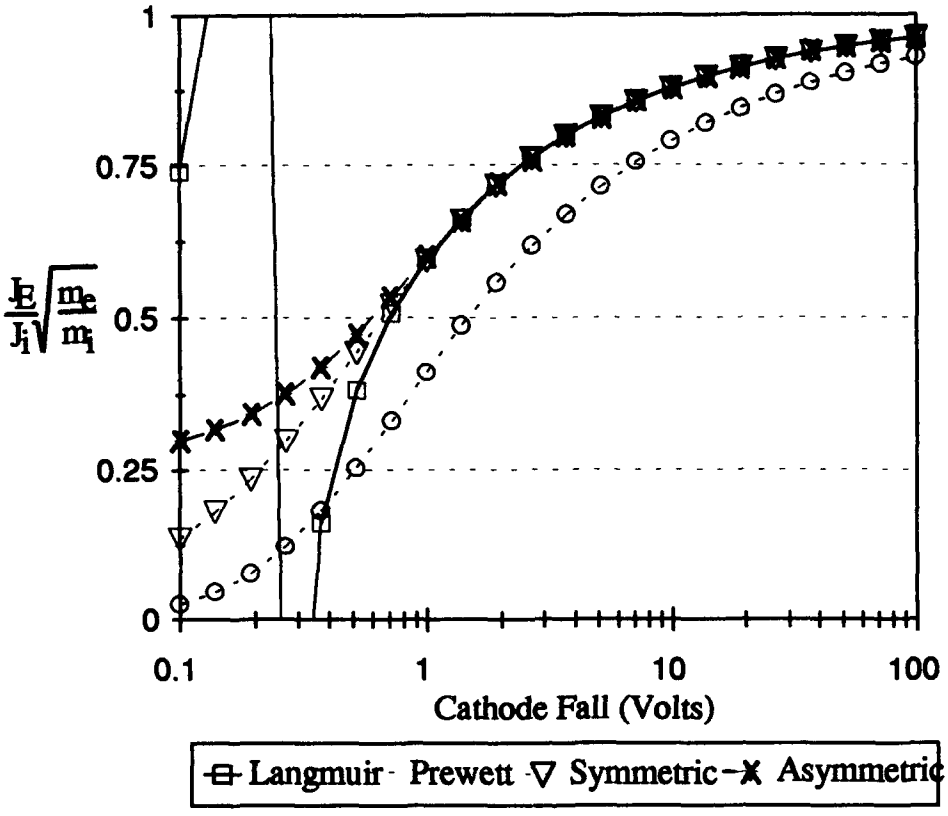

Figure 11. Comparison of the Results of Previous Sheath Theories to the Present Theory. T_E=1700K, T_e=3000K

expressions. Thus, it only differs from Prewett and Allen's analysis by the inclusion of the emission electron initial energy. If the energy of the emission electrons is small the two analyses should agree. When the comparison displayed in Figure 11 was repeated with a cold velocity distribution (10 Kelvin) assigned to the emission electrons in Langmuir's and the present analysis, the trace representing the results of Prewett and Allen's analysis overlaid the trace of the symmetric analysis across the entire range of cathode fall voltage examined, from 100 volts down to 0.1 volt.

Langmuir's analysis and the current work agree almost exactly at cathode falls greater than one volt, but diverge below 1 volt. With an electron temperature of 3000 K, as in Figure 11, a cathode fall of one volt corresponds to an eV_E/kT_e ratio of about 4. Because he was interested in eV_E/kT_e ratios greater than ~10, Langmuir used series expansions of various terms in his formulation. Those expansions result in a pole in his solution at about 0.25 volts, which explains part of the divergence. The trace in Figure 11 labeled "Symmetric" is essentially Langmuir's analysis with his series expansions replaced with the full analytic expressions. This trace still diverges from that of the present analysis at low voltages, as a result of the neglect of the asymmetry of the plasma electron velocity distribution in Langmuir's analysis.

As can be seen from Figure 11, all the solutions which ignore the asymmetry in the plasma electron velocity distribution predict ratios which vanish with the vanishing cathode fall, while the solution from this analysis tends to a non-zero value. This behavior can be justified by analyzing the asymptotic behavior of V_0 (the potential corresponding to the initial energy of the ion current density from the plasma). For a physically meaningful solution and a non zero ion current density, V_0 must remain finite and positive. A negative value would clearly be nonphysical, leading to a negative initial energy for the ions, while an infinite value would imply an ion density at the sheath edge of zero (and thus violate charge neutrality unless the plasma density itself vanished, leaving no sheath to consider). A value of zero would imply that the ion current density vanished, with the ions becoming a stationary neutralizing background, or that the ion density became infinite.

As the arguments of the Erm and Erp functions vanish, the values of both functions approach 1. Defining $J_b = \frac{J_E}{en_{e0}}\sqrt{\frac{\pi m_e}{2eE_E}}$ and substituting the limiting values for the Erp and Erm functions as $V_E \Rightarrow 0$, Equation (32) becomes

$$V_0 = \frac{J_b + 1}{\frac{2J_b}{E_E}\left[1 - \sqrt{\frac{E_E}{\pi V_E}}\right] + \frac{2}{E_e}\left[1 + \sqrt{\frac{E_e}{\pi V_E}}\right]} \tag{46}$$

The only way for the right hand side of this equation to have a non zero value as $V_E \Rightarrow 0$ is for the terms multiplying the radicals in the denominator to cause them to cancel each other, leading to the only possible non-zero solution:

$$J_b = \sqrt{\frac{E_E}{E_e}} \tag{47}$$

Values of J_b greater than this relation cause the value of V_0 to become negative, and so are non-physical. Values less than this cause the value of V_0 to vanish as $V_E \Rightarrow 0$. Substituting this value into the equation for V_0, and taking the limit, as $V_E \Rightarrow 0$ gives:

$$V_0 = \frac{\sqrt{\frac{E_E}{E_e}} + 1}{2\left[\frac{1}{\sqrt{E_E E_e}} + \frac{1}{E_e}\right]} \tag{48}$$

If the plasma and cathode temperatures are equal ($E_e = E_E$), $eV_0 = kT_e/2$, the energy corresponding to the Bohm velocity. This is an interesting result, because it suggests that in the limit of a vanishing cathode sheath with the emission and plasma electrons at the same temperature, a consistent solution requires the translational energy of the ions to match the average thermal energy of the electrons in a given direction. If the ion distribution were a thermal distribution instead of a beam, this would suggest the ions were in thermal equilibrium with the electrons in this limiting case.

The value for J_b from Equation (47) determines a relationship between J_E and J_{e0}, the limiting value of the electron current density from the plasma as the sheath vanishes:

$$J_{e0} = en_{e0}\sqrt{\frac{2eE_e}{\pi m_e}} \quad \Rightarrow \quad \sqrt{\frac{E_E}{E_e}} = \frac{J_E}{J_{e0}}\sqrt{\frac{E_e}{E_E}} \quad \Rightarrow \quad J_{e0} = J_E\frac{E_e}{E_E} \qquad (49)$$

If the cathode and plasma electron temperatures are equal, this predicts the emission and plasma electron current densities will be equal as well. This, together with the result for the ion energy presented above, suggests what this limiting case represents. The case where the cathode fall vanishes and in which the emission temperature matches the plasma electron temperature is analogous to an analysis of the electron current densities in the middle of a plasma, in which the emission and plasma electron current densities degenerate to the random electron current density. Because the asymmetry of the plasma electron distribution was included in this analysis, the plasma electron velocity distribution becomes a single sided Maxwellian in the limit of a vanishing cathode potential, as is the emission electron velocity distribution from the cathode. Taken together, they represent a full Maxwellian distribution at the plasma sheath boundary. Other analyses, such as Prewett and Allen, and Langmuir, assumed a full Maxwellian distribution at the plasma sheath boundary due to the plasma electrons alone. Pursuing the analogy, if the emission current density from the present analysis takes the place of half of the plasma current density in Prewett and Allen's analyses, then one would predict that in their analysis the limiting value of their emission current density would be zero, as, in fact, it is, because sufficient electron current density is supplied from their assumed form of the plasma electron velocity distribution (a full Maxwellian) to satisfy the plasma sheath boundary conditions. Taking this

analogy a bit further, then application of Prewett and Allen's analysis to a non emitting cathode in the limit of a vanishing cathode fall should produce a value for V_0 of $E_e/2$, because in that limit their analysis is analogous to our analysis of an electron emitting cathode for equal emitter and plasma electron temperatures. An examination of Prewett and Allen's results for a non emitting cathode in the limit of a vanishing sheath yields for V_0 of $E_e/2$, as predicted.

Invoking charge neutrality, and substituting in for the plasma electron current density using Equation (49), the following relationship can be derived for the ratio of the emission current density to the ion current density in the limit as the cathode fall vanishes:

$$\frac{J_E}{J_i}\left(\frac{m_e}{m_i}\right)^{1/2} = \frac{\sqrt{2\left[\frac{1}{\sqrt{E_E E_e}} + \frac{1}{E_e}\right]}}{\left(\frac{E_e}{E_E}\sqrt{\frac{\pi}{E_e}} + \sqrt{\frac{\pi}{E_E}}\right)\sqrt{\left(\frac{E_E}{E_e}\right)^{1/2} + 1}} \qquad (50)$$

In the comparison of the space-charge limited current ratios presented above, T_E = 1700 K and T_e = 3000 K, leading to an asymptotic value for the ratio of 0.297, in exact agreement with the limiting value from the full analysis.

Comparison of Cathode Sheaths in the Obstructed Mode. As mentioned previously, the method of closing the equations described for the present analysis can be applied equally well to Prewett and Allen's analysis. For notational convenience, this closed form of Prewett and Allen's analysis will be referred to as P&AC (for Prewett and Allen, Closed) in the remainder of this chapter. A comparison of the results of the P&AC analysis to those of the present analysis for two obstructed mode diode configurations is presented in Table 2. The present analysis yields results that differ from the P&AC analysis

by a factor of 3/2 for the emission current density and a factor of 3 for the cathode fall voltage.

Table 2. Comparison to P&AC Analysis in the Obstructed Mode.

J_{ext} (amp cm^{-2}):	2	5	2	5
	J_E(amp cm^{-2})		V_E (volts)	
P&AC Analysis	2.8	7.9	0.4	0.35
Present Analysis	4.3	13.4	0.13	0.11

T_e=2800K, T_i=1300K, Cesium Pressure=2 torr, d=254 microns, with elastic cross sections of 4.0×10^{-18} m^2 for electron-atom collisions and 1.2×10^{-17} m^2 for ion-atom collisions. For J_{ext}=2 amp cm^{-2}, $n_{max}= 4.0\times10^{19}$ m^{-3}. For J_{ext}= 5 amp cm^{-2}, $n_{max}= 1.3\times10^{20}$ m^{-3}.

Comparison to Particle In Cell (PIC) Calculation for Cathode Sheaths. To further examine the results of the P&AC analysis and the present analysis, a one dimensional particle-in-cell (PIC) computer code (based on the code PDP1 (52)) was used to model the cathode sheaths under conditions typical for cesium plasma thermionic converters. The systems of equations for both this analysis and P&AC's analysis were solved for the plasma sheath boundary conditions to be used in the PIC model. Given the external circuit current, cesium pressure, plasma electron density, and cathode and plasma electron temperatures, the analytic calculations produced the following values for use with the PIC code: plasma electron and ion current density at the sheath edge, plasma ion velocity at the sheath edge, electron emission current density and sheath thickness. These values, along with the external circuit current, were supplied as boundary conditions to the PIC code, which then calculated the electric field and potential

profiles in the sheath, and provided their values at the electrode. The analytic results also produced sheath electric field and potential profiles, and their values at the electrode. A comparison of the PIC results to the analytic results provides a check on the self consistency of the analytic models. A 'good' analytic model should produce results that are consistent with the values predicted by the PIC calculation.

The PIC calculations were performed with time-steps of a picosecond and 100 spatial cells. The calculations ran until the number of superparticles in the simulation reached a clear plateau (typically 10000 - 20000 superparticles after a million time-steps) or achieved a stable oscillation. Due to the nature of the PIC approach, the solutions all display oscillations in the electric field and potential profiles about some time-average value, with periods for the oscillations ranging from 10's of picoseconds to 200 nanoseconds. In the obstructed mode, the analytic result suggests that a change of the cathode voltage by 1 % can change the value of the electric field at a point near the cathode by more than an order of magnitude, so the oscillations in the PIC results aren't surprising. Most of the oscillations occurred in the region just outside the electrode, in the region of steepest potential and electric field gradients; the profiles tended to be fairly stable away from the electrode. To be sure the results had stabilized about a time averaged value, some of the calculations were run out to 8 million time-steps.

Table 3 presents a comparison of the analytic and PIC calculations for an obstructed mode sheath with J_{ext}=2 amp/cm^2, n_{max}=10^{19} m^{-3}, T_e=3200 K, and all other parameters as in Table 2. The range of values presented for the PIC potential and electric field strength correspond to the range over which the values at the cathode oscillated. The range for each value is followed by a time

averaged value given in parenthesis, with the average taken over at least 512 time-steps. To illustrate the sensitivity of the analytic electric field to the exact value of the cathode potential, a range of values are given for the analytic field as well, corresponding to its value calculated at 99.99 % of the cathode potential and the value calculated at 99% of the cathode potential. The value exactly at the cathode potential vanishes by definition.

Table 3. Calculated Sheath Characteristics for an Obstructed Mode Cathode.

	Cathode Fall (volt)		Cathode Field x 10^{-3} (volt/meter)	
	Analysis	PIC	Analysis	PIC
Present Analysis	0.595	0.585 - 0.606 (0.596)	0.35-9.5	−0.88 - 4.86 (2.20)
P&AC Analysis	1.27	1.261 - 1.274 (1.27)	7.40-39.3	65.83 - 66.2 (65.8)

J_{ext}=2 amp/cm^2, n_{max}=10^{19} m^{-3}, T_e=3200 K, and all other parameters as in Table 2.

The PIC model predicts very different time averaged values of the cathode fall and electric field for the two analyses the PIC model is evaluating. This is because each analysis predicts a different ion velocity, emission current density, sheath edge plasma electron current density and thickness, all of which are inputs to the PIC model.

The differences in the values predicted by these two analyses and used as inputs to the PIC model can cause differences of a factor of two in the resulting cathode fall voltage, and a factor of 30 in the cathode electric field. One way to judge which analysis produces the "right" voltage and field values is to examine how well ***both*** the analytic cathode fall voltages and electric fields agree with the PIC results based on the boundary conditions each analysis supplies.

The cathode fall voltage predictions of both the present analysis and that of the P&AC agree extremely well with those of their respective PIC calculations. The cathode electric field predictions, however, are another matter. In the P&AC PIC calculation, the time averaged cathode electric field is a factor of 2 outside the range of values suggested by the 1% perturbation of the analytic results. The results of the PIC calculation based on the present analysis are more encouraging. The time averaged field at the cathode is well within the range of values suggested by the 1% perturbation of the analytic results.

Table 4 presents the results of a comparison of the predictions of the analytic and PIC calculations for a saturated mode cathode sheath with Jext=8 amp/cm^2, n_{max}=8x10^{19} m^{-3}, Te=3200 K, J_E/J_R = 1.1 and all other parameters as in Table 2.

Table 4. Calculated Sheath Characteristics for an Saturated Mode Cathode.

	Cathode Fall (volt)		Cathode Field x 10^{-5} (volt/meter)	
	Analysis	PIC	Analysis	PIC
Present Analysis	0.631	0.627 - 0.637 (0.633)	1.354	1.35 - 1.37 (1.36)
P&AC Analysis	0.885	0.880 - 0.891 (0.885)	1.354	1.95 - 2.36 (2.35)

Jext=8 amp/cm^2, n_{max}=8x10^{19} m^{-3}, Te=3200 K, J_E/J_R = 1.1 and all other parameters as in Table 2.

Again, while the present analysis differs from the P&AC analysis with respect to the cathode fall by about 30%, agreement between both analyses and their respective PIC results are good. The same can not be said of the cathode electric fields. The value calculated by the present analysis falls within the range

of values from the PIC result and matches the time averaged electric field from its PIC calculation to within 1 %, but the value predicted by the P&AC analysis is well outside the range of values calculated by its PIC counterpart and is only 57% of its time averaged value.

PIC Comparisons for the Anode (Non Emitting Electrode) Sheath. A similar comparison to the results of a PIC model was made for the anode sheath, and the results are presented in Table 5.

Table 5. Calculated Sheath Characteristics: Electron Retaining Anode Sheath.

	Anode Fall (volt)		Anode Field x 10^{-4} (volt/meter)	
	Analysis	PIC	Analysis	PIC
Present Analysis	0.223	0.219 - 0.226 (0.222)	6.29	6.08 - 6.42 (6.28)
P&AC Analysis	0.188	0.181 - 0.194 (0.187)	4.22	5.50 - 7.53 (6.40)

T_e= 2750 K. All other parameters as in Table 2 for J_{ext}=2 amp/cm^2.

Once more, while the present analysis differs from the P&AC analysis with respect to the anode fall by about 16%, agreement between both analyses and their PIC results for the anode fall are excellent. Agreement is likewise excellent between the electric field predicted by the present analysis and that calculated by the PIC. The value from the present analysis is within the range of values from the PIC calculation and matches the time averaged value to within 1 %. The electric field calculated from the P&AC analysis, however, falls outside the range of values from the PIC calculation and is only 66% of the time averaged

PIC value. Further, the potential and electric field profiles predicted by the present analysis agree well with the results of the PIC calculation, while those of the P&AC analysis are significantly different from those of the PIC calculation based on that analysis, as can be seen in Figure 12.

Collisionality Having an expression for the electric field in the sheath as a function of the electron potential, the sheath thickness can be calculated as in Langmuir (28:163). If the thickness of the sheath is defined as the distance in which the electron potential falls to 1% of its value at the cathode (or virtual cathode), this results in sheath thickness' ranging from 29 microns for a cathode operating in the saturation regime, to 113 microns for a cathode operating deep in the obstructed regime (using densities and operating conditions typical for cesium plasma thermionic converters). The entire inter-electrode thickness for the example calculation cited in Table 2 is only 254 microns; the collisionless sheath example in the obstructed regime has a thickness almost half the inter-electrode gap!

Redefining the sheath thickness to require the electron potential to fall to 10% of its cathode value cuts the sheath thickness in half, yielding thickness' of approximately 15 microns and 50 microns for the saturation and obstructed regime sheaths, respectively. A quick calculation using the data in Table 2 yields electron-atom mean free paths of 16.7 microns, and ion atom mean free paths of 5.6 microns, so that the sheaths calculated using the collisionless treatment are

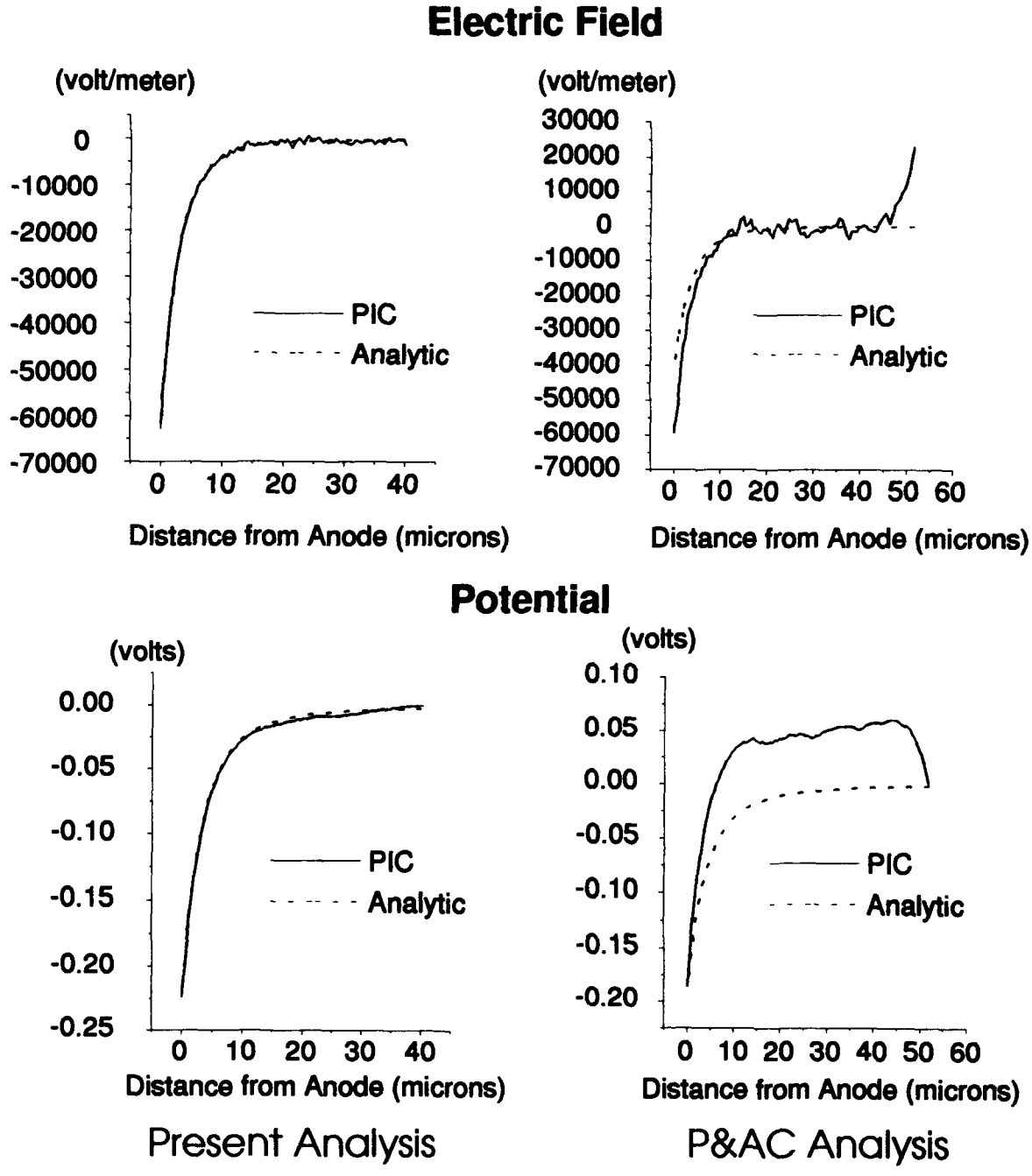

Figure 12. Comparison of Analytic Profiles to those from PIC Calculation.

many ion-atom mean free paths thick, and one to three electron-atom mean free paths even using the most restrictive estimate of the sheath thickness. These results suggest that the collisionless treatment of the sheaths -- used so frequently in modeling thermionic converters -- is not appropriate for these devices, especially in the obstructed regime.

Conclusion.

In this chapter, a collisionless sheath model was developed that is applicable across the entire range of sheath potentials, including potentials that are small with respect to the plasma electron temperatures. The model is particularly applicable for low pressure thermionic converters and diodes. After validation against the results of PIC calculations, the model was used to examine the consistency of the collisionless sheath assumption so often used in the modeling of high-pressure thermionic converters. Under these conditions, the calculated sheath dimensions were found to be inconsistent with a collisionless treatment. Previous work had suggested that sheath structures could extend to an ion-atom mean free path in the obstructed mode, but details of the analysis leading to that suggestion were not given (36:33). The present analysis shows analytically that the sheaths calculated using a collisional model can extend not one but many mean-free-paths into the interelectrode space, and extends the regime of concern across both the saturated and obstructed regimes.

The need for a collisional treatment of the sheaths makes a PIC treatment of a thermionic converter tempting, but the difficulties associated with the PIC approach for the bulk of the plasma in the inter-electrode gap seemed insurmountable. These considerations indicate that a hybrid approach, using PIC techniques in the sheaths, and fluid techniques in the bulk of the plasma, might be necessary. In the next chapter the details of the PIC and Fluid techniques used to construct such a model are described, as well as the method used to couple PIC and Fluid regions together.

III. A Hybrid PIC-Fluid Model

Introduction.

In the last chapter it was shown that a collisional approach is necessary to adequately model the sheaths of a high-pressure, ignited mode thermionic converter. In this chapter a collisional model is developed using a regional, hybrid technique. A Particle in Cell (PIC) approach is used for the anode and cathode sheaths and a fluid approach is used for the bulk of the plasma between the sheaths. The PIC approach is not used in the bulk because of the difficulties associated with treating ionization and recombination. For sufficiently thin sheaths, the role of ionization and recombination can be ignored as in past models, based on the low electron densities, the energy threshold for excitation and the narrow extent of the sheaths. When ionization and recombination can be ignored, the PIC method can provide an analysis that retains the collisionality (via elastic electron-atom and ion-atom charge exchange collisions) and allows the potential profile to form in a self consistent manner.

The fluid approach is not used in the sheaths, on the other hand, because the ion and electron velocity distributions are not well characterized there, having functional forms that vary substantially across the sheath regions. A fluid approach *is* attractive in the bulk of the inter-electrode space, however,

because the complicated ionization and recombination kinetics can be approximated using rate coefficients based on the assumed form of the distribution functions present in the bulk.

In this chapter, the details of the regional, hybrid model and the computer program implementing the model are presented. To begin, the PIC and fluid models used in the sheath and bulk regions (or sectors, as they are called in this implementation) are described, followed by a description of the interface algorithms linking the sectors together. Then, an overview of the computer program and the user interface is presented. The chapter concludes with a presentation of the results of validation calculations performed to ensure the implementation was functioning correctly as a whole.

The PIC Module.

The PIC approach used in this work is an adaptation of that developed by Birdsall et al. (4) and implemented in the code PDP1 (52). The PDP1 algorithms include a Monte Carlo collision capability for modeling ion-atom elastic and charge exchange collisions, electron-atom elastic scatter, excitation and single step ionization collisions assuming uniform neutral density and temperature. In the narrow sheath regions, the dominant collisions are anticipated to be ion-atom charge exchange and elastic electron-atom scattering (3:59-60). Ionization collisions are ignored because of the high threshold for excitation of the cesium

atoms to the first excited state, the relatively small cross sections at the typical electron energies found in the sheaths, and the relatively low density of excited state atoms with lower excitation/ionization thresholds. Recombination collisions are ignored in the sheaths because of the relatively low electron and ion densities there. The PIC model implements electron-atom excitation collisions, although this capability was not used in any of our calculations. The excitation energy threshold for the first cesium excited state is 1.4 eV, and, with sheath heights of about one volt, very few electrons have enough energy to participate in excitation collisions. Furthermore, the excitation cross section itself does not become comparable to the elastic scattering cross section until an electron energy of about 3 eV, and approaches the magnitude of the elastic scattering cross section at an energy of 10 eV (42:667-668); the few electrons with enough energy to cause excitations are at least as likely to scatter elastically, even at the higher energies.

Because the PIC technique used is an adaptation of that implemented in the PDP1 code and discussed thoroughly by Birdsall, the details of the PIC technique and algorithms will only be discussed to the extent that they differ in substantive ways from these two references. The differences of this approach from previous work can be broken into two major groupings: 1) those necessary or convenient for a multi-sector hybrid treatment, and 2) corrections to the PDP1 code.

There are several changes made to the PDP1 approach to enhance its applicability to the modeling of thermionic converters. The most fundamental is the use of multiple sectors, each with its own grid spacing. This modular approach is implemented by treating each sector as an independent bounded one dimensional problem, with interfaces in the place of walls. Poisson's equation is solved separately in each sector, using the value of the total charge density to the left of the left interface and the potential at the right interface as boundary conditions. This approach allows the grid spacing in each sector to be independent of what is used in other sectors, so that a fine mesh structure can be used in regions where the fields or particle distributions are changing rapidly, and a coarser structure where the fields are changing more slowly.

Implementation of this approach requires a three step PIC execution sequence. When a PIC sector is called to execute, it updates all particle velocities and positions in each of its species objects. It then tests to see which particles have moved outside of its boundaries, and transfers those particles to the interfaces. All sectors execute this portion of the sequence before the calculation proceeds, in order to load the interfaces with the particles that have crossed between sectors. Once this is done, the particles in the interfaces can be traded with the neighboring sectors, and new particles injected into the sectors bounded by the actual walls. Next, the probability of collision is calculated for each particle in the simulation, and the results of any collisions determined using

Monte Carlo techniques. Collisions must be calculated after the injection step to insure the collisions of particles that crossed boundaries are properly accounted for. Finally, after all particles have been injected and any new particles from ionizing events have been created, the new electric fields are calculated.

A second modification to the traditional PIC approach is the use of variable weights on the injection particles. In our treatment, each species class contains a linked list of particle class objects, each of which tracks its own velocity, energy, position and weight. Through both the input file and the user interface, the user selects injection rates for the types of particles in the simulation: ions, electrons, and thermionic electrons (the weights of electrons that the user specified as 'thermionic' are adjusted when an accelerating electric field exists at the wall, to increase the emission current density consiste. with the Schottky effect). The injection rate, together with the injection flux and the time-step determine the weight of each new particle. When the user changes the injection rate, the weight of the particles being created is altered, but all other particles already existing in the simulation retain their weights. Thus there can be particles of the same species in the simulation having a variety of weights. To conserve particles when a particle has an ionizing collision, the new ion and electron are given the same weight as the colliding particle.

The use of variable particle weighting has a number of advantages. It allows the user to monitor the number of particles in the simulation, and adjust the injection rate up or down during the calculation to obtain a reasonable

number for computational efficiency. It also allows the weights of the ions to be adjusted independently from that of the electrons. This is important, because the ions are much heavier and move more slowly than the electrons, thus they tend to build up in number more quickly. A variable weighting scheme also allows for the modeling of systems in which there are large differences between the injection current densities (a small electron beam being injected into a neutral plasma, for example, to study the beam-plasma instability), while maintaining statistically significant numbers of particles for each injection stream. With fixed particle weighting, the small current density (which may actually be driving the phenomena being studied) has a comparably small injection rate, so that its effects are statistically hard to determine. With a variable weight scheme, the injection rate of the small current density can be adjusted so that there are a large number of particles injected, each carrying a relatively small weight, and resulting in greatly improved statistics. This approach also allows for adjustments to the weights of injected particles to account for variations in the emission current density without adjusting the injection rate, thus enabling closer control over the number of particles in the simulation and better fidelity to the phenomena being modeled. The closer control over the number of particles in the simulation is a direct consequence of an absolute control over the injection rate. The better fidelity to the phenomena being modeled arises from the fact that the weight of <u>every</u> particle injected reflects an adjustment for the

phenomena of interest. If fixed particle weighting were used for a phenomenon that resulted in a fractional increase in the injection rate, additional particle emission would have to be accumulated until a discrete superparticle could be emitted, thus staggering the effect of the phenomenon over the number of time-steps required to generate a single additional superparticle. With variable particle weighting, the weight of each particle, not the injection rate, is adjusted by the fractional increase, so the effect of the phenomenon has as fine a time resolution as the injection rate itself.

For our application, the phenomenon of interest is the Schottky effect. This effect is included by increasing the weight of the injected electrons when there is an accelerating electric field at the surface of the cathode, to give the appropriate value for the overall injection current density. Other effects that could be modeled in a similar fashion include emitter temperature (particularly for thermionic electrons, using a time dependent or user controlled emitter temperature), secondary emission due to electron/ion bombardment, and particle reflux. These are not implemented in the computer code at this time.

A final feature included in this application to enhance its application in a hybrid code is the ability to ramp the injection current densities up and down in magnitude. Ramping is accomplished by adjusting the weight of the particles injected towards a target weight which gives the target current density. This allows one to start a calculation with boundary conditions and internal conditions matching that of a quiescent plasma at a given temperature and

density, and then ramp down the "random" current densities being injected at the boundary while slowly ramping up the target injection current densities and external circuit current. This allows for a quieter start and eliminates initial changes to the boundary conditions which may otherwise occur too quickly for the plasma to respond, leading to a large "ringing" at the plasma frequency as the simulation first overcompensates then attempts to correct for the start-up noise.

In addition to the changes made to enhance the application of the PIC technique in a hybrid code, there were a number of errors in the PDP1 model itself that were identified and corrected in the implementation of the PIC algorithms. The developers of PDP1 were informed of a number of these corrections and responded by telling us that the collisional model in the code had been updated. The specifics of the corrected model were not provided.

A number of the errors discovered and corrected were quite serious. The transform used in the computer code and reported in the papers documenting the code (37:8,1:10) to convert from the particle coordinate frame back to the simulation coordinate frame in an elastic scattering event is in error. Figure 4 in Reference 37 gives the transform illustrated in Figure 13, in which the primed quantities are post-scatter, the hatted quantities are the normalized velocities, the angle ϕ is chosen randomly between 0 and 2π, and the angle χ is determined by an empirical correlation based on the energy of the colliding electron (37:9).

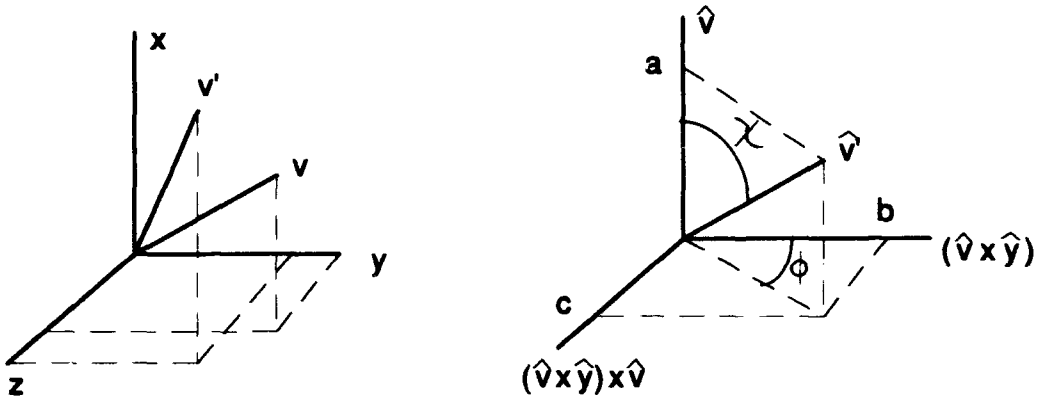

$$v_x' = |v'| \left(\hat{v}_x \cos(\chi) - \hat{v}_z \sin(\chi)\cos(\phi) - \hat{v}_x \hat{v}_y \sin(\chi)\sin(\phi) \right) \qquad a = \cos(\chi)$$

$$v_y' = |v'| \left(\hat{v}_y \cos(\chi) + \hat{v}_x{}^2 \hat{v}_z{}^2 \sin(\chi)\sin(\phi) \right) \qquad b = \sin(\chi)\cos(\phi)$$

$$v_z' = |v'| \left(\hat{v}_z \cos(\chi) + \hat{v}_z \sin(\chi)\cos(\phi) - \hat{v}_y \hat{v}_z \sin(\chi)\sin(\phi) \right) \qquad c = \sin(\chi)\sin(\phi)$$

Figure 13. PDP1 Velocity Space Transformation (37:8).

An examination of the code, together with an analysis of the transform, shows the second term of the equation for v_y' to be a typographical error. The v_x^2 and v_z^2 terms should be added, not multiplied, before being multiplied by the sine terms. However, even with this correction in the code, the transform in both the code and the documentation is incorrect, as can be seen by evaluating for the case of $\chi=\phi=\pi/2$. This results in a value for $\hat{v}'^2 = \left(1 - \hat{v}_y^2\right)$ which is only equal to 1 (as it should always be) when v_y vanishes. The correct transform (derived in Appendix D) corrects for the multiplication of the v_x^2 and v_z^2

discussed previously, and then divides all terms in the equations for the scattered velocity (other than the first term involving cos(χ)) by $\left(\hat{v}_x^2+\hat{v}_z^2\right)^{1/2}$, resulting in:

$$
\begin{aligned}
v_x' &= |v|\left(\hat{v}_x\cos(\chi)-\left(\hat{v}_z\sin(\chi)\cos(\phi)+\hat{v}_x\hat{v}_y\sin(\chi)\sin(\phi)\right)\sqrt{\hat{v}_x^2+\hat{v}_z^2}^{-1}\right)\\
v_y' &= |v|\left(\hat{v}_y\cos(\chi)+\sqrt{\hat{v}_x^2+\hat{v}_z^2}\sin(\chi)\sin(\phi)\right) \qquad (51)\\
v_z' &= |v|\left(\hat{v}_z\cos(\chi)+\left(\hat{v}_z\sin(\chi)\cos(\phi)-\hat{v}_y\hat{v}_z\sin(\chi)\sin(\phi)\right)\sqrt{\hat{v}_x^2+\hat{v}_z^2}^{-1}\right)
\end{aligned}
$$

Using these equations, the sum of the squares of the direction cosines always equals 1, as it should. The error introduced by the incorrect transform results in an energy loss due to "elastic" collisions, as the magnitude of the scattered electron velocity is on average less than that of the incident electron.

A second error in the collision module has to do with the calculation of the values for sin(ϕ). As mentioned previously, ϕ varies from 0 to 2π, and is chosen randomly. Cos(ϕ) is then calculated correctly, but then sin(ϕ) is calculated as $\sin(\phi)=\sqrt{1-\cos^2(\phi)}$, and is thus always positive, when it should also have negative values. The effects of this error are not immediately obvious, but, on close examination, bias the perpendicular component of the scattered particles toward the positive y-axis, resulting in a net flux in the positive y direction when the scatter should not be correlated with the y direction. Because the present analysis uses only the x and perpendicular components of the

velocity vector and ignores magnetic fields, this bias of the perpendicular component of the velocity towards the y direction is inconsequential. It should be of concern, however, for codes which include the effects of applied magnetic fields.

Another, more serious error is in the modeling of charge exchange of ions with neutrals. In PDP1, the probability of collision is determined by the energy of the ion, independent of the energy of the neutral with which it collides. To see the effect of this error, consider the case of a constant collision cross section. The probability of a collision during a single time-step is a function of the distance traveled in that time-step, which in turn is a function of the ion velocity. The faster the ion, the higher the probability of a collision. Thus, the fast ions are collided preferentially over the slow ions. The new ion, however, is selected with a velocity consistent with the neutral velocity distribution function. If the ions and neutrals were initially at the same temperature, then, the fast ions would be exchanged for neutrals with, on average, lower velocities, leading to a cooling of the ion distribution. The correction for this is to pick a neutral at random for each ion and calculate the probability of collision based on their relative velocity. In this way, even ions that are motionless have a chance of exchanging their charge with a 'hot' neutral, and the temperature of the ions is maintained. This scheme is implemented in the hybrid code developed in this

work by choosing an initial velocity for the neutral by the same methods used in loading a thermal distribution into the inter-electrode space at startup.

Finally, PDP1 contains an error in the particle injection scheme. In test calculations, the error results in a small changes in the calculated values (less than 0.1% for the value of the potential across an ideal diode), and has to do with the adjustment of the injection particles to match the "leap-frog" scheme used to advance the velocity and position of particles in the simulation. For completeness, the error and correction are discussed in Appendix B.

The Fluid Module.

The fluid equations used in this work represent the first three moments of the Boltzmann equation, derived from the equations of Holt and Haskell (17:156-165) with the collisional treatment following that of Golant et al.(13:168,174), assuming uniform neutral density and temperature. The derivation of the equations is treated nicely in these two references and will not be repeated here, but some discussion is in order as to the final form of the equations. Typically, past models of the plasma in thermionic converters have dropped the inertia terms from the momentum equation, and assumed charge neutrality so that only the density of the electrons had to be calculated. The ion temperature is usually assumed to be equal to that of the cesium atoms. In this manner, the fluid equations are greatly simplified, and reduced from six coupled equations to as

few as three (the continuity equation, a transport equation, and an electron energy equati Because this analysis was intended to produce a physics based code, it was decided to retain the generality of the fluid equations, including the inertia terms in the momentum equations, and to track the density and temperature of the electron and ion distributions separately.

Two additional decisions had to be made before constructing the fluid module. The first was how to characterize the velocity distributions in the bulk of the plasma. As mentioned pr the electrons and ions in the bulk of an ignited mode converter plasma are frequ ly characterized as having velocity distributions that are almost Maxwellian. The ion and electron species are generally considered to have different temperatures and drift velocities, and those values are generally said to vary spatially across the inter-electrode space. With this understanding, the decision was made to characterize the electrons and ions using distinct, single-group Maxwellian velocity distributions (one for each species), with densities, temperatures and drift velocities that vary spatially. The choice of a single-group description determined the form of the fluid equations and has far reaching effects on the final results of this effort. The limitations to the overall model introduced by this approach, as well as the potential of alternative approaches, will be discussed in Chapter IV.

The second decision to be made was how to cast the fluid equations: should they be cast in terms of particle, momentum, and energy fluxes, or in terms of density, temperature and drift velocity? For any given velocity

distribution function, the representations are equivalent -- but there are pros and cons to both choices when it comes to interfacing a fluid sector to a PIC sector.

The energy and momentum fluxes are not used or calculated in the PIC formalism, and the particle flux is only used to specify the injection rate of particles into the simulation and to update the surface charge density at a wall. Having said that, the fluxes at an interface can be calculated directly from the particles crossing the interface, or by taking a weighted average over all the particles in the vicinity of an interface. Either approach is no more complicated than that used to calculate the particle density. In addition, casting the fluid equations in terms of the fluxes makes conservation of particle, momentum and energy flux across an interface more apparent.

Density is calculated explicitly in both the PIC and fluid techniques, and is used to calculate the charge density and electric fields. It is therefore a natural quantity to use as one of the fundamental variables in the fluid formalism. On the other hand, the PIC formalism doesn't assume a functional form for the velocity distribution of the particles in the simulation -- the particles can develop any velocity distribution consistent with the physics being modeled. Thus, temperature and drift velocity are not natural quantities used in updating particle positions and velocities in a PIC calculation, and do not even have an exact meaning. The temperature and drift velocity are only used in the PIC

formalism as parameters to the assumed form of the velocity distribution function used to select the velocities of particles injected at the walls.

If fluxes were used as the fundamental quantities in the fluid model, the fluxes would have to be translated into an injection stream of particles for the PIC sector. With the assumption of Maxwellian velocity distribution functions in the plasma, a Maxwellian, parameterized by a density, drift velocity and temperature, is used to determine the velocities of the particles injected into the PIC sector at a fluid interface. Thus, even if the fluid equations were cast in terms of fluxes, at the interfaces those fluxes would have to be translated back into an equivalent set of density, temperature and drift velocity parameters to generate representative velocities for the PIC injection particles. For this reason and the other considerations presented above, the density, temperature and drift velocity were chosen to be the fundamental variables in which to cast the fluid equations. This choice will be revisited in Chapter IV.

The final form of the equations can be expressed generically for either electron or ion species as:

$$\frac{\partial n}{\partial t} = S_{COLL} - n\frac{\partial v}{\partial x} - v\frac{\partial n}{\partial x} \tag{52}$$

$$\frac{\partial v}{\partial t} = \frac{qE}{m} - v\frac{\partial v}{\partial x} - \frac{e}{m}\frac{\partial T}{\partial x} - \frac{eT}{nm}\frac{\partial n}{\partial x} + \sum_{\alpha} \upsilon_{\alpha}^{scatter}\left(v_{\alpha} - v\right)\frac{m_{\alpha}}{m + m_{\alpha}} \tag{53}$$

$$\frac{\partial T}{\partial t} = \frac{2}{3}\left[\frac{M_{COLL}}{ne} - \sum_{\alpha} \upsilon_{\alpha}^{scatter}\frac{v}{e}\left(v_{\alpha} - v\right)\frac{mm_{\alpha}}{m + m_{\alpha}} - \right.$$

$$\frac{S_{COLL}}{n}\left(\frac{mv^2}{2e}+\frac{3}{2}T\right)-\frac{3}{2}v\frac{\partial T}{\partial x}-T\frac{\partial v}{\partial x}\Bigg] \qquad (54)$$

for the continuity, momentum and energy equations, respectively. All units are SI in these equations, except for T, the temperature in electron volts; n is the density, S_{COLL} is the net ionization rate, v is the drift velocity, q is the species' charge, E is the electric field, m is the species' mass, υ is the collision frequency, e is the elementary charge, and M_{COLL} is the rate of change of energy due to collisions. The collision frequency in the summation terms involves scattering events only -- ionization and recombination are handled separately through the ionization rate term. Electron scattering events accounted for are electron-ion and elastic electron-atom collisions. Ion scattering events accounted for are charge exchange and electron-ion collisions. These represent the dominant elastic and inelastic (other than ionization/recombination) processes in a cesium plasma (3:59-60).

The collision frequencies for electron-atom and ion-atom collisions are calculated using constant cross sections, because the values of the cross sections vary only slightly over the energies of interest in a typical thermionic converter(3:60-61). The cross section values are set by the user through the input file. The ionization rate is calculated using the correlations from Norcross and Stone (42:669). The rate of change of energy due to collisions is calculated according to the following expressions:

$$M_{COLL} = M_{COLL}^{inelastic} + M_{COLL}^{elastic} \tag{55}$$

$$M_{COLL}^{inelastic} = \begin{cases} -S_{COLL}E_i - n_e R & (electrons) \\ -\frac{3}{4} n_i \upsilon_{chx} e(T_i - T_a) - \frac{1}{4} n_i \upsilon_{chx} m_i v_i^2 & (ions) \end{cases} \tag{56}$$

$$M_{COLL}^{elastic} = -n\sum_{\alpha} \frac{2m m_\alpha}{(m+m_\alpha)^2} \upsilon_\alpha^{elas} \left[\frac{3}{2} e(T - T_a) + \frac{1}{2}\left(mv^2 - m_\alpha v_\alpha^2 + (m_\alpha - m) v v_\alpha \right) \right] \tag{57}$$

where E_i is the energy required (in eV) to ionize a neutral atom, R is the radiative energy loss rate, υ_{chx} is the charge exchange frequency, and all other symbols are as defined for the continuity, momentum and energy equations (13:174-175).

There are two major contributors to the inelastic energy loss rate for electrons. The first, ionization losses, are the losses that arise from the ionization of the cesium atoms. The second, radiative energy losses, arise from excitations of the cesium atoms that later radiatively decay. Some of the radiation emitted -- particularly the resonance radiation from excited electrons decaying to the ground state -- is trapped and has no net effect on the energy loss rate. Non-resonance radiation escapes the plasma and serves as a cooling mechanism. Baksht provides an expression with which to evaluate the loss rate, but indicates the radiation term is small with respect to the ionization energy loss term (3:147). For this reason, the radiative energy loss rate is neglected in our implementation of these equations in the code. Because it *is* an energy loss term, however, it could have a significant effect in the precarious energy balance of the obstructed regime, so its effect should be checked for calculations in that regime.

The ion inelastic energy loss terms represent the energy losses that arise from charge exchange with the neutral cesium atoms, as charge exchange is the dominant scattering process for cesium ion-atom collisions (3:60). The first term represents the exchange of thermal energy and the second the exchange of directed energy with the neutral species.

The elastic energy loss terms are the losses due to elastic, two-body collisions; the summation in Equation (57) is over electron-ion and electron-atom collisions for electrons, and ion-electron collisions for ions. The electron-ion collision frequency in Hz is calculated as (17:271):

$$\upsilon_{ei} = \frac{2.1x10^{-12} n \ln \Lambda}{T^{3/2}} \tag{58}$$

where T is the electron temperature in eV, n is the electron density in m^{-3}, and $\ln\Lambda$ is given by:

$$\ln \Lambda = 30.37 + \frac{3}{2}\ln(T) - \frac{1}{2}\ln(n) \tag{59}$$

The fluid equations are implemented using finite difference techniques on a numerical grid. The grid has major grid-points at the cell centers and minor grid-points at the cell boundaries; an identical grid is used in the PIC implementation. The density and temperature are calculated on the major grid-points, and the drift velocity on the minor grid-points. The value of the drift velocity used in the calculation of the density and temperature at a major grid point is taken as the average of the value at the adjacent minor grid-points.

Similarly, the values of the density and temperature used in the calculation of the drift velocity on the minor grid-points are the average of the values at the adjacent major grid-points.

In our implementation of the fluid equations, the choice had to be made whether to use an *explicit* or an *implicit* method to calculate new macroscopic values in terms of the old. In an explicit method, a forward difference technique is used to approximate the first derivatives in time, so that new values at each point are calculated in terms of the old values and their first spatial derivatives. This is an intuitive approach and the simplest to implement. The drawback to using explicit techniques is that they are frequently limited with respect to the maximum permissible time-step. The classic example is that of the parabolic heat equation, in which the time-step must be less than the square of the ratio of the normalized cell size to the diffusion constant(7:624). At larger time-steps, errors grow without bound and the calculation fails.

To avoid the time-step limitation, an alternative technique is frequently employed, classified as an implicit method. In this method, a backward time difference technique is used, so that the new values at each point are calculated based on their old values and the new values at the adjacent grid points. The disadvantage of this technique is that it involves the linearization of the differential equations and the inversion of a matrix in order to calculate the new values. The equations used in this work are so complicated that linearization,

such as that used by Kurata in the modeling of semiconductor devices(25:28-54), would prove a formidable task unless substantial simplifications of the equations were performed.

Because the PIC formalism already limited the time-steps to the order of a picosecond, the decision was made to attempt an explicit treatment. At picosecond time-steps and with grid spacings of one micron, the calculations proved to have a stability problem and to be very sensitive to noise. As long as conditions were far from steady state, the calculations proceeded without any evidence of instability. As steady-state was approached, however, instabilities developed in the drift velocity calculations, leading to the development of negative temperatures and densities.

Because the stability problem arose as steady state was approached, an expression for the steady-state drift velocity was developed. When substituted into the continuity equation, the continuity equation was found to be parabolic, similar in form to the heat equation. If the stability constraints are analogous, a maximum time-step of 2×10^{-13} seconds -- one fifth of the time-step we were using -- is predicted for a stable calculation with a one micron grid spacing. A similar analysis was performed using an expression for the steady state density, and the drift velocity expression was also found to be parabolic. The time-step limitation for the velocity expression could be as small as 2×10^{-15} seconds, depending on the value of the first spatial derivative of the velocity as steady-state is approached.

To try to dampen noise and enhance the accuracy in the first derivatives, five point central difference schemes were introduced in place of the three point schemes used previously. For first derivatives of values on the same grid as the derivative being calculated, a centered five point scheme from Burden and Faires was implemented(7:150). This technique assumed that all five values to be used were equally spaced, with the first derivative being calculated at the central point. First derivatives of major grid-point quantities (density and temperature) were also needed at the minor grid-points, mid-way between major grid-points. Using the same analysis presented in Burden and Faires in the development of their five point scheme, the following relation for these 'trans-grid' derivatives was developed:

$$\frac{\partial f}{\partial x} \approx \frac{-1}{24h}\left(f\left(x+\frac{3h}{2}\right)-27f\left(x+\frac{h}{2}\right)+27f\left(x-\frac{h}{2}\right)-f\left(x-\frac{3h}{2}\right)\right) \qquad (60)$$

where x is the location at which the derivative is desired, midway between two of the grid-points at which the value of f is known, and h is the distance between the grid-points at which the value of f is known. At the boundaries it is not possible to use these formulae because enough values are not known. The original three point central difference schemes were used there.

With these modifications, acceptable time-step limitations were obtained; fluid calculations with time-steps of 0.025 picoseconds were stable with grid spacings down to one micron. With a fluid sector time-step of 0.025 picoseconds, the fluid sector can be stepped forward in time 40 time-steps for

every picosecond time-step in the PIC sectors without seriously degrading the run-times of the program. The fluid calculations execute so quickly that the PIC sectors remain the limiting performance drain on the overall computation.

The process of calculating many time-steps in the fluid sector for one time-step in the PIC sector is referred to as "subcycling", and it adds somewhat to the complexity of the calculation. In particular, the conditions at the fluid sector boundary have to be accumulated over the cycle and then averaged for passing to the PIC sectors. Further, the electric field must be updated in the fluid sector each subcycle time-step to balance the changes in density and temperature gradients and insure the correct updating of the drift velocity. Updating the electric field includes updating the charge density at the left hand boundary to account for the current in the external circuit as well as for particle flux across the boundary. Finally, the boundary conditions provided by the PIC sectors are only known at the beginning of the major time-step, but the fluid sector requires boundary condition updates at each subcycle time-step. To approximate the changes at the boundary, the differences between the new boundary values at the beginning of the time-step and the values at the beginning of the last time-step are calculated and then divided by the number of fluid sector subcycles per PIC time-step. The boundary values are then incremented using these differences each subcycle time-step as an approximation to the change in the actual values. At the end of the PIC time-

step, the boundary conditions are set to the actual values resulting from the calculations in the adjacent sectors.

The flow of the calculation in the fluid sector is actually quite simple. All the first derivatives are calculated using the old values of the density, temperature and velocity. The new values are then calculated using the old values, the derivatives and the boundary values. The boundary values are then updated, the old values of the density, temperature and velocity replaced with the new values, and the electric field recalculated. This sequence is repeated until sufficient subcycles have been performed to complete a full PIC time-step.

Interfacing the Sectors.

Between every two sectors there are two interfaces, the left interface of the sector to the right and the right interface of the sector to the left. This arrangement is illustrated in Figure 14. At the time a sector is initialized, it passes information about itself, including type of module (PIC or Fluid) to its left and right interfaces. Based on that information, the interfaces create the objects they will need to store boundary information from their sector.

The individual responsibilities of each interface are determined by its type. For example, the left interface of the first sector in Figure 14 is a wall interface. If sector 1 is a PIC sector, then the left interface is a LEFT, WALL-PIC

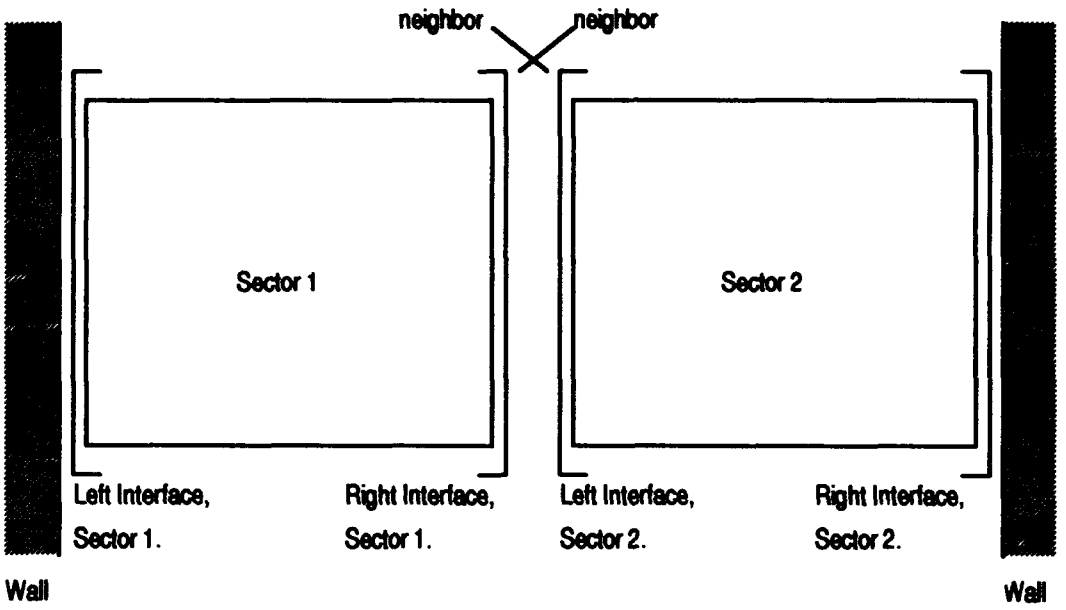

Figure 14. Relationship of Sectors and Interfaces in the Hybrid Model.

interface. That it is a WALL-PIC interface means it has no neighbor, and is responsible for creating injection particles to model the injection flux from the wall. That it is a LEFT boundary means it only injects the species that are supposed to be injected from the left wall, and is also responsible for accumulating a surface charge density from the injection flux and from the flux of particles leaving the sector through the left interface.

If Sector 1 were a fluid sector, the left interface would be a WALL- FLUID interface and would not have the responsibilities associated with particle injection. Instead, it would have to supply boundary condition values for the fluid equations. The right interface of Sector 2 is treated exactly the same as the left interface of Sector 1 except, if Sector 2 is a PIC sector, the right interface is

responsible for creating and injecting the particles for species having a flux from the right wall.

The interfaces between the two sectors are either PIC-FLUID, PIC-PIC, or FLUID-FLUID interfaces, depending rather obviously on the nature of the sectors being joined. If an interface is a PIC-FLUID interface owned by a PIC sector, it is responsible for creating and injecting particles into its sector based on information it receives from its fluid neighbor. Similarly, if the interface is owned by a fluid sector, the interface is responsible for providing boundary condition data and rates of change in that data to its fluid sector.

The role of a PIC-PIC interface is to receive particles from its neighboring interface and pass them unperturbed to its owning sector. Similarly, a FLUID-FLUID interface receives boundary conditions and rates of change in the boundary conditions and passes them to its owning sector.

A number of considerations must be made when setting up the interfaces between the sectors, chief of which is the nature of the sectors being interfaced. In the pages that follow, each of the interfaces will be described and the considerations and difficulties associated with each discussed. In the discussion frequent reference will be made to densities, temperatures and drift velocities, without specifying any species designation. It should be understood that both electron and ion species are meant and that they are tracked separately in both PIC and fluid modules.

The PIC-PIC Interface. Conceptually, the simplest type of interface is PIC-PIC. Essentially, its job is to take the particles that cross the interface leaving the PIC sector and transfer them directly into the neighboring sector so that their movement in space continues as if the interface didn't exist. This requirement leads to a need to transfer particles to the sector interfaces, then between neighboring interfaces, then from interfaces to sectors again. To implement this transfer capability and simplify the process, a species class was created that contains all the information generic to a particular injection stream of particles and which serves as a mount point for a linked list of particle objects. Each sector creates an array of species objects and the particles it requires at startup. Each interface creates a set of species identical to those in the sector it bounds, but without any particles.

A schematic of the particle update and transfer sequence is given in Figure 15. At the execution of a time-step, the velocity of each particle in each species in a sector is updated in time, and the particle moved through space based on its new velocity. After the particles in a sector have been moved, each particle is polled to see whether its new position is outside the bounds of the sector. If the position is negative, the particle is given to the left interface of the sector, where it is added to the left interface's list of 'out-bound' particles of that species. The particle's position, velocity and weight are transferred as part of the particle's information about itself, stored in its class structure. The particle's

```
For I=1 to nsectors
        Update Velocity
        Move Particles
        If position <=0
                Give to Left Interface
                Update Surface Charge
        Elseif position >= Sector Width
                Give to Right Interface
        Endif
Next I

For I=1 to nsectors
        Get Particles from Neighbors
        Inject Particles
        If SIDE==LEFT Update Surface Charge
        Collide Particles
Next I

For I=nsectors to 1
        Get Right Hand Side Potential
        Calculate Potential
        Calculate Electric Field
        Update Left Hand Side Potential
Next I
```

Figure 15. Time-step Sequence for PIC-PIC Calculation.

charge is added to the left interface "surface" charge density for use in the calculation of the electric field. In a similar fashion, if a particle's position is beyond the right sector boundary, the particle is transferred to the right interface.

After all sectors have executed and stored their out-bound particles in their interfaces, each sector is called to get input from its neighboring sectors. Each sector interface polls its neighbor to determine if there are any particles to be injected. If there are, the interface takes the particles from the neighboring

interface and rescales the position and velocity of the inbound particles. These particles are stored in the 'in-bound' set of species in the interface. Once all particles have been transferred, each interface is called to inject its 'in-bound' particles into its sector. An interface does this by simply giving the particles it received from its neighbor to the corresponding species of its sector. The sector species then simply add the injected particles to their lists of particles.

Each sector then approximates the effect of collisions on the particle distributions using Monte Carlo techniques. Collisions are allowed to take place based on the total distance traveled in the time-step, including the distance traveled in the previous sector, consistent with the path-length that would have been used if the interface did not exist.

Finally, the rightmost sector is called to calculate its potential and electric fields, starting with a potential arbitrarily set to zero at the right hand boundary. The value of the potential calculated at the left hand boundary is passed to the right hand interface of the next sector to the left to serve as a consistent boundary condition across the interface. The process continues until all sectors have calculated their potential and electric fields.

The technique outlined above allows particles to move across an interface almost as if the interface were not there in the first place. There is, however, a small discontinuity introduced by the PIC-PIC interfaces in a multi-sector PIC calculation, that arises from the nature of the spatial mesh and the calculation of average values at the boundaries. The discontinuity is particularly apparent if

the interface is located in a region where large gradients in the electron and ion densities occur. Under these conditions, the value of the density calculated at the interface will be discontinuous at the interface. This is a subtle effect, and though the discontinuity in the calculated value of the density at the interface can be unsettling, there is no significant effect on electric field calculated there or on the motion of the particles across the interface. A complete discussion of the discontinuity, including its effect on the electric field, is presented in Appendix A.

The FLUID-FLUID Interface. The second interface to be considered, and the simplest to implement, is the FLUID-FLUID interface -- an interface between two fluid sectors. This interface is not necessary for the implementation of a PIC-Fluid hybrid code (it was included in the development of the code primarily for diagnostic purposes), but a discussion of this simple interface lays a groundwork that is helpful in the more complicated PIC-FLUID interface.

As mentioned in the description of the fluid module, our implementation of the fluid equations employs a single-group approximation: the electrons and ions can have different densities and velocity distributions, and the distributions can vary with position and time -- but at any location and time, each species is assumed to be represented by a single temperature and density characterized by a single, possibly drifting, Maxwellian distribution. This level of definition is

provided in the fluid description to enable the interface to the PIC sector, to be discussed shortly.

Numerically, the inter-electrode space is divided into spatial cells using the same numerical grid structure as in the PIC module. The density for each species is calculated at the cell centers on the same set of grid-points (the major-grid points) as in the PIC formalism. This allows for the use of the same subroutines for calculating the potential and electric fields as used by the PIC calculations. The temperature is also calculated on the major grid-points as it represents a cell centered value. The drift velocity, however, is calculated on the minor grid-points as it is representative of the particle flux between cells. Central finite difference techniques are used for the first spatial derivatives, and a simple forward difference technique is used to evolve the density (n), drift velocity (v) and temperature (T) of each species forward in time. A schematic for the advancement through a single time-step as shown in Figure 16, in which the solid lines drawn from quantities at time t0 to quantities at t1 indicate a dependence of the new values on the old values.

For consistency, one would like for the values of density, drift velocity and temperature calculated using such a multi-sector approach with FLUID-FLUID interfaces to exactly match those calculated using a single sector over the same volume and conditions. To accomplish this goal, the interface algorithm is designed to emulate the information transfer and evolution that would occur in the middle of a single fluid sector. When a sector is executed, the new values of

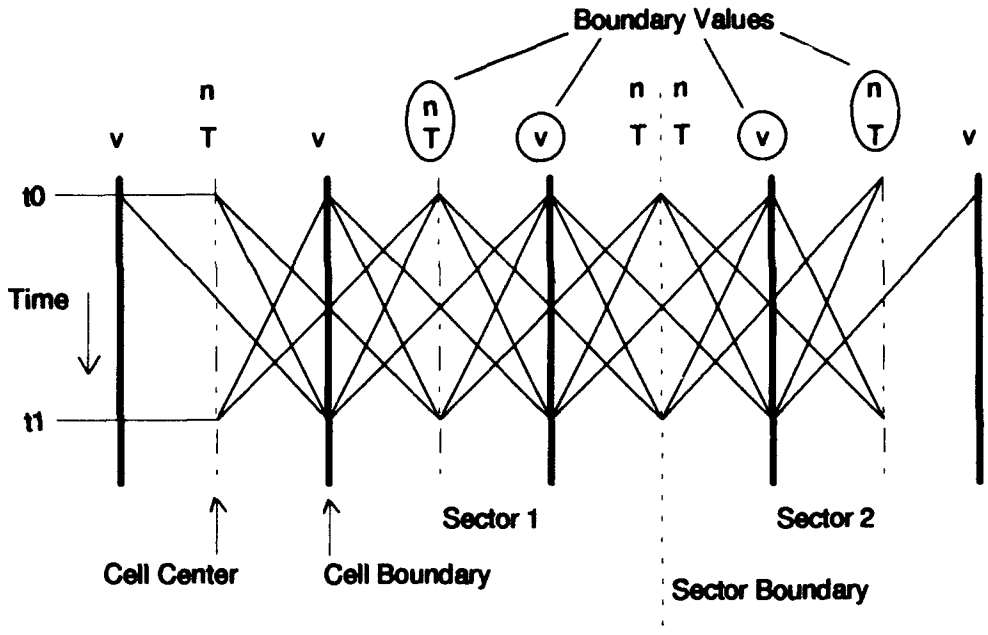

Figure 16. Time Sequencing in Fluid Calculation.

the density, temperature and drift velocity are calculated -- including the values at the sector boundary -- based on the boundary conditions provided at the end of the previous time-step. The new boundary values (the drift velocity at the first minor grid-point and the density and temperature at the first major grid-point away from the sector boundary) are transferred to the interfaces at the sector boundary. After all the sectors have executed, each sector gets the updated boundary conditions from its left and right interfaces, which get the boundary conditions from their neighboring interfaces. This technique ensures continuity of the first derivatives of the three principal quantities calculated at the interface because both sectors calculate the first derivatives based on the same set of values. With the same initial and boundary conditions and the same grid spacing, then, this technique calculates values at the interface using exactly

the same information that would be used if the interface were eliminated and a single sector calculation used instead. Thus, the interface algorithm will produce values at the boundary between two fluid sectors that are continuous across the boundary and the same as if they were calculated using a single sector calculation, as desired. To allow for a variable grid spacing, the grid spacing is passed between neighboring sectors when they are created and these values are used to correctly calculate the first derivatives and averages at the interface.

The PIC-WALL Interface. The PIC-WALL interface used in the code is a modification of that used in the code PDP1 and discussed by Birdsall (4:405-408). The injection rate of particles into the sector is determined from boundary conditions supplied by the user through the input file. In PDP1, the user specifies a particle weighting and an emission current density. Based on those values, an injection rate is calculated on a particles-per-time-step basis. In our implementation, the desired injection rate is specified by the user and the particle weight calculated. The injection rate is a floating point quantity, but only whole particles (integer quantities) can be injected. To allow the fractional part of the injection rate to accumulate, the whole injection rate is added to an accumulator at each time-step and the integer portion of the value in the accumulator injected. That integer portion is then decremented from the accumulator.

'Injection' of a superparticle computationally involves selection of an injection velocity, adjustment to the velocity for the electric field at the wall,

calculation of a position, and the delivery of the particle to the corresponding species in the sector, and (if the wall is the left wall of the simulation) decrementing the particle charge from the surface charge stored in the interface. Particles velocities are selected for injection by sampling from a drifting Maxwell-Boltzmann thermal distribution with a drift velocity and temperature specified by the user through the input file. The particles are assumed to have come into the simulation across the boundary at uniform temporal spacings in each time-step, and their position and velocity adjusted accordingly for the portion of the time-step spent in the sector. Particles leaving the sector through the PIC-WALL boundary are destroyed. If the wall is the left wall of the simulation, the charge of particles leaving the sector is accumulated in the interface surface charge density for use in calculating the electric field.

PDP1 allows the user to specify either the potential across the electrodes (along with particulars of the external circuit), or the current through the external circuit from the right electrode to the left electrode. Because this effort is concerned with devices that are current controlled and in which a single value of the voltage can correspond to two different currents, the model is restricted to a user specified current in the external circuit. Internally, within the inter-electrode space, the total current will be the sum of the conduction current (due to the actual movement of the charge carriers) and the displacement current, arising from the time rate of change of the electric field.

The FLUID-WALL Interface. The FLUID-WALL interface was implemented in the hybrid code solely for diagnostic purposes. Its was designed to allow a fluid-PIC or fluid-PIC-fluid calculation, and is intended to provide an interface between a fluid sector and a region with a constant density, temperature and drift velocity. The boundary conditions that must be supplied, then, are the same as in the case of the Fluid-Fluid interface: the drift velocity, density and temperature in the region the wall represents.

To implement this interface in the hybrid code, the electron and ion initial densities temperatures and drift velocities from the input file are used. A uniform drift, density and temperature is assumed for each species (electrons or ions) across the entire simulation, so that the values for the boundary conditions on the right wall are identical to the left wall.

The PIC-FLUID Interface. The most intriguing interface of all, and the heart of the hybrid PIC-Fluid model, is the interface between PIC and Fluid sectors. A discussion of the interface can be nicely organized around what each model needs from the interface and how the interface satisfies these needs using information polled from its neighboring interface. The discussion that follows will first treat the needs of the fluid model, then those of the PIC model.

As discussed previously, the fluid model used in this work assumes that the velocity distribution functions for the electrons and ions are full, drifting Maxwellians at all grid points inside the sector. For benchmark calculations (and consistency), a hybrid calculation of a quiescent plasma with Maxwellian

velocity distributions of electrons and ions, should produce the same results as a PIC-only or fluid-only calculation. Given a Maxwellian particle distribution, then, the interface between the PIC and the Fluid sectors must be able to translate the particle information inherent to the PIC calculation (number density, particle position and velocity) into a set of consistent density, temperature and drift velocity parameters.

There are a number of ways this could be accomplished. The approach taken in this work is to use the same formulation of the fluid equations at all points in the fluid sector, including the points at the boundaries. Using this approach, the PIC-FLUID interface (from the fluid side) looks like a FLUID-FLUID interface, and the fluid sector simply requires the values of the density, temperature and drift velocity at the first major and minor grid-points on the PIC side of the interface. The values of the density and temperature at the first major grid-point within the PIC region are used, as opposed to the major grid-point on the boundary, because (as shown in Appendix A) the values calculated by the PIC sector for the major grid-point at the boundaries are less precise.

While the PIC sectors calculate the density directly, there is no inherent assumption of a velocity distribution function, and therefore no definition of temperature or drift velocity. These values have to be obtained directly from the particle distribution by polling all the particles near the interface and calculating the average velocity and energy. The average velocity of a Maxwellian

distribution is by definition the drift velocity. The temperature can be calculated by subtracting the energy associated with the drifting motion from the average energy. Mathematically,

$$\frac{3}{2}kT = \overline{E} - \frac{1}{2}mv_d^2 \tag{61}$$

where k is Boltzmann's constant, T is the temperature, $\overline{E}$ is the average energy, m is the particle mass and v_d is the drift or average velocity. If the particle distributions in the PIC sector are truly drifting Maxwellians, this technique conserves particle flux, momentum flux and energy flux because it provides a completely consistent representation of the particle distributions across the interface.

The PIC sector only desires one thing from an interface: injected particles representative of the velocity distribution on the fluid side of the interface. Again, a hybrid calculation should model a quiescent plasma with Maxwellian velocity distributions of electrons and ions, and get the same results as a PIC-only or fluid-only calculation. To accomplish this, the interface between the PIC and the Fluid sectors must be able to emit particles with velocity distributions consistent with the assumed form in the fluid sector at the interface. At a PIC-WALL interface, when the assumed form of the distribution is a drifting Maxwellian, a directed flux, temperature and drift velocity are used to create particles for injection as described previously. A interface consistent with this approach can be provided at a PIC-FLUID boundary as the quantities provided

to the PIC-WALL interface come naturally from the fluid sector's treatment of the species as drifting Maxwellian distributions. The temperature is provided directly from the major grid-point at the interface, as calculated by the fluid sector. The drift velocity at the interface is an average between the drift velocity calculated at the first minor grid-point on the fluid side of the interface and the value obtained from the first minor grid-point in the PIC sector as a boundary condition to the fluid sector. The directed flux is not explicitly calculated in the fluid sector, but an expression for its value can be obtained by integrating the velocity distribution function weighted by the velocity. For a right directed flux, the integral is taken over all positive values of the velocity. Conversely, for a flux directed to the left the integral is taken over all negative values. This results in the following expressions for the flux to the right and left respectively:

$$\Phi_R = n\left(\frac{v}{2}\left(1+Erf\left[\sqrt{\frac{m}{2kT}}v\right]\right)+\sqrt{\frac{kT}{2\pi m}}Exp\left[\frac{-mv^2}{2kT}\right]\right) \tag{62}$$

$$\Phi_L = n\left(\frac{v}{2}\left(1-Erf\left[\sqrt{\frac{m}{2kT}}v\right]\right)-\sqrt{\frac{kT}{2\pi m}}Exp\left[\frac{-mv^2}{2kT}\right]\right) \tag{63}$$

where n is the species density, v is the drift velocity, m is the mass of a species particle, k is Boltzmann's constant and T is the species temperature, with all quantities calculated at the boundary. The flux to the left is provided to the interface to use as the boundary condition on the flux for the right side of a PIC sector and the flux to the right for a boundary condition on the left side of a PIC sector. With these expressions for the directed particle flux, an interface can be

built that exactly represents (to within the noise inherent in the PIC approach) a continuous drifting Maxwellian distribution of particles across an interface between a fluid sector and a PIC sector. Put into a code modeling a drifting Maxwellian in both the PIC sectors and the fluid sectors, this technique conserves particle flux, momentum flux and energy flux because it provides a completely consistent representation of the particle distributions across the interface so long as both sides of the interface are what they claim to be.

At this point, a word needs to be said regarding the PIC-fluid hybrid calculation and sub-cycling. The PIC calculation is limited by particle velocities and cell dimensions to a time-step of a picosecond. As mentioned in the section on the fluid module, the fluid calculations must be run at time-steps of 0.025 picoseconds due to stability and accuracy issues. The boundary conditions supplied by the PIC sector to the interface are exactly as specified in the preceding paragraphs. For the fluid, however, an adjustment must be made to allow for the smaller time-steps. There are two parts to this adjustment: adjustments to values the fluid sector uses, and adjustments to values the fluid sector produces.

The values used by the sector are provided as initial conditions at the beginning of each major time-step. These values are compared to the values at the last major time-step and the difference calculated. At each subcycle time-step, a fractional part of the difference between the new value and the old value

is added to the new value to estimate the change in the value over the space of a subcycle time-step. The electric field in the fluid sector is calculated at each subcycle time-step to allow for the changes in the sector densities. This, it turns out, is essential for a stable calculation.

The values stored in the interface by the fluid sector are accumulated each subcycle time-step. Before they are used by a PIC sector, they are averaged over the number of subcycles in the fluid sector. Thus, these values represent averages taken over a single PIC time-step, consistent with the assumptions made during injection of particles into the PIC sector at a fluid boundary. For a FLUID-FLUID interface, however, a temporal error is introduced because the values provided at the interface are not the values at the end of the time-step but averaged over the time-step. If this work relied on or used fluid-fluid interfaces (it doesn't , they are provided only for diagnostic purposes) an adjustment to the stored information would have to be made for that case.

Program Description.

Now that the details of the modules and interfaces have been discussed, a higher level description of the program that implements them will be presented. When the hybrid program is executed, it creates the graphical user interface and a single instance of the simulation object. The graphical user interface is treated as an independent object, allowing the program to be run with or without the

user interface. The simulation object is that part of the program that actually sets up the problem -- based on the user input file -- and controls the calculations. When the user interface is invoked, it reads in a copy of the input file, which can be edited using the built-in text editor. Program execution loops at the program level until the user is satisfied with the input file and presses the Execute button on the user interface. Program control is then passed to the simulation object.

Simulation Level Description

At the simulation level, the space being modeled is divided into a series of interacting sectors, separated by the interfaces discussed above. The simulation object reads in program data, creates the sectors and interfaces, reads and saves dump files, initiates the sector calculations, initiates the calculation of the electric field at the end of each time-step, coordinates the transfer of information between sectors, and controls data flow at its own level with the user interface.

The program flow at the simulation level is presented in Figure 17. When program control is passed to the simulation object by the main program, the simulation checks to see if a dump file is to be loaded. If so, the file is loaded and the surface charges at the interfaces initialized. If not, the simulation checks to see if an initial particle loading is desired. If so, each sector is ordered to

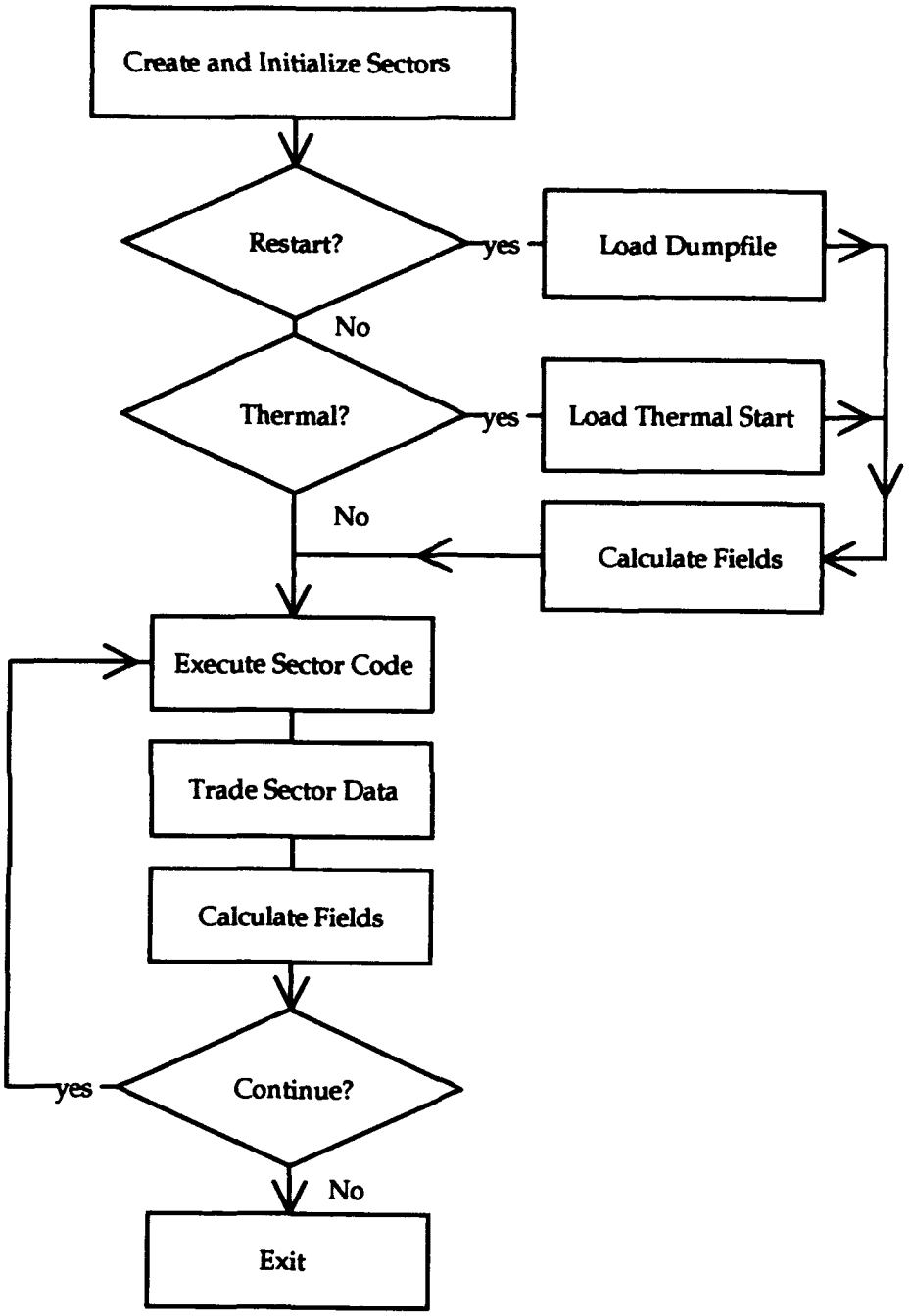

Figure 17. Simulation Level Program Execution.

create the distributions needed and the initial electric fields are calculated. Once the simulation is initialized, the execution of individual time-steps can begin.

At each time-step, the simulation calls the execution module for each sector. Each sector is then responsible for performing the calculations peculiar to its own nature. Once all sectors have executed their peculiar calculations, the simulation has the sectors trade information with each other as to the densities, temperatures, drift velocities and fluxes across the boundaries. Any particles that would have crossed over into the PIC sectors from the walls or neighboring sectors are injected, then all the particles in the particle simulations are given the opportunity to collide using Monte Carlo techniques. Finally, electric potentials and fields are calculated beginning with the rightmost sector and continuing to the leftmost sector. Program execution loops back until the user presses the "Quit" button on the command panel or from a menu and the program terminates.

Sector Level Description

At the sector level there are two fundamental approaches to modeling the charged particles moving in the inter-electrode space: the PIC approach and the fluid approach discussed above. The user specifies in the input file which approach he wishes to use for each sector, and the simulation passes this information to the sectors. Each sector is subdivided into a number of cells, with

each cell having at its center a numerical grid-point. The number of cells per sector is specified by the user, and can vary from sector to sector. This enables the use of a fine mesh in sectors where the fields and densities have strong spatial gradients, and a coarser mesh where the gradients are small.

When initialized, the sectors create the species objects they will need (ions and electrons), and initialize their left and right interfaces. The species serve as mount points for linked lists of particle objects. Particles are either read in from a dump file, created by the sector at start-up (if a thermal distribution is specified), created by ionization events, or received by transfer from the interfaces. The sectors also create the grid object on which the sector variables and fields will be tracked.

Sectors execute a single time-step when instructed to do so by the simulation object, using either the PIC or Fluid module. PIC sectors update the acceleration, velocity and position of each particle; particles that move outside their sector boundaries are eliminated by transfer to the interfaces, where they are stored. Fluid sectors calculate the flux out of their sectors as boundary conditions for their neighbor sectors, and calculate the new temperatures, densities and drift velocities based on the boundary conditions provided by their interfaces.

The PF User Interface

The computer code implementing the PIC-Fluid hybrid model is written in C++, using the Objectworks for C++® version 3.0 compiler, and runs on a SUN SparcStation ®. C++ was chosen as the programming language because the model and the graphical user interface lend themselves to an object oriented approach, in which the sectors, the particles passed between sectors, the grid on which quantities are calculated and the graphical display of the results of the calculation are treated as semi-independent objects that interact with one another.

Neither particle simulation methods nor fluid techniques strictly require any sort of graphical user interface. One could write the computer codes and have them periodically dump their data for later post-processing as has been done in the past. In doing so, however, one throws away a wealth of information as to the evolution of the calculation, and misses the opportunity to catch possible errors or non-physical situations as they are developing. The ability to observe non-physical behavior as it develops can be especially important in debugging a code. A well constructed graphical user interface capable of plotting the data as it is generated also provides a visual interpretation of the calculation that is extremely useful. Visualization helps the user to develop insight into the intricacies of both the numerics and the physics involved in numerical simulation. For these reasons, together with the

availability today of relatively inexpensive, high-speed graphics terminals, the inclusion of a graphical display in a numerical simulation should be considered essential.

The user interface for the model was written specifically for this application using X-View constructs developed with the help of sample X-View subroutines shipped with the OpenWindows® version 3.0 windowing environment. The interface was rewritten using DevGuide® to ease the interface maintenance requirements as the interface grew in complexity. While the interface was written specifically for this application, it was designed to be easily integrated into other applications. The interface utilizes standard Open-Look® buttons, icons and dialog boxes to provide control of the program and the graphical display of the results of the calculations.

When the code is executed, an input file describing the problem to be solved is read into a built-in text editor identical to the standard text editor provided by the OpenWindows® windowing system. At the top of the editing window is a control panel containing a series of "buttons" which can be "pressed" using the left mouse button. These buttons control the operation of the program and the flow of the calculation. Once any editing changes have been made to the input file, pressing the Execute button displayed on the control panel at the top of the editor window initializes the program. If the user has edited the input file, he is asked if he wishes to save the edited file.

Additional program control is provided by the Run, Step, Stop and Quit buttons. Pressing the Step button instructs the program to cycle through the execution process, stepping forward a single time-step. The Run button instructs the program to continuously cycle through the execution process until the Stop or Step button is pressed. Pressing the Stop button suspends the execution process until the Run or Step button is pressed. Pressing the Quit button terminates the program.

A number of dialog boxes also provide program control and are accessed by buttons on the main control panel. The DumpFile dialog box allows the user to load a dump file prior to execution (dump files are used to save the state of a previous calculation), change the dump file name or manually initiate a dump of the current program state during a calculation. The Parameters dialog box provides control over the generic features of the graphical display such as the plot interval, steps between history updates, and the number of steps over which to take running averages for the time averaged displays. The Parameters box also gives the user the ability to alter the particle injection rates, the interval over which to produce dump files, the "target" external circuit current during the calculation, and the number of time-steps over which to approach the target current. The "target" current is the current in the external circuit that is to be reached after a user specified number of time-steps. At each time-step, the value of the current in the external circuit is incremented or decremented to allow for a

gradual shift in the operating conditions of the device being modeled. This feature was implemented to give the user control over the external circuit current during a calculation while minimizing the noise introduced by large changes in the current's value.

The graphical displays are accessed by pressing the Diagnostics button displayed on the main control panel. This provides the user with a choice of the following diagnostic charts as a function of position: velocity in the propagation direction (x-Vx), velocity perpendicular to the propagation direction (x-Vperp), kinetic energy(x-eV), density, electric field, potential, charge density, temperature, flux, current density, and actual pathlength traveled by particles in the simulation. Diagnostics are also available that display the temporal evolution (histories) of the number of particles in the simulation, and the values of the potential and electric field at the left boundary of the inter-electrode space. These are essential for determining whether steady state solutions have been achieved. Finally, a diagnostic is provided that displays particle velocity in the propagation direction vs. particle velocity perpendicular to the propagation direction(Vx-Vperp). This diagnostic is particularly helpful in determining if particles coming from different sources have the same total velocity distributions. Most of the diagnostics can be displayed either at a simulation level or on a sector by sector basis. Some, such as the potential and electric field, provide time averaged values of the instantaneous values they display. The time averages are taken as running averages with a user specified averaging

window. Any or all of the diagnostics may be selected for display; once a diagnostic has been selected for display, if it is later de-selected it collapses into an icon labeled with the distinctive AFIT logo and the plot type. When a diagnostic is closed to an icon, it is not updated as the data change. Thus, when speed is desired, the diagnostics can be closed and the overhead associated with the user interface minimized.

When the cursor enters a diagnostic window it changes into a bulls-eye. Pressing the left mouse button displays the value of the point under the bulls-eye on the bottom of the plot window. Pressing the middle mouse button displays the maximum and minimum abscissa values in a greater precision than displayed on the plot. Pressing the right button brings up a menu with all the commands that are on the top of the editor window (in case it is obscured) as well as a Trace command (which prevents the erasure of the screen prior to plotting subsequent data), a Print command (which copies the values plotted to a file) and a Rescale command. The Rescale command opens a Rescale window, from which the user can adjust the plot scaling, the colors used for background and foreground, and the colors of the individual traces. The user can also "turn off" the display of individual traces. This last feature, combined with the fact that species are tracked not only by their particle type but also by their origin, allows the user to selectively display and examine the evolution of individual injection streams of particles. The ability to selectively "turn off" traces can also

be very helpful in understanding diagnostics on which many traces are displayed and may obscure one another.

There is a small amount of overhead associated with running in a windowed environment, as the window manager takes up some of the computer's processing time. For this reason two features were added to the code. The first is a Dismiss button which dismisses the graphical user interface entirely, allowing the windowing environment to be exited so that the calculation can have all the available processing time. The second is a start-up flag '-s', indicating that the code is to be executed in the 'silent' mode, that is, without the user interface. If either of these options are exercised, the code will perform the calculation based on data in the input file and produce dump files at the user specified intervals. The dump files can later be read in and analyzed or used to restart the calculation.

With these features, the graphical user interface designed for this application provides a professional quality user interface and greatly enhances the flexibility and usefulness of the underlying models.

Validation of the PIC-Fluid Hybrid Code.

The thrust of this work has been to take two proven techniques for modeling plasmas, PIC and the Fluid equations, and mate them together. For the PIC module, algorithms already developed and implemented in a widely

used PIC code called PDP1 were used. Similarly, new fluid equations were not re-derived, but rather those already derived by Holt and Haskell with the collisional treatment of Golant et al. were used. This being the case, the validation requirements are rather simple. We need to demonstrate that the implementation of the PIC algorithms from the PDP1 code produces correct results, and where this work deviates from the algorithms of PDP1 (the multi-sector approach and corrections to the collisional model) it must be shown that the modifications have been effective in producing the desired results. For the fluid model, it must be demonstrated that this implementation is functioning correctly and matches results calculated either analytically or using an independent collisional model as a cross-check. Finally, the interface between the PIC and Fluid sectors must be demonstrated to be functioning correctly given a proper set of initial and boundary conditions.

It is convenient to begin by discussing the validation of the collisionless PIC portion of the code. As the code was under development, a number of calculations were run as cross checks to ensure that the results of a collisionless calculation made with the hybrid code were consistent with those calculated using PDP1. For every case, the codes were found to be in excellent agreement. Having said that, an analytic calculation is desirable to show that beyond matching those of PDP1, the values produced by the new code are correct within the limitations of the PIC formalism. One such analytic calculation is that of the ideal diode. This is a particularly interesting calculation in that not only is the

result analytic, it stresses every portion of the collisionless PIC technique and can be used to check the results of both a single sector and multi-sector PIC approach.

Recall from Richardson's equation that when the current density in the external circuit is less than the emission current density, the magnitude of the retarding potential across an ideal diode rises logarithmically as the external current falls, so that

$$V = \frac{-kT_E}{e} \ln\left(\frac{J_{ext}}{J_E}\right) \tag{64}$$

where V is the retarding voltage across the diode, k is Boltzmann's constant, T_E is the emitter temperature, e is the elemental charge, J_{ext} is the current in the external circuit divided by the electrode area, and J_E is the emission current density. Any actual diode will develop a retarding potential due to the space charge of the electrons in the inter-electrode gap, although the space charge can be reduced by making the electrode gap very small.

For a current ratio (J_{ext} / J_E) of ½ and an emission temperature of 1000 K, the value of the retarding voltage using Equation (64) is found to be 0.0597335 volts. With an emission temperature of 1000K, the time required for an electron with a thermal velocity to travel about a hundredth of the way across an inter-electrode gap of an inter-electrode gap of $^1/_{3}\text{x}10^{-8}$ m is $5.0\text{x}10^{-16}$ sec. Using this for the time-step and an emission current density of 20000 amps/m^2, both the

single sector and a three sector PIC calculation produce identical values of 0.0597406 volts, differing from the analytic value by only 0.01%.

This relatively simple calculation provides a validation of the implementation of both the single sector and the multi-sector PIC formalism, and a validation of the PIC-PIC interface. The simplest way to provide a validation for the collisional model in the PIC module is to compare the results of a collisional PIC calculation to a calculation including the same collisional processes but using a very different calculational technique. For this procedure, the fluid module (absent the ionization and recombination kinetics) developed for the hybrid calculation will serve very nicely. If results of a PIC-only calculation agree with those of a PIC-Fluid-PIC calculation, the two calculation will serve as cross-checks of one another as it is unlikely that they would both contain the same errors because of the gross differences in the techniques (all they share in common is the Poisson equation solver which has already been validated in the ideal diode calculation). This cross-check will also serve as a validation of the PIC-FLUID interface under conditions where actual drifting Maxwellian velocity distributions exist on either side of the PIC-FLUID interface.

Two sets of calculations were performed. The first set used singly charged ions with masses 1000 times that of the electrons. The ion charge exchange cross section was set at 1.0×10^{-17} m^2 and the electron-atom scattering cross section was set at 3.5×10^{-18} m^2. Both ions and electrons were injected from

the left and right boundaries with current densities of 10^4 amps/m^2 each and temperatures of 1700 K. There was no current in the external circuit.

When the first set of calculations began, an initial Maxwellian distribution of electrons and ions at a temperature of 1700 K and a density of 5.0×10^{18} m^{-3} was uniformly loaded throughout the inter-electrode space; there was no net charge density and no electric field. The ion injection current density specified at the boundaries is much greater than in the initial Maxwellian distribution (10^4 amps/m^2 as opposed to 324 amps/m^2). To maintain charge neutrality in the bulk of the plasma, a potential barrier to the ion current density develops in the sheath regions to slow down the ions.

The average, steady-state values of electric field resulting from a single-sector PIC calculation, a three sector PIC calculation (the traces labeled "Edge PIC" refer to the two sectors at the boundaries and the trace labeled "Mid PIC" to the sector in the middle), and a hybrid PIC-Fluid-PIC calculation are plotted in Figure 18. The average values of the field were calculated over several plasma periods to reduce the particle noise. As can be seen in the figure, the traces of all the plots obscure one another due to their close agreement.

The scale of the middle section of the plot in Figure 18 is expanded in Figure 19 to further detail the behavior of the various techniques in the middle sector and at the interface to the edge sectors. As can be seen, the techniques all match one another to within the noise inherent in the PIC technique. For the calculation illustrated in the figure, the number of electrons per superparticle

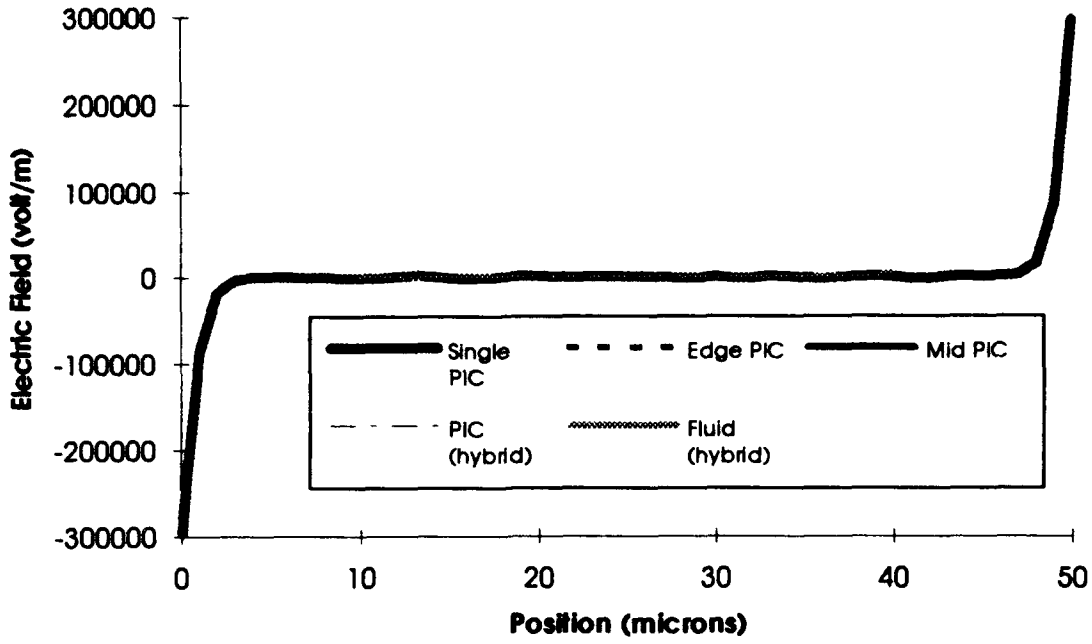

Figure 18. Calculation of the Electric Field Using Various Combinations of Techniques.

was 624219, and the electrode area was 10^{-4} m^2. The electric field associated with a single superparticle is 113 volt/m. Thus, the noise in the electric field corresponds to variations between cells of only about 18 charged particles. For a density of $5x10^{18}$ m^{-3} and a cell width of 10^{-6} m, there are about 800 particles per cell. Based on statistical variations alone, deviations of on the order of 28 particles per cell (the square root of the number of particles in each cell) are expected so the results are well within the noise of the calculation. In passing, the noise in the field is a direct consequence of the number of electrons per superparticle. If the current densities in the simulation are reduced to the milli-

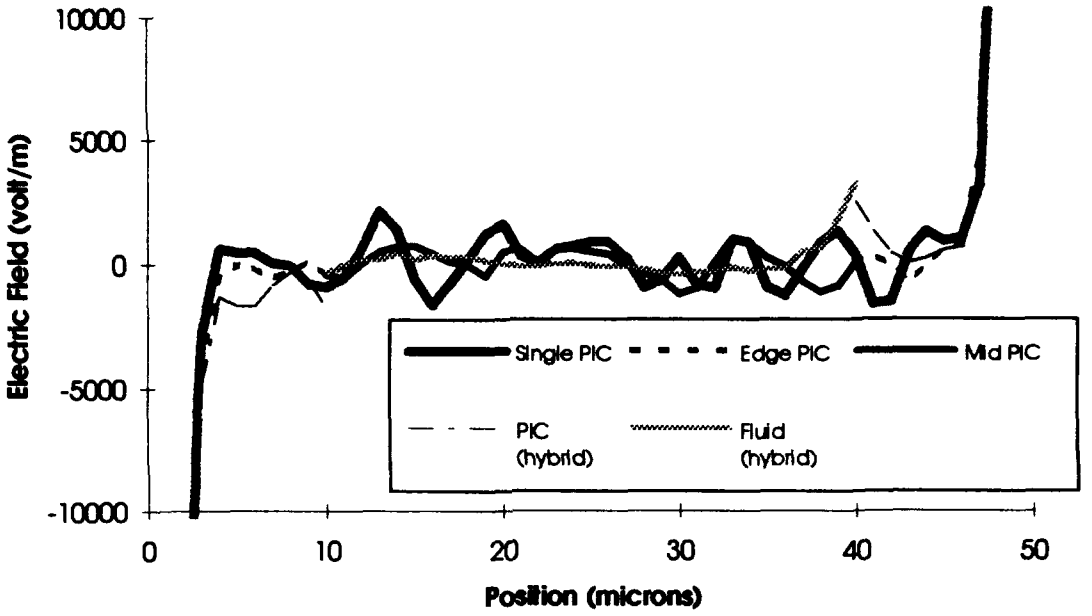

Figure 19. Expansion of Time Averaged Electric Field Calculated using Various Techniques.

amp per cm^2 level, the noise in the field drops to the on the order of 10's of volts/meter.

The electron density calculated by each of the techniques is plotted in Figure 20. As with the calculation of the electric field, there is no significant difference in the values calculated by any of the techniques, all produce a value in the middle of the plasma region of about $5x10^{18}$ m^{-3} falling to a minimum value at the walls of about $2x10^{18}$ m^{-3}. The noise in the calculated density profile associated with each of the techniques is typical of the PIC calculation for the number of particles used. The statistical variations of 28 particles per cell leads to a deviation of the density between any two cells of $4x10^{17}$ $meter^{-3}$, consistent with the figure. Unlike the values plotted for the electric field, the values plotted

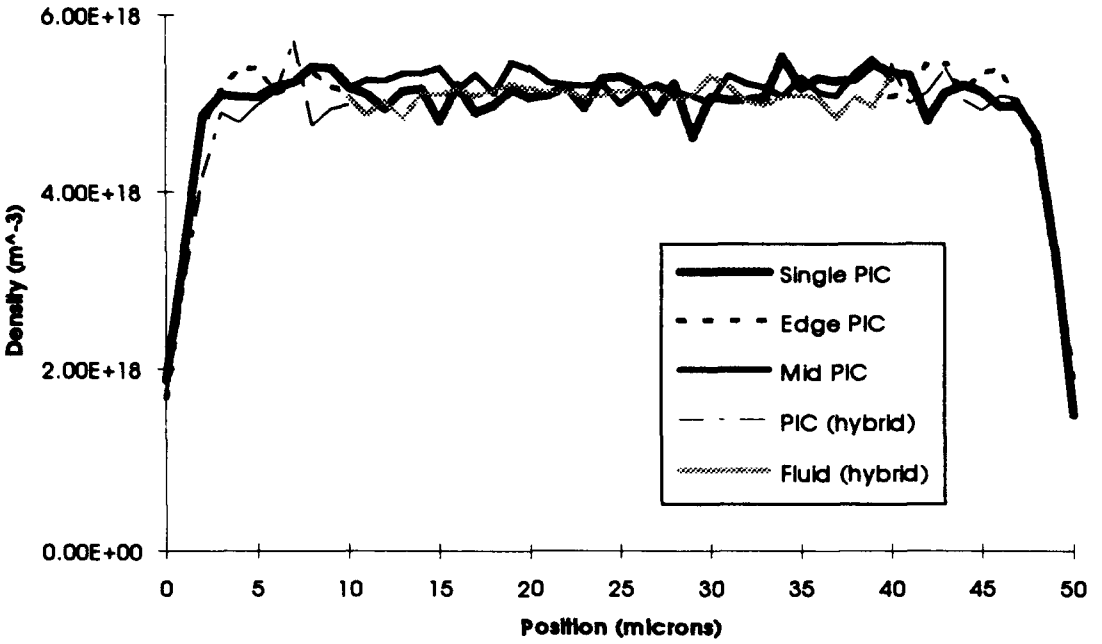

Figure 20. Electron Density as Calculated by Various Combinations of Techniques.

here are instantaneous values taken after the calculation had achieved steady state, but they are representative of the profile at any given instant – the location of the peaks and valleys in the density would be different at another instant, but the magnitude of the average cell-to-cell deviations would remain constant.

A snapshot of the instantaneous ion density after steady state has been reached is presented in Figure 21, and the results are much the same as for the electron density. All approaches produce the same values to within the average noise inherent in these types of calculations.

As an additional cross-check on the validity of the fluid and PIC collisional models and interfaces, calculations were performed with the ion mass

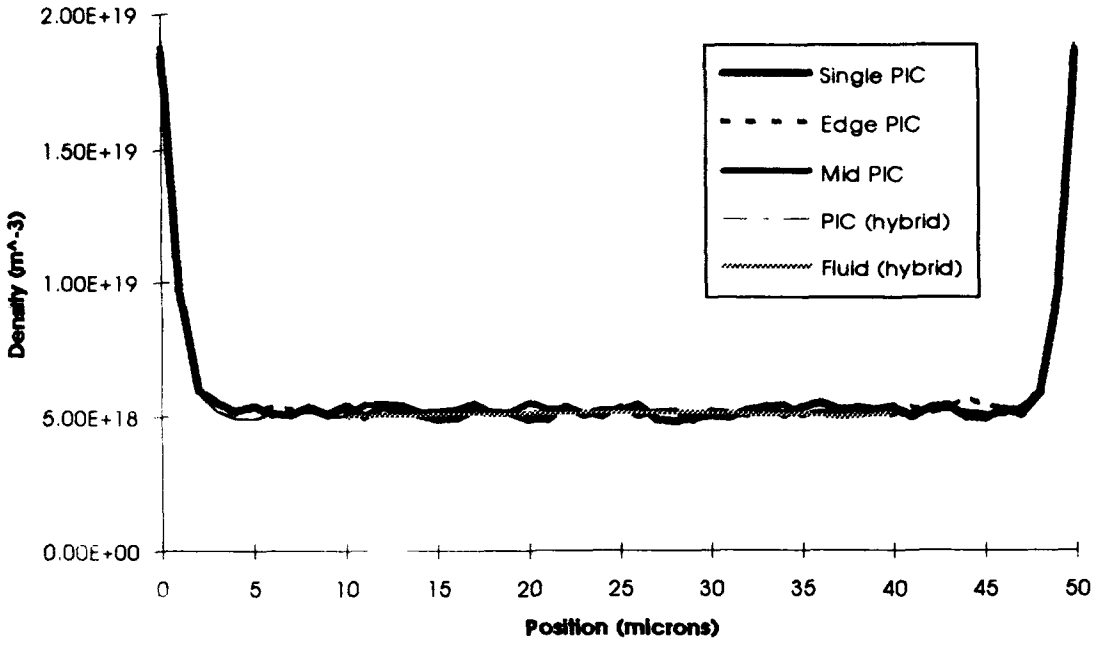

Figure 21. Ion Density as Calculated by Various Combinations of Techniques.

equal to that of a cesium ion. Injection current densities, and initial densities and velocities were set to match those of drifting Maxwellian velocity distributions using differing temperatures for the ions and electrons. Under these conditions, one expects no change in the temperature, velocity or density, and no appreciable electric fields. The results of these calculations were the same as for the calculations presented above: the fields, potentials, temperatures, fluxes and densities calculated using single PIC, multi-sector PIC and PIC-Fluid-PIC techniques all matched one another to within the noise associated with the PIC calculation.

The excellent agreement between the collisional PIC and fluid modules serves to validate both models and the PIC-FLUID interface to the extent that

they modeled the same types of collisions and the same velocity distributions, but there are some aspects of the collisional model both in the PIC and in the fluid module which have not been validated. No attempt was made to validate the ionization model or the excitation model in the PIC treatment, because they were not intended for use in this work. They are included in the code for completeness but still require validation. Similarly, the calculations using the hybrid model never reached the point of using the ionization model in the fluid treatment, rather, in the cases examined the ionization rate was set to zero. The ionization model used is that of Norcross and Stone(42:655), and was taken from a code developed early in this effort to implement the algorithms of Lawless and Lam. When that code was written, plots of the ionization rates calculated using the Norcross and Stone model were compared to plots of the ionization rate made by Lawless and Lam using the same model and were found to be in agreement. No such comparison has been made in the current implementation, however, as other concerns about the model took precedence, as will be discussed in the next chapter.

Conclusion.

Because the collisionless model of the sheaths in high-pressure, ignited mode thermionic converters predicted sheath thicknesses that were several collision mean-free-paths thick, a hybrid plasma model has been developed

using collisional Particle in Cell (PIC) techniques in the sheaths and a set of fluid equations in the bulk of the plasma. The fluid and interface models assume that the plasma at the PIC-Fluid interfaces has a velocity distribution closely approximated by the Maxwell-Boltzmann velocity distribution, allowing for a non-zero drift velocity. The single-sector PIC portion of the model was tested against bounded analytic calculations for an ideal diode with excellent agreement. The multiple-sector PIC implementation was cross-checked against the single-sector and also found to be in excellent agreement with both the single sector calculation and the analytic results. Finally, collisional calculations using the fluid module were cross-checked against single and multi-sector PIC calculations and again found to be in excellent agreement.

The conditions provided to the model in the validation calculations test the model under conditions strictly in accordance with the assumptions that went into the model. In the next chapter, the hybrid model is applied under conditions typical of a high-pressure, ignited mode thermionic converter.

Chapter IV. Application to Modeling of Thermionic Converters

Introduction

In the last few chapters the need for a collisional technique to model the sheaths in high-pressure thermionic converters was discussed, and to that end a hybrid Particle in Cell (PIC) - Fluid model was developed, assuming that the velocity distributions at the sheath-plasma boundary were close to Maxwellian. The model was validated against analytic calculations and under circumstances which matched the assumptions made in its development.

This chapter reports the results of an application of the model under conditions typical of thermionic converters. First, a description of the velocity distributions that developed at the plasma-sheath interfaces in the presence of the ignited mode sheaths will be presented, along with a discussion of the physical phenomena leading to their formation. Next, the impact of the departure from the assumed form of the velocity distribution on the performance of the hybrid code will be presented and analyzed. Conservation of energy, momentum and particle flux will be discussed in this section, as well as the effects of alternative interface formulations. Finally, suggestions will be made for changes to the hybrid model to increase its robustness and make it suitable for modeling thermionic converters.

The Observed Electron Velocity Distribution

Recall that the particle velocity distributions at the interface were assumed to be Maxwellian. This assumption was used both to translate the particle data from the PIC sectors into the macroscopic variables used in the fluid equations, and to create the distribution of particles needed at each time-step for injection back into the PIC sectors from the Fluid sector. Figure 22 presents a phase-space portrait consistent with a Maxwellian velocity distribution. In the figure, the magnitude of the distribution function is plotted as a function of the x-component and the perpendicular component of the velocity. When the hybrid model was applied under conditions typical of ignited-mode thermionic converters, the distribution observed at the interface was clearly non-Maxwellian, and looked much closer to that illustrated in Figure 23.

To understand the observed form of the velocity distribution, it is helpful to understand the physical processes that lead to its development. When the electrons are injected into the PIC sector, they are injected with a velocity distribution represented by the positive or negative x-velocity portion of a Maxwellian velocity distribution, and with the temperature of the surface from which they were emitted. This distribution is referred to as a half-Maxwellian or a single-sided Maxwellian. If the emitting surface is the right wall of the device, the negative portion of the velocity distribution is used; if the emitting surface is

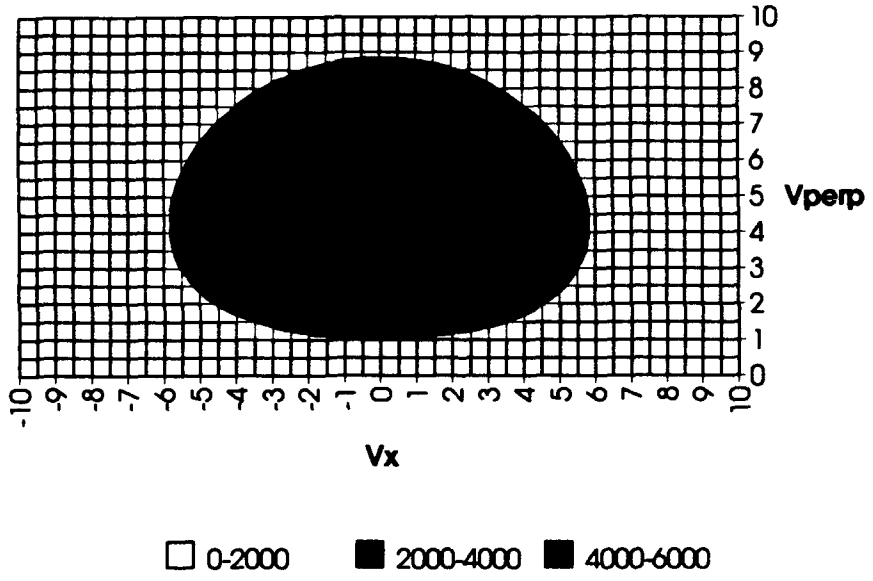

Figure 22. Velocity Phase-Space Plot of a Maxwellian Velocity Distribution (arbitrary units).

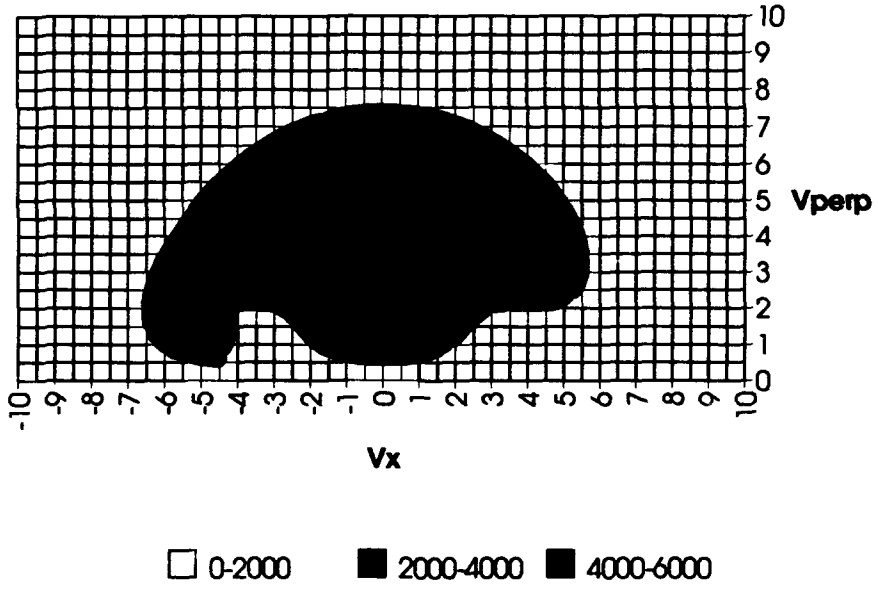

Figure 23. Observed Phase Space Plot of Electron Velocity Distribution at Plasma-Sheath Boundary (arbitrary units).

the left wall, the positive part of the distribution is used. Once the electrons are emitted into the PIC sector, they respond to the forces and kinetics represented in the sector. Three physical phenomena are of particular interest: response to the electric field, collisions with neutrals, and Coulomb collisions. Each of these effects will be discussed below, and their contributions to the observed velocity distribution function will be analyzed.

As mentioned above, the electrons are injected into the PIC sector from the wall with a half-Maxwellian velocity distribution. As discussed in Chapter 1, an accelerating electric field exists just outside the cathode (or virtual cathode in the obstructed regime) which imparts energy to the electrons as they move through the sheath towards the plasma. In the absence of collisions, the emission electrons arrive at the plasma-sheath boundary with a total energy equal to the sum of their initial energy and the energy gained when passing through the sheath. The result is a drifting, half-Maxwellian velocity distribution as illustrated in Figure 24. If the thickness of the PIC sectors used for modeling the sheaths is less than the mean-free-path for collisions, the drifting half-Maxwellian is quite pronounced at the PIC-Fluid interface. As the thickness of the PIC sectors is increased to several mean-free-paths, the half-Maxwellian contribution to the total electron distribution diminishes exponentially, becoming a small 'lump' on the side of the distribution away from the emitter, as seen on the left side of the distribution in Figure 23.

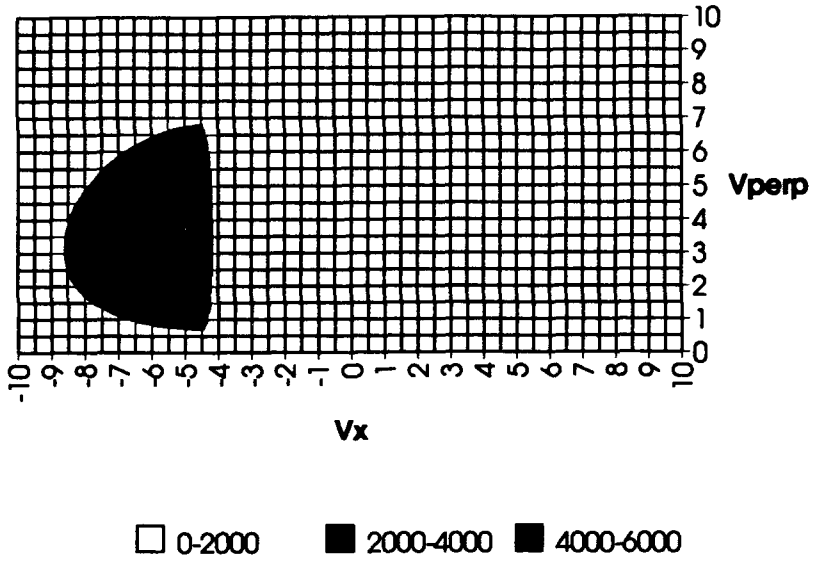

Figure 24. A Drifting Half-Maxwellian Velocity Distribution (arbitrary units).

As already discussed, the sheaths in a thermionic converter are at least mildly collisional, and the description of the drifting half-Maxwellian is not sufficient to describe the observed distribution function. The effect of electron collisions with the atoms must be included to help complete the picture. Electron collisions can be classified as inelastic or elastic. The principal inelastic collisions are excitation and ionization collisions. These are not active in the PIC model of the sheaths because of the high excitation threshold (1.4 eV) and the relatively small values of the cross section(order of 10^{-19} m^2(42:667)) when compared to elastic scattering (order of 10^{-18} m^2 (3:60)). This leaves the elastic collisions. An elastic collision between an electron and an atom has the effect of

isotropically redirecting the electron's velocity vector. Because the atoms are essentially infinitely massive with respect to the electrons, elastic collisions with the atoms result in no energy transfer from the electrons to the atoms. In a Maxwellian plasma, elastic collisions with the atoms have no net effect on the electron distribution function. But the electrons that are emitted into the sheath by the electrodes become strongly non-Maxwellian as they acquire the drifting half-Maxwellian distribution described above. Elastic collisions act to redistribute the additional energy gained by the x-component of the particle velocity vector to the perpendicular component of the particle velocity vectors. After many mean-free-paths for collisions, the electron velocity distribution becomes a shell in velocity phase space, characterized by a radial temperature and a radial offset from the velocity space origin. Such a distribution is illustrated in Figure 25.

The distribution illustrated in Figure 25 satisfies the equation:

$$f\left(v_x, v_{perp}, v_0\right) = 2\pi\, v_{perp}\left(\frac{m}{2\pi kT}\right)^{\frac{3}{2}} \exp\left(\frac{-m}{2kT}\left(\left(\left(v_x\right)^2 + \left(v_{perp}\right)^2\right)^{\frac{1}{2}} - v_0\right)^2\right) \quad (65)$$

where v_0 is a fitting parameter related to the average energy picked up by the electrons as they traverse the sheath. As described above, the form of Equation (65) is that of a non-drifting Maxwellian distribution with a radial offset (v_0) from the origin in velocity space. This distribution function is

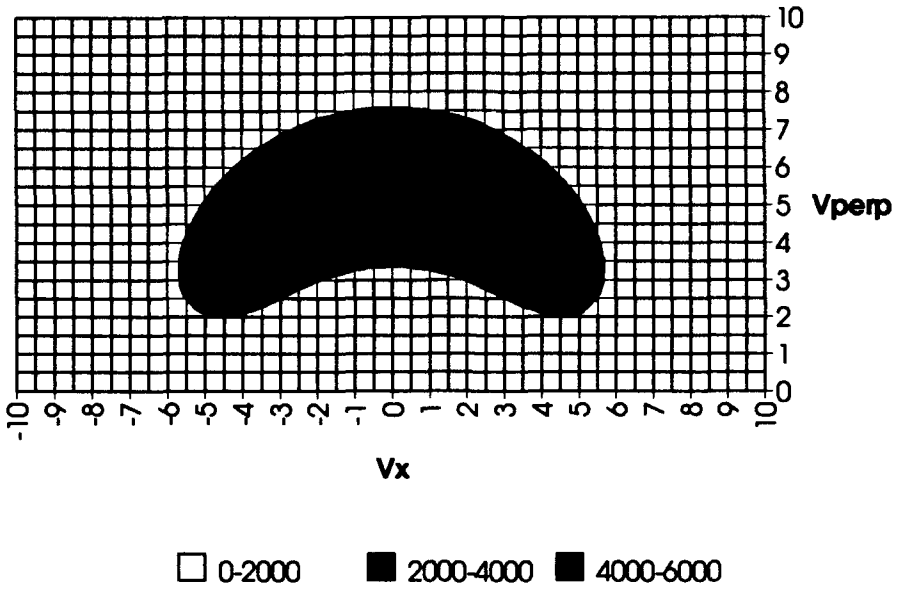

Figure 25. Velocity Distribution Resulting from the Isotropic Redistribution of the Energy in a Drifting Half-Maxwellian(arbitrary units).

referred to as a spherical-Maxwellian because, in three dimensional velocity space, the distribution function takes on the form of a spherical shell.

The mean-free-path for elastic electron-atom collisions at cesium pressures of about 2 torr is 16 microns. The calculation that produced the velocity distribution shown in Figure 23 was modeling a device with an inter-electrode gap of 254 microns thick, and a Debye length of about 3 microns (calculated at the mid-point of the device). The sheath/pre-sheath regions modeled as PIC sectors were 30 microns (~2 mean-free-paths) thick. When the thickness of the PIC sector is only a couple of mean-free-pathlengths, the randomization of the velocity vector is not complete. In this case, the velocity

distribution illustrated in Figure 26 develops. It is this distribution that accounts for the 'arch' with the 'bump' at the left end in Figure 23.

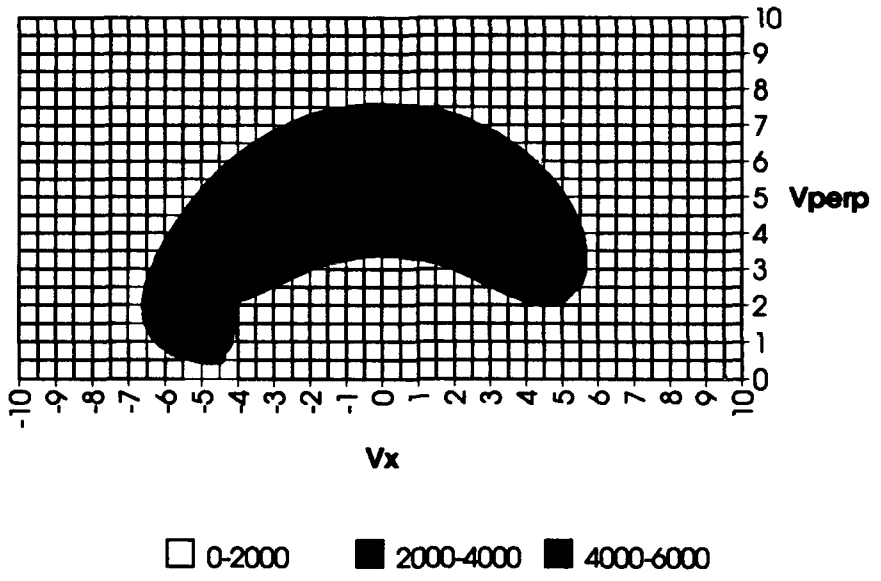

Figure 26. Velocity Distribution When Half-Maxwellian Distribution Not Fully Redistributed by Collisions (arbitrary units).

The two distribution functions described above (the drifting half-Maxwellian and the spherical-Maxwellian) account for the non-Maxwellian features of the velocity distribution function found in Figure 23. Together with the Maxwellian distribution function of the electrons from the plasma(which accounts for the symmetric 'bump' in the center of the figure, about Vx=0) they describe the distributions observed in the simulation. But what about the role of Coulomb collisions in the formation of the velocity distributions at the sheath edge? Coulomb collisions are cited as the principal method of energy transfer

between the injection and plasma electrons (41:280, 3:193-196, 42:657, 49:298), but, as already mentioned in the discussion of the PIC method, are not modeled well by the PIC method used for the sheaths. If the pathlength for energy relaxation by Coulomb collisions were small with respect to the actual distance traveled by electrons passing through the sheath, the inability of the PIC method to treat the Coulomb collisions could result in a serious error, and the actual form of the distribution function at the plasma-sheath boundary would be very different from that observed in the calculation.

Using the analysis of Krall and Trivelpiece, the mean free path for the energy relaxation of an electron by Coulomb collisions with a Maxwellian plasma can be approximated as (23:293):

$$L_c \approx \left[8\pi n \left(\frac{e^2}{mv^2} \right)^2 \ln \left(\frac{3}{2e^3} \sqrt{\frac{k^3 T^3}{\pi n}} \right) \right]^{-1} \tag{66}$$

where e is the elementary charge, n is the plasma electron density, v is the initial electron velocity, m is the mass of the electron, T is the temperature, k is Boltzmann's constant, and all units are in cgs. Using this equation for an electron with an energy of 1eV, interacting with a 3000 K plasma with a density of 10^{19} m^{-3}, the Coulomb mean free path is found to be 1200 microns – almost five times the distance across the inter-electrode space of 254 microns. The electron-atom mean free path for elastic collisions is about 16 microns in the device; due to collisions, the actual pathlength traveled by an electron through

the inter-electrode space is much longer than 254 microns. Calculations using the PIC portion of the code indicate that, on average, injection electrons traveling through the first 40 microns of the inter-electrode gap actually travel a total distance of 60 microns before first interacting with the plasma beyond. This is only 0.06 of a mean free path for Coulomb collisions -- clearly, the injection electrons are not significantly thermalized by the time they leave the sheath.

On the other hand, by the time the electrons make their way across the entire inter-electrode space they have traveled on average 6-7000 microns, more than five Coulomb collision mean free paths. This result indicates that Coulomb collisions, while insufficient to thermalize the electrons as they move across the sheath, are sufficient to thermalize the electrons as they move through the bulk of the inter-electrode space.

This observation, together with the details of the distribution function discussed above, make it apparent that our model has serious shortcomings in at least two areas. First, the assumed form of the distribution function at the interface between the PIC and fluid sectors is too simple to be able to properly model the velocity distribution of the injection particles from the Fluid sector back into the PIC sector. The interface design will only allow us to approximate the distribution function illustrated in Figure 23 using a Maxwellian with an equal total energy and net particle flux. The implications on conserved

quantities and whether a different interface design would perform better will be discussed later in this chapter.

The second shortcoming of our model results from the Coulomb collision analysis. It is clear, from the energy relaxation distance and the actual electron pathlengths, that the thermalization of the non-Maxwellian portions of the electron velocity distribution by Coulomb collisions takes place over a large region in the bulk plasma. Because the electrons are represented by a single-group Maxwellian velocity distribution, it is impossible to capture this thermalization process without resorting to some sort of distributed auxiliary heating term in the energy equation.

Response of the Model to Departure from the Assumed Velocity Distribution.

The calculations discussed above began with initial conditions consistent with a quiescent Maxwellian electron velocity distribution at temperatures and densities typical of ignited mode thermionic converters. As the calculations evolved, the current in the external circuit was gradually increased, as were the thermionic converter injection current densities at the electrodes. At the same time, the current densities consistent with a quiescent plasma were gradually diminished. As the sheaths developed, particularly at the emitter, the electron velocity distribution at the PIC-FLUID interface took on the functional form explained in the previous section. As the calculation continued (with boundary

conditions in the PIC sector that were no longer consistent with the model), the electron temperature at the PIC-FLUID interface on the emitter side of the inter-electrode space began to rise. Discontinuities in the charge density and the electric fields developed at the interfaces, apparently exacerbating the temperature rise, and the calculation eventually diverged. A number of calculations were made with larger ramp-times (the number of time-steps over which the injection parameters were changed), to see if a longer start-up time would help, but the calculation diverged regardless of how gradual the start-up.

To understand the divergence, one has to examine the underlying assumptions of the model and how those assumptions affect the conservation of particle, momentum and energy fluxes. In understanding how the interface affects those conservation issues, it is also helpful to point out the mechanisms that cause the divergence observed. It is helpful to begin by describing those mechanisms using a simple mathematical model. This model demonstrates the interplay between the PIC and Fluid modules and the external circu requirements.

As already mentioned, when the plasma sheaths developed, a beam-like component of the electron velocity distribution also developed (the drifting half-Maxwellian discussed above). As the sheath potentials increased, the energy of the beam component also increased. At the same time, the electron temperature about the interface between the PIC and fluid sectors also increased. Part of the

function of the sheath is to repel plasma electrons back into the plasma so that the current to the external circuit is kept at the prescribed value. As the plasma electron temperature grew, the sheath height had to grow in order to repel the hotter electrons. The increased sheath height led to higher beam velocities and plasma temperatures, and so a feedback mechanism was established.

This feedback mechanism can be understood by using a simple mathematical model of the interface between the PIC and Fluid sectors. Consider a Maxwellian plasma with temperature T in a PIC sector having an emitter as one boundary, and a fluid sector as the other. Let the emitter sheath be just high enough to reflect almost all of the plasma electrons back into the plasma. Let the emission electrons acquire a velocity v (directed towards the plasma) when passing through the sheath. To calculate the effective temperature to pass to the fluid side, the PIC sector uses Equation (61), expressing the average energy in the PIC sector as:

$$\bar{E} = (1-\alpha)\frac{3kT}{2} + \alpha\, mv^2 \qquad (67)$$

where α is the fraction of the total density in the beam, and v is the beam velocity. In this model, n is the total density at the PIC-FLUID interface, and αn is the beam component of the density. The drift velocity calculated over the whole (beam+Maxwellian) distribution is simply αv. The PIC sector assigns this value to the drift velocity and calculates an effective temperature (T') based on Equation (61) and the expression for the average energy:

$$T' = \frac{1}{3k}\left[(1-\alpha)(3kT + \alpha\, mv^2)\right] \tag{68}$$

This is an interesting expression. If the value of v is given by:

$$v = \sqrt{\frac{3kT}{m(1-\alpha)}} \tag{69}$$

the temperature returned is the original plasma temperature. As α approaches unity, v approaches infinity and T′ vanishes. In this limit the beam is a pure drifting Maxwellian with a temperature of zero. As α approaches 0, the beam energy approaches the average energy of the non-drifting Maxwellian distribution.

For values of the velocity greater than that given by Equation (69), the calculated effective temperature is greater than the original plasma temperature. For values less than that given by Equation (69) the effective temperature is less than the original. Let's start with a beam velocity greater than the value given in Equation (69). We step forward in time and calculate a temperature to pass to the Fluid sector. The temperature is greater than the original plasma temperature. The fluid sector returns a flux of particles into the PIC sector consistent with the temperature passed, and now the temperature in the Maxwellian portion of the PIC distribution has increased due to the hotter injection stream from the fluid sector. To repel the hotter electrons from the plasma, consistent with the constant current requirement, the sheath height has to increase. The larger sheath imparts a greater velocity to the emission electrons

passing through to the plasma. The higher beam velocity results in a still higher temperature to be passed to the fluid sector and the feedback cycle is complete.

Many complexities are absent in the simple feedback illustration above, but the basic mechanism described is accurate. Inelastic collisions (ionization in the fluid model) serve to limit the temperature rise, while elastic collisions in the PIC sector reduce the calculated drift velocity, transferring the energy gained by the emission electrons passing through the sheath from the x-component to the perpendicular component of their velocity vectors. In the limit of a PIC sector many mean-free paths thick, all the energy picked up from the beam goes to raise the temperature of the distribution and the feedback may actually be worsened.

The feedback cycle described above results from the fact that fluxes are not conserved across the interface when the distribution function in the PIC sector differs from that assumed for the fluid sector. While the particular feedback mechanisms arising from alternative formulations of the interface may vary, this is a fundamental limitation of the hybrid method. As will be demonstrated below, the only sure way to overcome this limitation is to formulate the distribution function at the interface and in the fluid sector with enough generality to closely match the observed distributions.

The failure to conserve fluxes can be illustrated by examining the relationship between the directed particle flux and the net particle flux across an

interface between a PIC and fluid sector. Let us assume that we have a steady-state, quiescent Maxwellian plasma with a beam component as described above, and let's represent the system at an interface between a PIC and a Fluid sector. The net flux across the interface is $nv\alpha$. The flux to the right and the flux to the left are:

$$\Phi_R = \alpha\, nv + \sqrt{\frac{kT}{2\pi\, m}}(1-\alpha)n \tag{70}$$

$$\Phi_L = -\sqrt{\frac{kT}{2\pi\, m}}(1-\alpha)n \tag{71}$$

respectively. Using the interface formalism, we cast the distribution as a Maxwellian with a temperature given by Equation (61), and a drift velocity of $v\alpha$. While the net flux and total energy using this formalism is conserved (for the moment), the flux to the left and flux to the right are now found using Equations (62) and (63), and will not in general be equal to those calculated using Equations (70) and (71). An example of the difference between the directed fluxes calculated using the interface algorithm is given in Table 6 for $n=10^{18}$ m^{-3}, T=3000 K, α=0.05 and a beam velocity 1.05 times the critical value given by Equation (69).

As can be seen in the Table, the directed flux to the left and right do not match before and after the distribution is recast as a Maxwellian, even though the net flux does match. The directed flux to the left (which is what the PIC-FLUID interface calculates and injects back into the PIC sector) is 6% less than

Table 6. Divergence in Directed Fluxes for a Beam-Plasma Velocity Distribution.

	Original	Final	% Difference
ϕ_R $(m^{-2}s^{-1})$	10.06816×10^{22}	9.55762×10^{22}	5.07
ϕ_L $(m^{-2}s^{-1})$	-8.07932×10^{22}	-7.56878×10^{22}	6.319
ϕ_{NET} $(m^{-2}s^{-1})$	1.98884×10^{22}	1.98884×10^{22}	0.0

what it would be if it were calculated using the correct distribution. This results in a decrease in the electron density in the PIC sector. Because the electrons are affected and respond more quickly to the changes in the sheath height than do the ions, this leads to a positive space charge buildup. Furthermore, because the directed flux into the fluid sector from the PIC sector has not changed, the new value calculated for the net flux will differ from the old, so that the net particle flux is not conserved in time. Similar statements can be made regarding the total energy, in that the directed flux into the PIC sector will have a different temperature from the initial distribution, so that the average energy of the particles in the PIC sector will have changed as well.

Alternative Interface Formulation.

The PIC-FLUID interface was designed to conserve all fluxes when the velocity distribution function at the interface was of the assumed form. When the distributions at the interface are not of the assumed form, nothing is truly conserved. The question has been raised as to whether a different formulation of

the interface would be able to properly represent the fluxes across the interface. Two alternatives to the interface formulation have been suggested. The first is to supply the directed flux of particles, energy and momentum into the fluid sector as boundary conditions to the fluid sector. The directed fluxes would be obtained directly from the particle distributions in the PIC sector, just outside the interface. The second suggestion is similar to the first: supply the *net* fluxes at the interface, rather than the directed fluxes. Both of these require a re-formulation of the fluid equations to accept the new boundary conditions, but other than that would not prove difficult to implement. In the limiting case of a plasma with pure drifting Maxwellian particle velocity distributions, these representations are equivalent to the existing implementation and would function equally well.

But what happens when the distribution in the PIC sector is non-Maxwellian? Do these alternative formulations still conserve all the relevant fluxes? To answer those questions requires an understanding of how the equations are formulated and how information is translated from the fluid sector to the PIC sector. Because the development of the fluid equations assumed Maxwellian velocity distributions, the equation of state for an ideal gas was used to close the system of equations. The ideal gas law was also used to characterize the thermal energy and pressure in terms of density and temperature. The density and temperature were related to the thermal energy density by a

numerical constant (Boltzmann's constant) that is strictly valid only for Maxwell-Boltzmann velocity distributions. The ionization, collision and energy transfer rates used in our equations all rely on an assumed form for the distribution function. The symmetry of the distribution allowed us to eliminate the heat flux vector, which must be included when an asymmetric distribution is used.

Because of these assumptions, if directed fluxes are provided as boundary conditions to the fluid sectors, the macroscopic quantities calculated in the fluid sector will evolve in time in exactly the same manner as if a density, temperature and drift velocity consistent with the directed fluxes were provided instead. In other words, an equivalent method for providing the exact energy, momentum and particle fluxes to the fluid equations would be to solve for the density, temperature and drift velocity that would give rise to the correct directed fluxes, and to provide those values instead.

The problem is that the density, temperature and drift velocity consistent with the directed fluxes (via the assumed form of the velocity distribution function) will not be consistent with the actual velocity distributions present in the PIC sector. While the directed fluxes into the fluid sector will match those leaving the PIC sector, the calculated fluxes back into the PIC sector will in general not match the actual directed fluxes into the PIC sector. For instance, if we take the previous example of a plasma with a beam electron component making up 5% of the total electron density (initial density of 10^{18} m-3, T=3000 K,

Vdrift = 0, α = 0.05, Vbeam =3.98x10^5 meter sec^{-1}) we can calculate the total energy, momentum and particle fluxes to the right (from the PIC sector into the fluid sector). If we then solve for an equivalent Maxwellian by varying the density, temperature and drift velocity to produce the same fluxes to the right, we get the velocity distribution function illustrated in Figure 27, and labeled "Directed Fluxes f(V)".

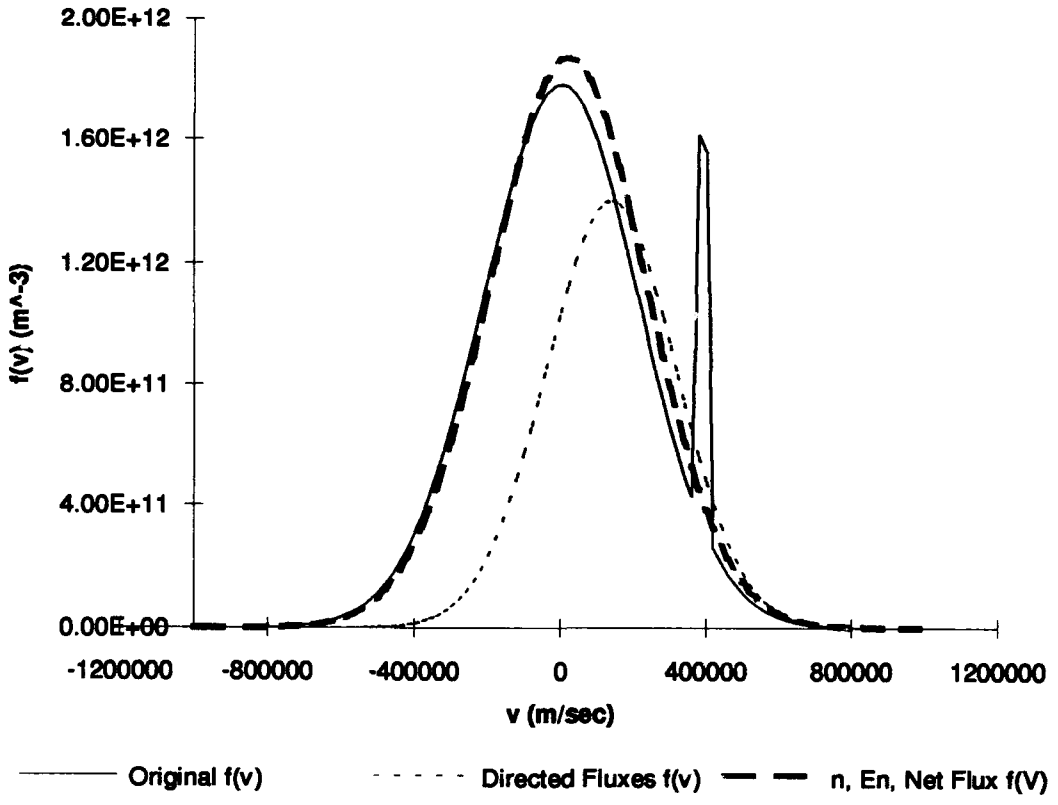

Figure 27. Comparison of Distribution Function Based on Directed Flux Matching to Our Implementation.

Also plotted in Figure 27 is a representation of the original distribution function and the distribution function that results from the application of our

interface algorithm (the trace labeled "n, En, Net Flux f(V)"). Note that in the original distribution, the beam component is actually a dirac delta function about the beam velocity. For the sake of visualization, it is given a finite width in the figure.

There are three "goodness of fit" considerations to use in evaluating the distribution functions produced: 1) how well do they reproduce the directed fluxes into the fluid region, 2) how well do they reproduce the directed fluxes back into the PIC region, and 3) how well do they conserve the net flux across the interface. Each of these considerations is equally important. The fluxes resulting from the conservation of directed fluxes into the fluid sector are compared to those of the original distribution function and to those arising from our implementation of the interface in Table 7. The column labeled Dir. Flux lists the fluxes based on conservation of directed fluxes, and the column labeled n,E,nv_d lists the fluxes from our implementation. As can be seen in the table, the original fluxes to the right are matched exactly by the fluxes based on conservation of directed fluxes, but the fluxes back to the left (representing what the fluid sector would calculate and send back into the PIC sector) are grossly inconsistent – 83%, 89% and 92% less than the original values for the particle, momentum and energy fluxes, respectively, resulting in increases in the net particle, momentum and energy fluxes across the interface of 335%, 241% and

Table 7. Non-Conservation at PIC-FLUID Interface -- 5% Beam.

Quantity	Original	Dir. Flux	% err	n,E,nv_d	%err
Vd (m/sec)	0	1.38×10^5	na	1.98×10^4	na
T (K)	3000	2103	na	3015	na
n (m^{-3})	10^{18}	6.27×10^{17}	-37	10^{18}	0.0
Flux Left ($m^{-2}\ s^{-1}$)	8.08×10^{22}	1.41×10^{22}	-83	7.57×10^{22}	-6.3
Flux Right ($m^{-2}\ s^{-1}$)	1.007×10^{23}	1.007×10^{23}	0	9.56×10^{22}	-5.1
Net Flux ($m^{-2}\ s^{-1}$)	1.989×10^{22}	8.66×10^{22}	+335	1.989×10^{22}	0
Momentum Flux Left (kg m s^{-1}($m^{-2}\ s^{-1}$))	1.966×10^{-2}	2.222×10^{-3}	-89	1.789×10^{-2}	-9.0
Momentum Flux Right (kg m s^{-1} ($m^{-2}\ s^{-1}$))	2.687×10^{-2}	2.687×10^{-2}	0	2.408×10^{-2}	-10
Net Momentum Flux (kg m s^{-1} ($m^{-2}\ s^{-1}$))	7.21×10^{-3}	2.464×10^{-2}	+241	6.19×10^{-3}	-14
Energy Flux Left (kg $m^2\ s^{-2}$ ($m^{-2}\ s^{-1}$))	3.345×10^3	2.552×10^2	-92	2.972×10^3	-11
Energy Flux Right (kg $m^2\ s^{-2}$ ($m^{-2}\ s^{-1}$))	4.778×10^3	4.778×10^3	0	4.217×10^3	-12
Net Energy Flux (kg $m^2\ s^{-2}$ ($m^{-2}\ s^{-1}$))	1.433×10^3	4.523×10^3	+216	1.245×10^3	-13

216%, respectively. By conserving the directed energy, momentum and particle fluxes, the net fluxes are not conserved.

The situation is somewhat better for the fluxes that arise from our implementation of the PIC-FLUID interface; the maximum error is a 14% underprediction in the net momentum flux. In terms of overall conservation of

both directed and net fluxes across the interface, our interface clearly outperforms an interface based on conservation of directed fluxes.

The comparison above shows that if the velocity distribution function in the PIC side of the interface is composed of a beam and a Maxwellian, the net fluxes across the interface are not conserved even when the directed fluxes are conserved. A similar argument can be made for the reverse. If the net fluxes are conserved, the directed fluxes will not be conserved. A similar comparison to that presented above was performed to calculate the density, temperature and drift velocity consistent with conservation of the net energy flux, particle flux, and momentum flux at the interface. The consistent values for the density, temperature and drift velocity were 9.6×10^{17} m^{-3}, 3472 K, and 2.1×10^{4} m s^{-1}, respectively. The directed fluxes back into the PIC sector were then calculated based on these values. The consistent values differed from the original directed particle, momentum and energy fluxes by -3%, -1% and +6% respectively, relative errors comparable to the implementation used in the hybrid code, and still not equal to the original directed fluxes.

Whether the discontinuities and feedback mechanisms using a flux-based interface would be less severe than with a net flux/total energy based interface is not known. But the inability to conserve energy, momentum and particle flux in both directions across a PIC-FLUID interface when the particle velocity distribution in the PIC sector cannot be adequately represented at the fluid

interface is a fundamental limitation of the system regardless of the formulation of the interface. If either the net fluxes or the directed fluxes are not adequately conserved across the interface, the densities and electric fields will become discontinuous across the interface, and the calculation will most likely diverge.

Recommendations to Make the Hybrid Model Robust.

In the validation calculations performed for the hybrid code, the hybrid model was stable and produced results consistent with full PIC calculations and with analytic expectations -- this in spite of the fact that the distributions in the PIC sectors adjacent to the fluid interfaces were never truly Maxwellian. Rather, the distributions at the interfaces were PIC representations and contained substantial statistical noise due to the finite number of particles in the simulation. The stability and consistency of the calculation under these conditions indicates that the assumed distribution function for the fluid sector and interface doesn't have to exactly match the actual distribution function in the PIC sector to have a stable and consistent calculation. In other words, there is such a thing as "close enough", although how close is close enough has not been determined. Based on the observed form of the velocity distribution function and the divergence of the converter calculations, the assumption of a single group Maxwellian distribution function together with our implementation of the interface is clearly not close enough. However, it may not be necessary to use

a full description of the distribution using a Maxwellian, a drifting half-Maxwellian and a spherical Maxwellian as suggested by the analysis above.

Instead, it's possible that a simple, two-group Maxwellian distribution function may be sufficient. For the example (discussed above) of a plasma containing both a beam and a Maxwellian distribution of electrons, a model based on a two group Maxwellian distribution function would correctly calculate both the directed and net fluxes, because a beam is, in the limit, a drifting Maxwellian with a temperature of zero. Such a formulation would allow for the transfer of energy via Coulomb collisions between the distribution groups across the entire inter-electrode gap, consistent with the calculated energy relaxation lengths of the injected electrons. The distribution of emission electrons in the converter at the sheath edge is not a true beam nor a drifting Maxwellian, but characterization as a drifting Maxwellian may be sufficient for a stable calculation, with the accuracy of the result to be determined.

Implementation of a two group distribution would involve two tasks: a reformulation of the fluid equations to include inter-group interactions, and a reformulation of the PIC-Fluid interface to extract the boundary condition information and inject a two-group distribution. The first of these two tasks is actually more difficult than the second, and will require careful analysis. The second is actually relatively simple. In the PIC method implemented in the hybrid code, particles are tracked by origin. Therefore, the emission electrons are a separate species from the plasma (or bulk) electrons. The plasma electrons

can be treated as one group (the bulk Maxwellian) and the emission electrons as the second, or "beam" group. Particles injected from the fluid interface into the PIC sector would have to be injected into their respective groups, either the bulk Maxwellian or the beam group, to provide the necessary back-flux for both distributions. Temperatures, densities and drift velocities can be calculated quickly for each group in the PIC sector using the same algorithm as in the current interface implementation. Determining the fluid groups based on the origin of the particles is supported by the detailed analysis of the distribution of particles in the sheaths presented above, and eliminates the need for a complicated and time-consuming algorithm for sorting the particles by energy and fitting a function to the particle distribution.

An analysis of the two-group method should be performed before it is implemented, following the same methods used to produce Table 7. The actual fluxes should be calculated using a Maxwellian and a 'drifting half-Maxwellian plus spherical Maxwellian' weighted sum of distribution functions. The 'drifting-half plus spherical' group should be recast as a full Maxwellian, then the fluxes recalculated and compared to the original. From the present work, we know that deviations on the order of 10% are unacceptable.

If the procedure outlined above doesn't produce acceptable results, the set of distribution functions could be enlarged to three, with one each to represent the bulk plasma electrons, the drifting half-Maxwellian emission electrons and

the spherical Maxwellian distribution. A flag could be added to the particles to indicate whether they have collided, and the uncollided portion of the emission species treated as one group, the collided portion as a second and the bulk plasma species as the third. Again, this procedure should be checked before implementation to determine the deviation from the original fluxes.

As a last resort, the fluid equations and interfaces could to be reformulated in terms of a weighted three-group distribution composed of a drifting half-Maxwellian, a drifting Maxwellian, and a spherical-Maxwellian (Equation 65). Such a formulation is consistent with the physics of the device being modeled and would provide 9 parameters (the weight, temperature, and drift (or offset) velocity for each distribution) which could be adjusted to reproduce any of the distributions observed computationally in a thermionic converter. The determination of the groups in the PIC sector could be made as for the three-group Maxwellian discussed above. Use of the actual distribution functions observed in the PIC sheath sectors is suggested as a last resort because substantial reformulation of the fluid equations would be required.

Because the distance traveled by electrons traversing the sheaths is so short with respect to thermalization by Coulomb collisions, the inability of the PIC technique to model Coulomb collisions is of little consequence. No changes to the PIC module are believed to be necessary, other than enabling the PIC-FLUID interface to inject particles consistent with the three group fluid model.

Conclusion.

In this chapter the application of the hybrid PIC-Fluid model to conditions typical of ignited mode thermionic converters was examined. Under ignited mode conditions, the electron velocity distribution function at the plasma-sheath boundary differed greatly from the form assumed in the development of the interfaces and fluid equations. Under these inconsistent boundary conditions, the current implementation of the hybrid model is incapable of correctly modeling the fluxes across the interface between the fluid and PIC sectors, and the calculations diverged. Analysis indicates that no modifications need to be made to the PIC module, but that the velocity distribution function used in the fluid equations and at the PIC-FLUID interface needs to be reformulated. A physically based set of distribution functions is a weighted sum of three related distribution functions: a drifting Maxwellian, a drifting half-Maxwellian, and a spherical-Maxwellian, but a simpler two or three group Maxwellian basis set may suffice.

V. Conclusion and Recommendations

In this work, a detailed collisionless sheath theory and a three-region collisional model of a bounded plasma was presented, and the suitability of the collisional model for ignited mode thermionic converters was investigated. The sheath theory extended previous analyses to regimes in which the sheath potential and electron temperatures are comparable in magnitude – as is the case for ignited mode thermionic converters. In all operating regimes typical of an ignited mode thermionic converter, the predicted sheath structures extend several mean-free paths into the inter-electrode space. The apparent collisionality of the sheaths prompted development of a collisional, three-region model of the converter plasma.

The need for a collisional approach to model the sheaths made a PIC treatment of a thermionic converter tempting, but the failure of the one dimensional PIC method to properly account for electron-electron collisions, difficulties representing multi-step ionization and three-body recombination, as well as the large numbers of particles that had to be tracked for statistical reasons, made the PIC method unacceptable in the bulk plasma. These considerations indicated that a hybrid approach, using PIC techniques in the sheaths, and fluid techniques in the bulk of the plasma, might be appropriate.

The hybrid model constructed assumed that the plasma at the PIC-Fluid interfaces had a velocity distribution closely approximated by the Maxwell-

Boltzmann distribution, and has the capability of modeling a device using any combination of PIC and fluid sectors, subject to the constraint that recombination and the multi-step ionization kinetics are not included in the PIC module. The computer code used to implement this model was written in C++ to run on a SUN SparcStation ® under OpenWindows ®, and employed a completely interactive graphical user interface. The user interface allows for selective representation of such diagnostics as the density, electric field and temperature both by species and by sector. It also allows the user to vary such simulation parameters as the particle weighting and external circuit current during the course of a calculation.

The implementation of the PIC algorithms was tested against bounded analytic calculations for an ideal diode with excellent agreement. The multiple-sector PIC implementation was cross-checked against the single-sector, again with excellent agreement. Finally, the fluid module was cross-checked against single and multi-sector PIC calculations, once again with excellent agreement.

When the hybrid PIC-Fluid model was applied to conditions typical of those found in an ignited mode thermionic converter, the electron velocity distribution function at the plasma-sheath boundary was found to differ greatly from the form assumed in the development of the interfaces and fluid equations. Under these inconsistent boundary conditions, the hybrid model was incapable of correctly modeling the fluxes across the interface between the fluid and PIC

sectors, and the calculations diverged. Analysis indicates that no modifications need to be made to the PIC module, but that the velocity distribution function used in the fluid equations and at the PIC-FLUID interface needs to be reformulated. There is reason to believe that an exact match of the distribution function in the PIC sector is not necessary, and it is possible that a weighted sum of two or three Maxwellians may comprise a sufficiently close approximation. If not, a weighted sum of three related distribution functions: a drifting Maxwellian, a drifting Half-Maxwellian, and a spherical-Maxwellian comprise a physically justified basis set for use in reformulating the fluid equations. With a corrected fluid module and interface, the hybrid code should be fully capable of modeling high-pressure, ignited mode thermionic converters.

Recommendations for Future Work

The hybrid multi-sector PIC Fluid code developed in this work suggests a number of possibilities for future study. The first is to correct the fluid model and develop a new PIC-FLUID interface consistent with the new model. When operated in the hybrid mode, the code was able to perform a stable simulation of a "Maxwellian" plasma, even though the distributions in the PIC sectors were only approximations to Maxwellians, and had substantial statistical noise. This implies that the representation of the distributions at the interface have to only

approximate the actual distribution functions in order to achieve meaningful results. What is unknown is how close that approximation has to be.

These observations suggest that a simple two or three-group Maxwellian distribution function, rather than the more complicated observed three group distribution function, may be able to satisfy the interface requirements. A two or three group Maxwellian representation would be much simpler to implement than the full observed distribution due to the simplicity of the Maxwellian distribution. Because the PIC code already tracks species by their origin, one (or two) group(s) could be used for particles emitted from the electrode and the remaining group for particles emitted from the plasma. Thus, no complicated fitting or stripping of the distribution function would be required.

If both the two and three group Maxwellian models prove insufficient for modeling the ignited mode thermionic converter, the next attempt should be a three-group model using the distributions observed in the PIC sheaths at the interface. The isolation of the components by species origin (emitter or plasma) could still be used to avoid having to strip or fit the distribution function in the PIC region.

Reformulating the fluid model remains the most difficult task, but the result should be a very useful tool for examining the behavior of not only thermionic converters across their entire realm of operation, but of all plasma devices in which the sheath structures are not well known.

A second area of future work is the inclusion of variance reduction techniques (32:331-338) into the multi-sector PIC implementation. It should be possible to specify importances for each sector and then apply Russian roulette and splitting techniques (commonly used in neutron transport codes (32:333)) at the interfaces between the sectors. Such an implementation is necessary to be able to fully reap the benefits of variable grid spacing provided by the multi-sector approach, as it allows for increased numbers of particles in the sectors with fine spatial meshes and for fewer numbers of particles in sectors with coarser meshes.

Implementation of Russian roulette and splitting is greatly simplified by the PIC-PIC interface design. When particles pass from one sector to another, they are given to the interfaces and their velocities and positions are rescaled before they are passed to their new sector. Splitting a single particle into two particles and staggering their injection slightly could be handled quite neatly as the particle crossed the interface. Similarly, particles passing to a region of lower importance could be accumulated and combined to give appropriate flux across the interface. Care would have to be taken to address conservation of momentum, charge and energy in developing the splitting and recombination algorithms.

Once a working hybrid model is developed, a third area of work will have to do with the run-times of the model and determination of convergence. The fluid and PIC techniques used in this analysis are limited to time-steps of a

picosecond. An average cesium ion in a distribution with a temperature of about 1300 K has a velocity of about 300 m sec^{-1}. The inter-electrode gap is typically $5x10^{-4}$ meters across, so the average ion transit time is just under 2 microseconds. Thus, at a picosecond time-step, just under 2 million time-steps are required for an ion to cross the inter-electrode gap (barring collisions). The fastest hybrid calculations on a Sparc-10 using 5,000-10,000 particles in the PIC sectors have required about 0.5 real seconds per computational time-step. At that rate, a calculation which runs long enough for a cesium ion to cross from electrode to electrode would take about 9 days.

In fact, the actual run-time of a calculation to steady state, given a good starting point, may be less than the ion-transit time, but one would still like to run to several ion transit times to ensure a steady state has been achieved. That would take a month, given the current state of the code. The code is not optimized and a number of diagnostic values are calculated at every time-step for every particle, so quite a bit of optimization may be possible. Further analysis of the fluid equations and elimination of negligible terms may also speed up the calculation. The Sparc-10 was selected as the computational platform because it has a multi-processor capability; the multi-sector nature of the hybrid model lends itself to a parallel-processor implementation, which would also serve to decrease the time necessary for a calculation.

Once a working hybrid model is developed, serious consideration should be given to extending the model to two dimensions to examine the possibility of contraction of the discharge in the obstructed regime -- not possible with a one dimensional calculation. A two dimensional calculation could also examine such issues as the effects of patchyness of the emitter work function and the 'anomalous' Schottky effect.

To generalize the code, options should be added for other ionization kinetic schemes. Currently the ionization kinetics in the fluid module are specifically for cesium.

Appendix A: Discontinuities in the Multi-Sector Approach

Particle in Cell (PIC) techniques compute and follow the actual motion of representative particles as they move through the space being modeled. As such, the fundamental data produced by a PIC calculation is simply a list of representative particles, their positions and velocities. The user, however, is usually concerned with more macroscopic quantities such as the density of electrons and ions, the associated net charge density, the electric fields, potential and current through the device. To arrive at these macroscopic quantities, a technique is needed to transform the discrete nature of the fundamental PIC data into the desired form.

In the PIC approach used in this work, that technique involves the use of a cellular discretization of space using a major and minor grid structure. Essentially, the space being modeled is divided into sectors and each sector is divided into cells. Each sector uses a consistent cell width, although the cell width can vary from sector to sector. This discretization is illustrated for a single sector in Figure 28.

Each sector begins with a major grid-point at the boundary, with subsequent major grid-points located at intervals of a cell width across the sector, terminating with a major grid-point at the far boundary. The major grid-points are defined as being located at the cell centers; thus the cells

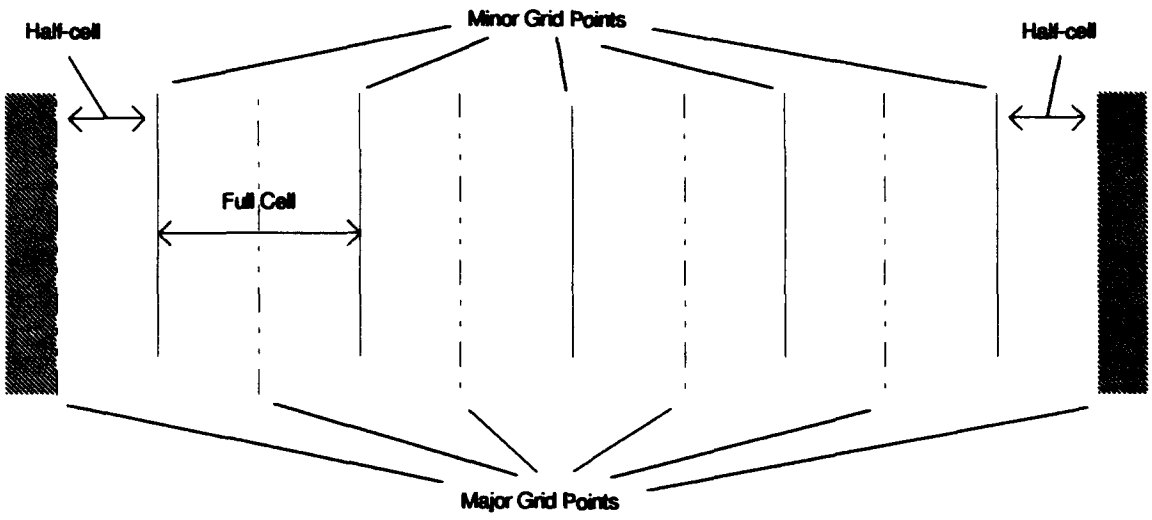

Figure 28. Spatial Discretization Using Major and Minor Grid Points.

corresponding to the first and last grid-points (those located on the boundaries) are actually bisected by the boundaries so that half their volume lies outside the boundary. The half of these cells within the boundary are called 'half-cells'.

The multi-sector approach implemented uses the same major/minor grid-point meshing as used in the single sector calculation. In a single sector calculation, the particle values (such as density) are weighted to a grid using the linear weighting scheme discussed in Birdsall (4:21). Under this scheme, particle values are linearly weighted based on the distance to the nearest two major grid-points, and the weighted values assigned to the two nearest grid-points. For example, if a particle was one-fifth of the way between grid-point A and grid-point B, the nearer grid-point would receive four-fifths of the particle value and the farther grid-point one-fifth of the particle value. At grid-points away from a boundary, macroscopic quantities (such as the charge density, particle density,

drift velocity, average energy, temperature, and average path length) receive contributions from all particles within the distance of a full cell width on either side of the grid-point.

At the boundary, however, only particles on one side of the grid-point (the side away from the boundary) can contribute to the accumulated value at the grid-point, because the positions of the particles beyond the boundary are unknown. This leads to a calculated values at the boundary grid-points that are half of what would be calculated at an internal grid-point given a uniform density. To correct for this error, the accumulated values at the boundary grid-points are doubled to produce a 'one-sided' estimate of the true value at the boundary(4:410).

This one-sided estimate will in general not match the value calculated if particles from both sides of the interface were used in the estimate -- nor will the one-sided estimate calculated on one side of a boundary match the estimate calculated on the other -- resulting in a discontinuity in the calculated value at the interface. This is particularly noticeable in the presence of strong gradients in the quantities being estimated, as illustrated in Figure 29.

While a discontinuity in such quantities as the particle density is disquieting, the discontinuity is an artifact of the boundary and does not affect the motion of the particles in a PIC simulation. At a PIC-FLUID boundary, however, the density at a major grid-point has to be provided as a boundary

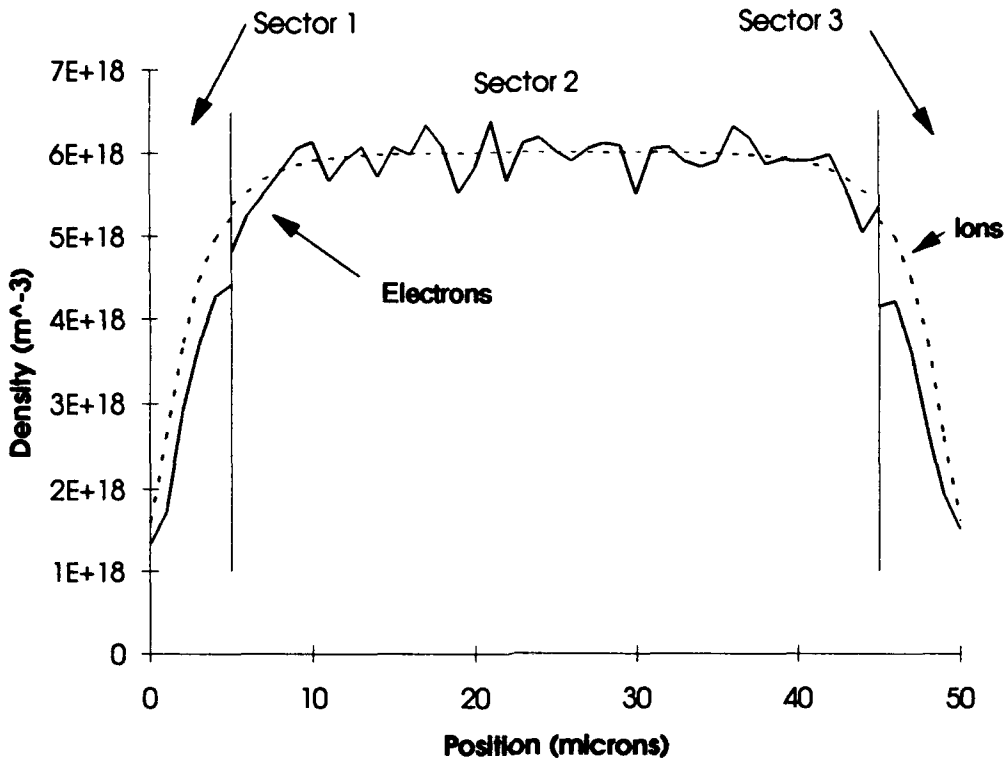

Figure 29. Discontinuity in Electron and Ion Densities at Interfaces.

condition to the fluid calculation. The fact that value of the density is less well known at the boundary than at the first major grid-point inside the PIC sector led us to use the better known value as a boundary condition to an adjacent fluid sector, rather than the value calculated by the PIC sector at the boundary grid-point.

While the discontinuity of the density across a PIC-PIC interface is of no direct consequence, it leads to a discontinuity in the charge density at the interface that *is* of concern because the electric field (calculated from the charge density) directly affects the motion of the particles in the simulation. In practice,

however, the results of such a discontinuity are also negligible, as demonstrated in Figure 30, in which the electric field consistent with the density profile presented in Figure 29 is plotted.

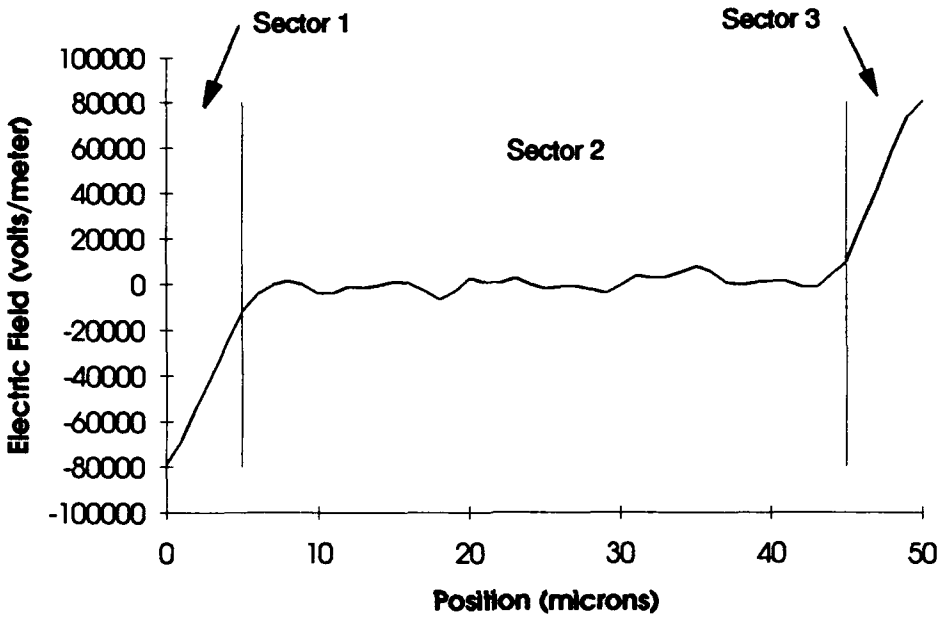

Figure 30. The Electric Field in the Presence of Discontinuities in the Charge Density.

To understand the influence of the discontinuity in the charge density on the electric field, it is helpful to briefly review the nature of the one dimensional electric field and how it is calculated in the PIC technique.

In one dimension, the electric field due to an infinite sheet of charge is constant in a direction perpendicular to that sheet of charge, and equal but opposite on either side of the sheet. Thus, if a moving sheet of charge passes a point in space, the field jumps from a minimum to a maximum value

discontinuously as the sheet passes. This results in a very noisy electric field, with the noise in the field tied to the motion of particle sheets (or superparticles) past the observation point.

To reduce the noise in PIC implementations, the superparticle sheets of charge are typically treated as clouds of charge instead of infinitesimally thin sheets, and their contribution to the local charge density linearly weighted to the two nearest grid-points. With this approach, the charge density, and therefore the electric field, varies relatively smoothly as superparticles move through the region two cells wide about an observation grid-point.

Further smoothing of the noise in the electric field from the motion of superparticles can be obtained by extending further the range over which they can affect the field at a point, essentially making their influence broader and field variations due to particle motion more gradual. This is done by calculating the electric field at the right boundary of each cell due to the charge density in and to the left of the cell, and then calculating the potential at the center of the cell based on the electric field at the right cell boundary and the potential at the center of the next cell to the right. The field at the midpoint of each cell is then calculated using a central finite difference technique and the potential at the middle of the two adjacent cells. Figure 31 illustrates the calculation of the electric field using this method.

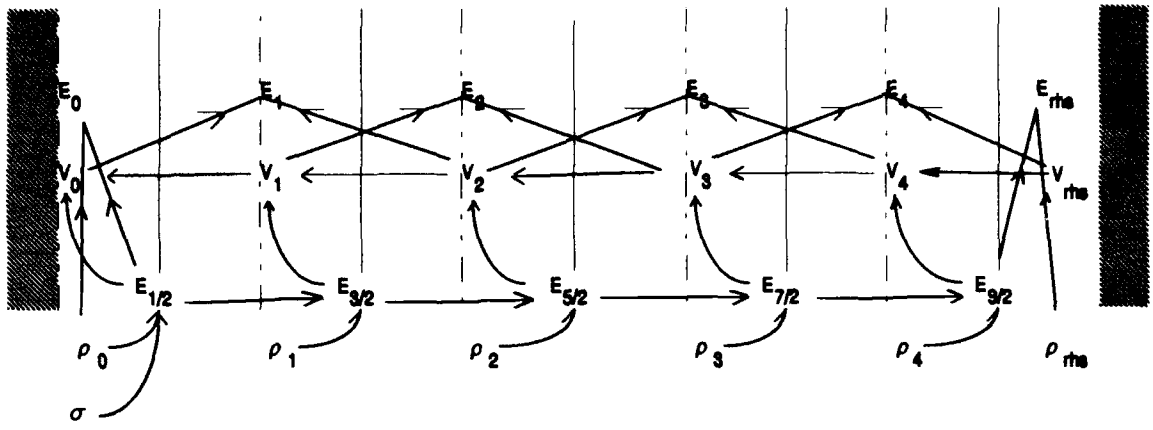

Figure 31. PIC Calculation of Electric Field.

The arrows in the figure indicate a contribution from the calculated quantity at their tails to the quantity at their tips. For example, σ (the surface charge density at the left wall) and ρ_0 (the average density calculated at the left wall) contribute to the calculation of the electric field at the edge of the first half-cell ($E_{1/2}$). $E_{1/2}$ and the charge density in the first full cell contribute to the calculation of the electric field at the right edge of the first full cell ($E_{3/2}$). Once all the electric fields at the cell boundaries are calculated, the potential at the right wall and the electric field at the right boundary of the fourth cell are used to calculate the potential at the center of the fourth cell. Once all the potentials are calculated, the zeroth and the second potential are used to calculate the field at the first grid point, and so on. Finally, the electric field at the walls is calculated, effectively using the fields at the first half-cell boundaries away from the wall and the charge density calculated at the walls.

Figure 32 demonstrates how this scheme smoothes the discontinuity in the field arising from the motion of a superparticle past a given grid-point by extending the superparticle's range of influence over a distance of four cell widths about the grid-point. A particle just to the left of grid-point four can contribute to the charge density at grid-point three, which in turn is used to calculate the electric field at the minor grid-point between major grid-points three and four. That value of the field is used to calculate the potential at grid-point three, which is used along with the potential at grid-point one to calculate the electric field at grid-point two.

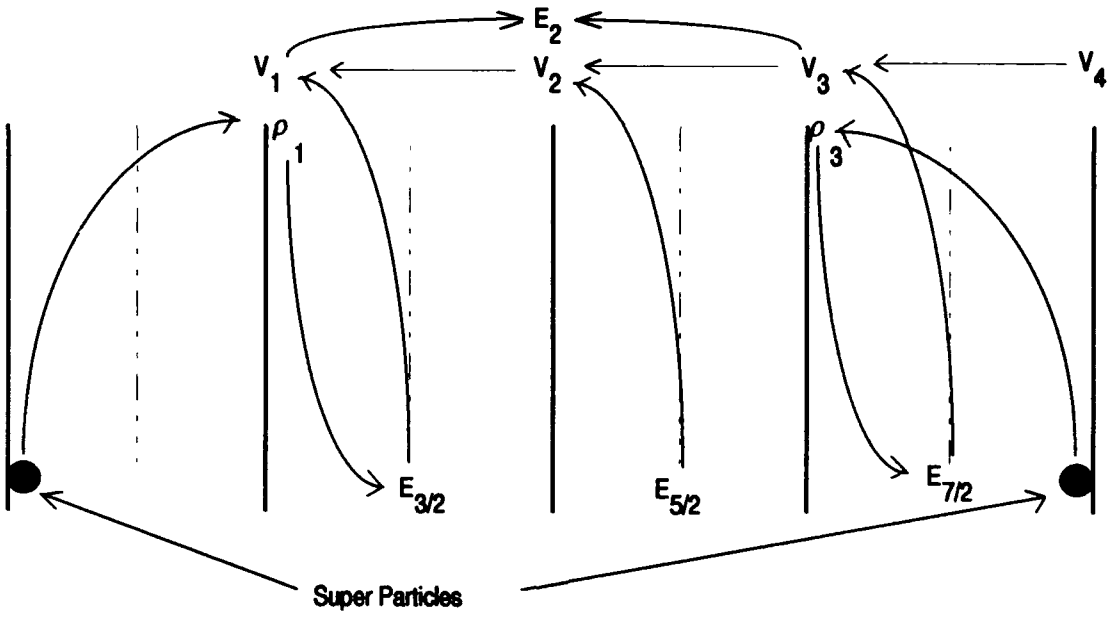

Figure 32. Range of Influence of Superparticle Motion on Calculated Value of Electric Field.

As the test particle moves toward grid-point three, the charge density there increases, thus increasing the field at the grid-point between major grid-points three and four, directly affecting the value of the potential at grid-point three and the electric field calculated at grid-point two. Thus, the movement of a test charge can influence the value of the electric field as soon as the particle is two cells away from a grid point.

The discontinuities introduced at the interfaces between PIC sectors influence the calculation of the electric field in two ways. First, the value of the electric field at an interface will differ slightly from that calculated when the interface is absent -- in fact, the calculated field will be more spatially accurate with the interface than without. The second effect is related to the first -- the increased accuracy comes at the cost of a slight loss of precision and a slight increase in noise.

The first effect, the shift in value of the electric field, can be explained as follows. The charge density calculated at an internal grid-point in a sector is a weighted average value taken across the two cells on either side of the grid-point. If the charge density varies asymmetrically across those two cells, a value calculated over the left half only will not equal a value calculated over the right half. In the absence of the interface, the field at the interface would be determined by the total charge density to the left of the half cell to the left of the interface ($\varepsilon_0 E_{3/2}$ in Figure 32 if the interface were placed at grid-point 2) plus half

of the average value of the charge density in the half cells on both sides of the interface (ρ_2). In the presence of the interface, the field is determined by the total charge density to the left of the half cell to the left of the interface ($\varepsilon_0 E_{3/2}$ again) plus the one sided estimate for the charge density in the left half of cell bisected by the interface, that is, the left half of the cell with major grid-point 2 at its center. Both sides of the interface will agree to this value for the field , but if the charge density in the one sided estimate for the left half of cell 2 doesn't equal the value of the charge density calculated in the absence of the interface (ρ_2), the resultant field will not match that calculated in the absence of the interface. The calculated field will be more accurate with respect to the positions of the particles in the simulation because it will reflect the total charge density to the left of the interface without any influence from particles to the right of the interface, which is the strict definition of a one dimensional electric field.

The second effect (the loss of precision and increase in noise in the electric field) arises from two sources. The first is simply that a smaller volume, hence a smaller number of particles, is being used to calculate the density in the half-cells on either side of the interface than in the absence of the interface. This leads to poorer statistics. The second cause arises from the weighting process for the charge density. In the absence of the interface, particles approaching the interface grid-point begin to affect the electric field there when they are within 2

cell widths of the grid-point in either direction. Thus, their effect is spread out over 4 cell widths. As a particle moves across the grid-point from left to right, a portion of its charge is effectively moving to the right of the grid-point as soon as the particle is within 2 cell widths of that point. The effective rate at which the charge is moving past the grid-point reaches its maximum when the superparticle is at the grid-point, and tapers off again as the super particles moves to the right, vanishing when the super particle is 2 cell widths past the grid-point. With the interface, the effect of a particle crossing the interface from the left to the right on the electric field is very different. As long as the particle is to the left of the interface, the full effect of its charge is felt to the right. Only when the super particle moves past the interface does its influence begin to be smoothed. On injection its full weight comes off of the charge density to the left, and then is distributed between the first two grid points. The particle contributes to the charge density at the first grid-point away from the boundary, and thus to the electric field at the boundary, until it is 2 cell widths away from the boundary. The reverse is true for particles moving from right to left across the interface. Thus, only half of the smoothing effect obtained using central differences to calculate the electric field at major grid-points is achieved, and the result is increased fluctuations in the electric field due to single and multiple particle crossings of the interface -- slightly more noise.

In a typical calculation, the effect of the additional noise on the electric field is not noticeable. The most noticeable effect on the field is a kink in the field at the interface between PIC sectors that occurs when the charge density on either side of the interface disagree. Typical kinks in the field can be seen at the sector boundaries in Figure 30 (presented previously) and in Figure 33, which is a plot of the instantaneous electric field in a three sector PIC calculation for a quiescent plasma with an electron temperature of 1800 K and an ion temperature of 973 K.

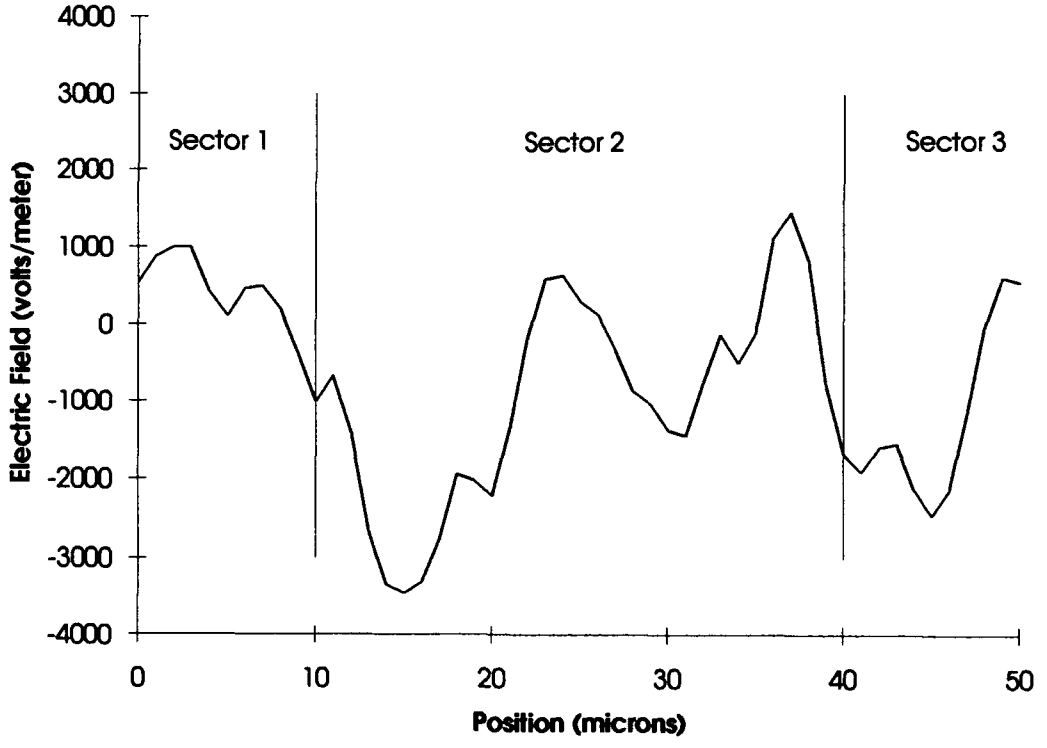

Figure 33. Kink in Electric Field Arising From Discontinuity in the Charge Density at an Interface.

The noise in the field (for which the time averaged value vanishes) is comparable to that in a single sector PIC calculation, and the perturbation due to the discontinuity at the interface is much less than the simple noise in the calculation.

Appendix B: Correction to the Injection Velocity Adjustment Scheme Used in PDP1

The algorithms developed by Birdsall et al. use a leap-frog technique to advance the velocity and the particle positions(4:13). At some time t, the electric field is calculated based on the particle positions, and the velocity of each particle is updated from what it was known to be at t-½ to a new value at t+½. The particle is then moved in space from its position at time t to a new position at time t+1 using the velocity at t+½, treated as uniform from t to t+1. The difficulty is that the particles are injected from the walls at times uniformly distributed between t and t+1. To blend in with the velocity update scheme, their velocities and final positions in the simulation must be adjusted for the electric field present just outside the emitting surface, then their velocities must be again adjusted so that at the next application of the acceleration, which assumes a full time-step under the influence of the electric field, the velocities will be correctly accelerated.

In the PDP1 code, injection particles are assumed to have entered the simulation uniformly at time intervals of dt/(n+1), where n is the number of particles to be injected during the time-step and dt is the length of the time-step. The time they are in the simulation and the acceleration they experience is calculated, and the velocity is chosen to be consistent with the emission temperature and drift velocity. This is all correct. The error comes in the adjustment of the velocity for

the acceleration due to the electric field. In PDP1, this adjustment is made by multiplying the acceleration by del_t-.5 (where del_t is the normalized time in the simulation and ranges from 1/(n+1) to n/(n+1)) and adding the result to the normalized velocity: v = v+ a * (del_t-.5). The new position is then calculated as: x = del_t * v. That this is incorrect can be seen by considering the case in which a positive acceleration exists at the emitter and a particle is injected with minuscule initial velocity during the first half of the time-step (del_t<0.5). The above scheme will assign the particle position with a negative value, that is, outside the simulation, when it should have been accelerated into the first cell. Instead it will be eliminated as having moved outside the system.

The correct scheme can be deduced by re-examining the update sequence and considering how the injection timing fits in with the normal update timing. The timing of the leap-frog scheme is illustrated in Figure 34. In the normal

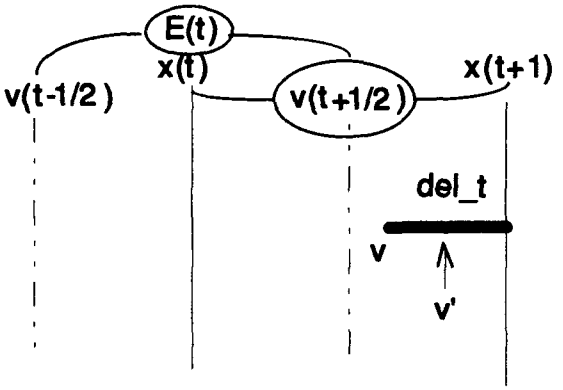

Figure 34. PIC Leap-Frog Scheme.

sequence, the electric field calculated at time t is assumed to be constant from t-1/2 to t+1/2 and the particle velocity is adjusted for the acceleration the

particle experiences under that field over a complete time-step to v(t+1/2). This velocity is assumed to be constant over the time interval from t to t+1, and the particle position is updated using v(t+1/2) over the complete time-step from t to t+1. On injection, the particle position and velocity are not known at t-1/2, but at t+1-del_t. For consistency, then, the velocity of the particle must be accelerated through half the time the particle will be moved, that is, to t+1-del_t/2, and then that velocity used to move the particle through del_t to t+1: v'= v'+ a * (del_t/2); x = v'*del_t. We're not done, though, because v' is not at t+1/2, but at t+1-del_t/2. At the next time-step, v will be accelerated a full time-step from t+1/2 to t+3/2, so v' must be consistently be backed up in time to t+1/2. This is done by accelerating through -(1-del_t)/2 so that v = v - a *(0.5*(1-del_t)).

This scheme was implemented in the PIC module, and tested using the analytic results for an ideal diode. Using Equation (1), the potential barrier across an ideal diode can be calculated as:

$$V = -\frac{kT_E}{e}\ln\left(\frac{J}{J_E}\right) \qquad (72)$$

where J_E is the emission current density, T_E is the emitter temperature, k is Boltzmann's constant, e is the magnitude of the charge on an electron and J is the current density delivered to the anode. Using a ratio of J/J_E of ½, V is found to be 0.0597335 volts. In a PIC calculation using a gap of $\frac{1}{3}$ x10^{-8} m, 10 cells, T_E of

1000 K, and a time-step of 4.0×10^{-15} sec, the potential calculated using the PDP1 procedure differed from the analytic result of 0.08% while the value calculated using the new procedure differed by only 0.009%. While this result shows almost an order of magnitude improvement, the previous result was actually quite good already; but this may not always be the case.

Appendix C: An Expression for the Height of the Space Charge Barrier in a Closely Spaced Thermionic Converter

The Langmuir-Childs law was derived for a powered diode, under conditions of an applied potential across the device. In the absence of an applied potential, an alternative derivation results in the same formula and more clearly displays the relationship between the potential in the formula and the space charge. Assume we have a current density of monoenergetic electrons with just enough initial energy E_d to overcome their own space charge when traveling from point 'd' to point '0' (see Figure 35) where the value of the potential V is given by $-V_0$.

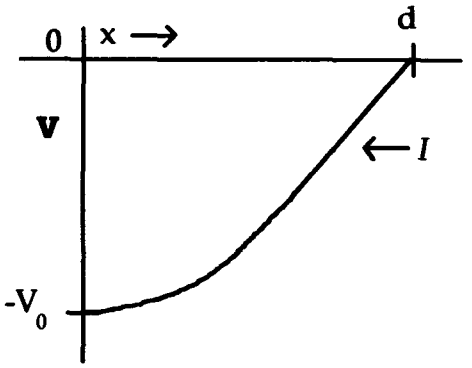

Figure 35. Space Charge Potential Diagram for Stagnating Monoenergetic Electron Beam.

Following Langmuir (27:9-10), the velocity of the electrons at a point in the space charge region can be found from an energy balance given by:

$$\frac{1}{2}mv^2 = E_d + eV \tag{73}$$

where m is the particle mass, v the velocity, e the elementary charge, E_d the initial energy of the electrons and V the potential. Using the definition of the current density, $I=v\rho$, the charge density (ρ) is found to be:

$$\rho = \frac{-I}{\sqrt{\frac{2}{m}(E_d + eV)}} \tag{74}$$

Laplace's equation becomes (in electrostatic units for consistency with Langmuir):

$$\frac{d^2V}{dx^2} = -4\pi\rho = 2\pi I\sqrt{\frac{2m}{E_d + eV}} \tag{75}$$

Multiplying by $2V\,dV/dx$ and integrating yields:

$$\left(\frac{dV}{dx}\right)_x^2 - \left(\frac{dV}{dx}\right)_0^2 = 8\pi I\frac{\sqrt{2m}}{e}\left[\sqrt{E_d + eV} - \sqrt{E_d - eV_0}\right] \tag{76}$$

By definition, E_d is equal to eV_0, and, because the current stagnates at x=0, the electric field vanishes there. Inserting these values and taking the square root of both sides, we arrive at:

$$\frac{dV}{dx} = \sqrt{8\pi I\frac{\sqrt{2m}}{e}\left[\sqrt{E_d + eV}\right]} \tag{77}$$

Integrating this expression from x=0 to x=d leaves us with:

$$\frac{4}{3}\frac{E_d^{3/4}}{e} = \sqrt{\frac{8\pi I}{e}}\sqrt[4]{2m}\,d \tag{78}$$

Rearranging, and substituting eV_0 for E_d gives the Langmuir-Childs relation:

$$I = \left(\frac{\sqrt{2}}{9\pi}\sqrt{\frac{e}{m}}\right)\frac{V_0^{3/2}}{d^2} \tag{79}$$

where the potential V_0 is the space charge that arises when a current density I crosses a gap of thickness d with just enough initial energy to overcome the self-induced space charge. Solving for the space charge yields:

$$V_0 = \left(\frac{9\pi I}{\sqrt{2}}\sqrt{\frac{m}{e}}\right)^{2/3} d^{4/3} \tag{80}$$

Equation (80) represents an upper bound on the potential arising from the space charge because the electrons injected have only the amount of energy necessary to overcome the space charge. If the injection electrons had a greater initial energy, the density, and therefore the space charge, would be lower.

A smaller bound for the space charge in a closely spaced thermionic converter can be obtained as follows. Consider a fixed current density, I, injected from the emitter as above, with just enough energy to overcome the space charge. If a potential minimum exists in the inter-electrode space, as illustrated in Figure 36, any electrons that have enough energy to cross the minimum will cross and be accelerated to the anode. Thus, the value of the potential at the minimum determines the initial energy the electrons must have to be able to cross the inter-electrode space. Equation (80) can still be used to calculate the potential at the minimum, but the distance d, which was the spacing of the gap, is now replaced with the distance to the minimum.

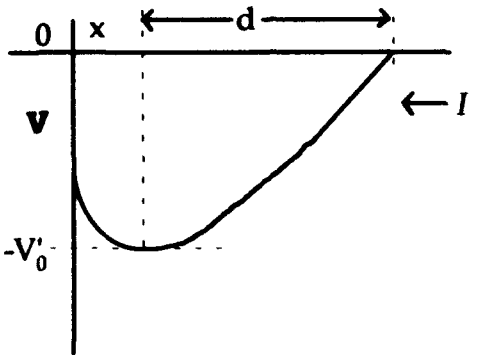

Figure 36. Space Charge Potential Diagram with a Potential Minimum.

It is easy to see from Equation (80) that as the distance d is decreased, the space charge potential grows smaller, vanishing in the limit as d vanishes. But, physically, d cannot vanish. As the location of the minimum moves towards the emitter, a potential rise develops on the anode side of the minimum. The electrons that make it through the minimum are accelerated in this region until they reach the wall. The conditions of the region to the left of the minimum are exactly those for which Langmuir developed his space charge equation: electrons with no initial velocity, accelerated by a positive potential from a region where the electric field vanishes. Thus, the Langmuir-Childs equation, with the current density equal to the injection current density, predicts the value of the potential rise to the anode. As the location of the potential minimum is shifted to the center of the inter-electrode space, the magnitude of the potential rise to the anode approaches the magnitude of the potential minimum, becoming equal when the minimum occurs at the middle of the gap. If the minimum is shifted any further toward the emitter, the potential rise to the anode would

exceed the potential drop from the cathode. Thus, the anode would be positive with respect to the cathode, as can only happen if power is applied to the device, or if the anode work function is less than the cathode work function.

Thus, given equal work functions, the smallest achievable space charge potential occurs when the minimum is at the middle of the inter-electrode gap. We can calculate the value of V_0' (the smaller bound on the space charge potential) for a given current density and gap, by replacing d in Equation (80) with d/2:

$$V_0' = \left(\frac{9\pi I}{\sqrt{2}}\sqrt{\frac{m}{e}}\right)^{2/3}\left(\frac{d}{2}\right)^{4/3} = 2^{-4/3}V_0 \qquad (81)$$

This limit is $2^{-4/3}$ of the upper bound, or 0.3968 times the space charge calculated by Langmuir's analysis.

There is, however, an accelerating potential available in the gap of an un-powered thermionic converter. As already mentioned, when the anode work function is less than the cathode work function, an accelerating potential equal to the difference between the work functions exists in the inter-electrode space, typically on the order of a volt. In this case, we can take the limit of Equation (80) as d vanishes, and find that the initial energy of the electrons vanishes, and the space charge limited current density from the cathode is given precisely by the Langmuir-Childs law, with the difference between the work functions used for the applied voltage.

Appendix D: Velocity Space Transform for Elastic Scattering

Assume we have a particle moving with velocity vector V that scatters to new velocity V′, as illustrated in Figure 37. We would like to be able to model forward biased scatter, and so need to calculate the scattering angles in the particle frame of reference and then transform the new velocity vector into the laboratory frame of reference. The equations needed to effect this transform are developed in this appendix.

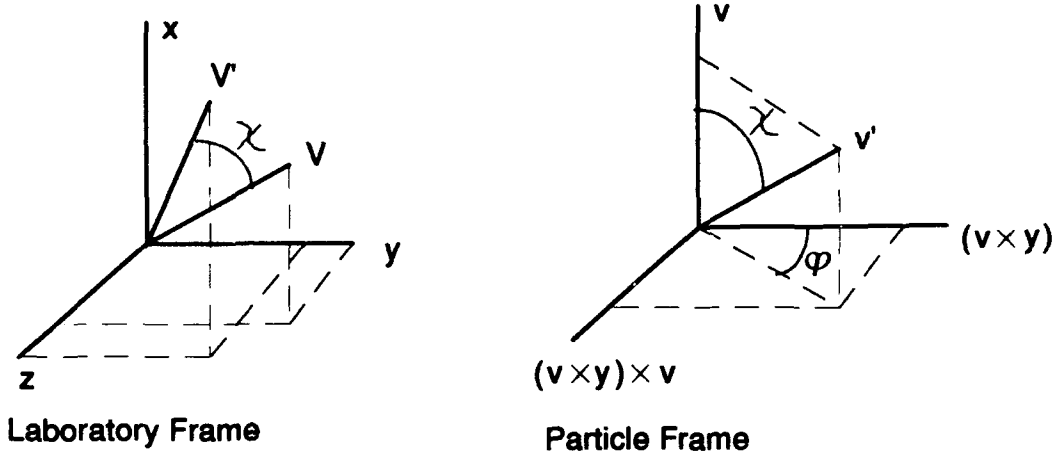

Figure 37. Elastic Scatter Coordinate Frames.

To help understand the transformation, we begin by defining our symbols. Un-primed symbols represent values before scattering, and primed symbols the values after the scatter. Lower case symbols represent vectors normalized by the magnitude of the velocity vector, while upper case symbols

are the un-normalized values. The angle χ is the angle between the new and the old velocity vectors. The angle φ is the angle through which the new velocity vector is rotated about the axis of the old velocity vector, measured from the vector defined by the cross product of the original velocity vector and the y axis.

To transform the new velocity vector from the particle frame back to the laboratory frame, we will adopt the transformation formalism of Goldstein to produce a transformation matrix conforming to a rotation about the z-axis, followed by a rotation about the shifted x axis, and a final rotation about the shifted z axis(15:143-148). To use this formalism, we must determine the proper rotations and sequences. To help to visualize the process, a superposition of the particle frame axes on the laboratory frame axes, together with the normalized vectors and the angles separating them is presented in Figure 38.

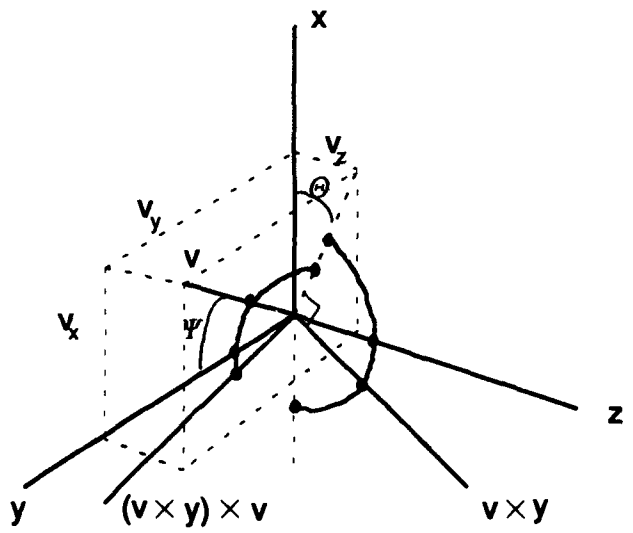

Figure 38. Particle Frame Superimposed on Laboratory Frame.

We'll need to analyze this geometry a bit to determine the rotations we want and the relationship between the rotation angles and the coplanar vectors. All the vectors diagrammed pass through the origin. The vector vxy is perpendicular to both v and y. Because it is perpendicular to y and passes through the origin, it lies in the xz plane, as signified by the curved line and the dots that ties vxy to x and z in Figure 38.

The plane containing v and y is perpendicular to vxy by definition of the cross product. Because y is perpendicular to the xz plane, the vy plane is perpendicular to the xz plane. Because (vxy)xv is perpendicular to vxy, it, too, must lie in the vy plane. Because the vy plane contains v and the origin, and is perpendicular to the xz plane, the line passing through the origin and the point $(v_x,0,v_z)$ -- the projection of v on the xz plane -- is also in the vy plane. Because the vy plane is perpendicular to vxy, and contains the projection of v on the xz plane, that projection is perpendicular to vxy. Therefore, the angle given by $\cos(\Theta) = v_x (v_x^2+v_z^2)^{-1/2}$ is the angle between the z axis and vxy, and $\sin(\Theta) = v_z (v_x^2+v_z^2)^{-1/2}$. The angle Ψ that v makes with the y axis is given by $\cos(\Psi) = v_y$, and $\sin(\Psi)=(v_x^2+v_z^2)^{1/2}$. Now we have everything we need to perform our rotations and construct our transform.

The rotation sequence is presented in Figure 39. For convenience, and so that our axes agree with those used in Goldstein's transformation, we'll orient our drawings with the z axis vertical. Recall that z, vxy, and x are coplanar, and

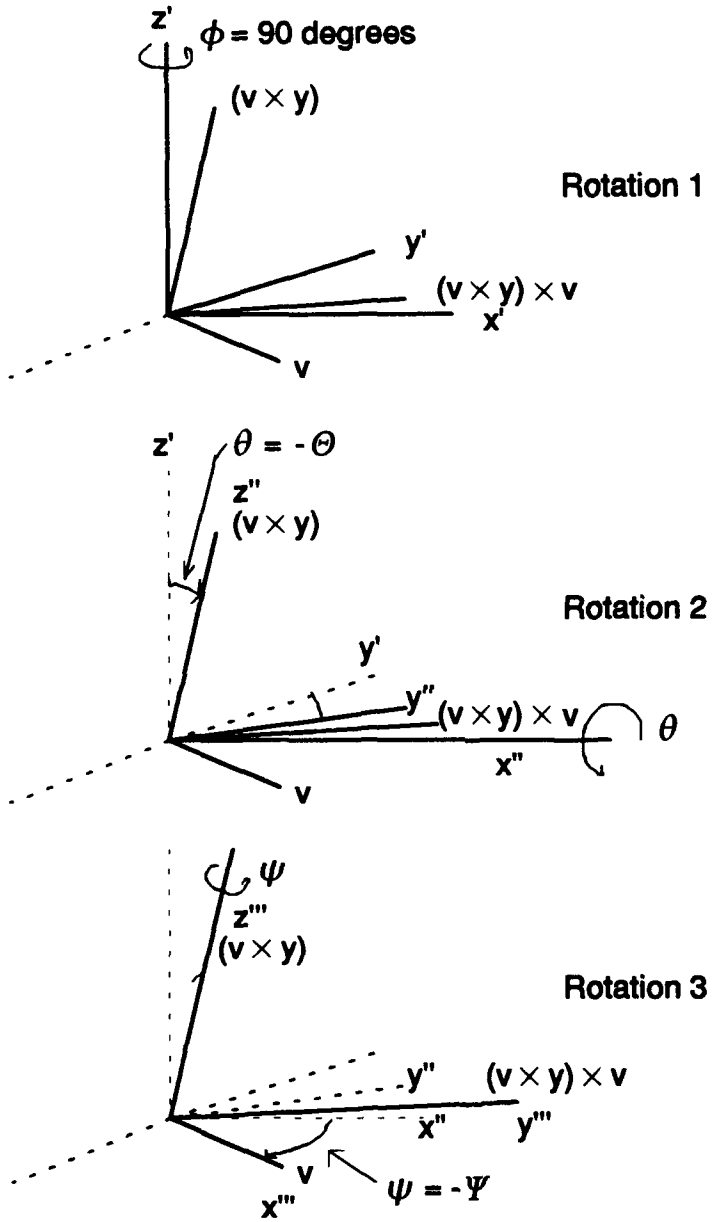

Figure 39. Three Rotations of the Transformation Matrix.

v, y and (vxy)xv are coplanar. First, we rotate counter clockwise about z so that our new x′ axis is where our original y axis was. Our first rotation angle is ϕ=90. Next, we rotate by $\theta = -\Theta$, measured counter clockwise about the x′ axis, so that our new z″ axis lines up with (vxy) and our new x″ and y″ axes lie in the plane with (vxy)xv and v. Finally, we rotate by $\psi = -\Psi$, measured counter clockwise about the z″ axis so that x‴ aligns with v and y‴ aligns with (vxy)xv.

With the rotations as outlined above, we have the following relationships:

$$\cos(\phi) = 0 \tag{82}$$

$$\sin(\phi) = 1 \tag{83}$$

$$\cos(\theta) = v_x (v_x^2+v_z^2)^{-1/2} \tag{84}$$

$$\sin(\theta) = -v_z (v_x^2+v_z^2)^{-1/2} \tag{85}$$

$$\cos(\psi) = v_y \tag{86}$$

$$\sin(\psi) = -(v_x^2+v_z^2)^{1/2} \tag{87}$$

For a particle scattering through the angles χ and φ of Figure 37, the new normalized velocity vectors in the particle frame are:

$$v_x' = \cos(\chi) \tag{88}$$

$$v_y' = \sin(\chi)\sin(\varphi) \tag{89}$$

$$v_z' = \sin(\chi)\cos(\varphi) \tag{90}$$

Using Equations (82) - (87) in Goldstein's inverse transformation matrix and applying it to the velocity vector defined by Equations (88)-(90), we arrive at

the following expressions for the components of the velocity vector in the laboratory frame:

$$V_x' = |V'|\left(v_x \cos(\chi) - \left(v_z \sin(\chi)\cos(\varphi) + v_x v_y \sin(\chi)\sin(\varphi) \right) \sqrt{v_x^2 + v_z^2}^{-1} \right) \quad (91)$$

$$V_y' = |V'|\left(v_y \cos(\chi) + \sqrt{v_x^2 + v_z^2} \sin(\chi)\sin(\varphi) \right) \quad (92)$$

$$V_z' = |V'|\left(v_z \cos(\chi) + \left(v_z \sin(\chi)\cos(\varphi) - v_y v_z \sin(\chi)\sin(\varphi) \right) \sqrt{v_x^2 + v_z^2}^{-1} \right)$$

References

1. Alves, M. V., V. Vahedi and C. K. Birdsall. "RF Plasma Processes in Cylindrical Models and Plasma Immersion Ion Implantation", Presented at the Thirty-First Annual Meeting of the APS Division of Plasma Physics (4U14), Anaheim, CA. 13-17 Nov 1989.

2. Andrews, J. G., and Allen, J. E., "Theory of a Double Sheath Between Two Plasmas." Proc. R. Soc. Lond., A. 320: 459-472. (1971).

3. Baksht, F. G., et al., Thermionic Converters and Low Temperature Plasma, Academy of Sciences of the USSR, English Edition by Laurin Hansen, DOE-tr-1. Springfield VA: National Technical Information Service/ U.S. Department of Commerce. 1978.

4. Birdsall, C. K. and A. B. Langdon. Plasma Physics Via Computer Simulation. Bristol, U.K.: Adam Hilger. 1991.

5. Birdsall, C.K., "Particle-in-Cell Charged-Particle Simulations, Plus Monte Carlo Collisions With Neutral Atoms, PIC-MCC." IEEE Transactions on Plasma Science, Vol. 19, No. 2: 65-85. (April 1992).

6. Britt, Ned. Vice President, Space Power Incorporated, Sunnyvale CA. Personal communication. Jan 1991. Repeated in Jan 1994.

7. Burden, R. L. and J. D. Faires. Numerical Analysis, Fourth Edition, Boston: PWS-Kent Publishing Company, 1989.

8. Burger, Peter. "Elastic Collisions in Simulating One-Dimensional Plasma Diodes on the Computer." The Physics of Fluids, Vol. 10, No.3: 658-666. (March 1967).

9. Cherington, B.E. Gaseous Electronics and Gas Lasers. Volume 94 of International Series on Natural Philosophy. New York: Pergamon Press. 1979.

10. Dawson, John M. "Thermal Relaxation in a One-Species, One-Dimensional Plasma," The Physics of Fluids Vol. 7 No. 3: 419-425. (March 1964).

11. Determan, William R. and Thomas H. Van Hagan. "Space Power Reactor In-Core Thermionic Multicell Evolutionary (S-PRIME) Design," American Institute of Physics Conference Proceedings 271, 10th Symposium on Space Nuclear Power and Propulsion. 1235-1240. 1993.

12. Emmert, G. A., R. M. Wieland, A. T. Mense and J. N. Davidson. "Electric Sheath and Presheath in a Collisionless, Finite Ion Temperature Plasma." Physics of Fluids, Vol. 23 No. 4: 803-812. (April 1980).

13. Golant, V. E, A. P. Zhilinsky and I. E. Sakharov. Fundamentals of Plasma Physics, New York: John Wiley and Sons, 1980.

14. Golant, V. E. , A. P. Zhilinsky and I. E. Sakharov. Fundamentals of Plasma Physics. New York: John Wiley & Sons, 1980

15. Goldstein, Herbert. Classical Mechanics. Second Edition. Reading, Mass: Addison-Wesley Publishing Company. 1980.

16. Hitchon, W.N.G. et al., "An Efficient Scheme for Convection-Dominated Transport." Journal of Computational Physics, No 83: 79-95. (1989).

17. Holt, E. H. and R. E. Haskell. Foundations of Plasma Dynamics, New York: The MacMillan Company, 1965.

18. Houts, Michael G., William R. Wharton Jr., Lester L. Begg, and Leo A. Lawrence. "The Thermionic Verification Program: Technical Progress and Future Plans," American Institute of Physics Conference Proceedings 271, 10th Symposium on Space Nuclear Power and Propulsion. 1225-1234. 1993.

19. IEEE Transactions on Plasma Science, Vol. 19, No. 2. (April 1991).

20. Kaibyshev, V.Z. et al. "Effect of a Third Electrode on a Low Voltage Arc." Soviet Physics - Technical Physics Vol 20 No 2: 203-207. (Feb. 1975).

21. Kaibyshev, V.Z. et al. "Use of the Thermionic Converter for Regulation of Current in Electric Circuits", Soviet Physics - Technical Physics Vol. 17, No 6: 1006-1009. (Dec. 1972).

22. Kaplan, V.B., et al. "Pulsed Control with a High-Current Low-Voltage Cesium-Barium Discharge." Soviet Physics - Technical Physics Vol. 22, No. 10: 1202-1207 (Oct. 1977).

23. Krall, N. A. and A. W. Trivelpiece. Principles of Plasma Physics, San Francisco: San Francisco Press, Inc., 1986.

24. Kuhn, S. "The Physics of Bounded Plasma Systems (BPS's): Simulation and Interpretation." Contrib. Plasma Physics Vol. 34 No. 4: 495-538 (1994).

25. Kurata, Mamoru. Numerical Analysis for Semiconductor Devices. Lexington, MA: Lexington Books. 1982.

26. Lamp, Thomas R. and Brian D. Donovan. "The Advanced Thermionics Initiative...Program Update." American Institute of Physics Conference Proceedings 271, 10th Symposium on Space Nuclear Power and Propulsion. 1219-1223. 1993.

27. Langmuir, I., "The Effect of Space Charge and Residual Gasses n Thermionic Currents in High Vacuum," Physical Review Vol. II, No. 6: 450-486. (Dec 1913).

28. Langmuir, I., "The Interaction of Electron and Positive Ion Space Charges in Cathode Sheaths," Physical Review, Vol. 33, No. 6: 140-175. (June 1929).

29. Lawless, J.L. and Lam, S.H., "An Analytical Model of Thermionic Discharge Plasmas," Journal of Applied Physics, Vol. 59, No. 6: 1875-1889. 15 March 1986.

30. Lawless, John Langee Jr. The Plasmadynamics and Ionization Kinetics of Thermionic Energy Conversion. PhD dissertation. Princeton University, Princeton N.J. 1981.

31. Lee, H. H., Brian R. Lewis, and Andrew C. Klein. "System Modeling for the Advanced Thermionic Initiative Single Cell Thermionic Space Nuclear Reactor," American Institute of Physics Conference Proceedings 271, 10th Symposium on Space Nuclear Power and Propulsion. 951-956. 1993.

32. Lewis, E. E. and W. F. Miller Jr. Computational Methods of Neutron Transport, New York: John Wiley and Sons, 1984.

33. Main, G. L. "Effects of Emitter Sheath Ion Reflection and Trapped Ions on Thermionic Converter Performance Using an Isothermal Electron Model", IEEE Transactions on Plasma Science, Vol. PS-15, No. 3: 309-318. (June 1987).

34. Main, G. L., et al. Advanced Thermionic Technology Initiative Program, Task 3A - Comprehensive Semi-3D Modeling of In-core Thermionic Converters. WL-TR-91-2078. Dayton, OH: Wright Laboratories. 27 Nov 1991.

35. Main, G. L., Ph.D. dissertation, Emitter Sheath Effects on Thermionic Convertor Performance, Princeton University, Princeton N.J. 1984.

36. McVey, J. B., G. L. Hatch, K. J. Greek, G. J. Parker, W. N. G. Hitchon, J. E. Lawler, and M. L. Ramalingam. Comprehensive Time Dependent Semi-3D Modeling of Thermionic Converters In-Core, Thermionic Analysis for the ATI Cylindrical Converter. WL-TR-93-2031. Dayton, OH: Wright Laboratories. 19 Mar 1993.

37. Morey, I. J., V. Vahedi and J. P. Verboncoeur. "Particle Simulation Code for Modeling Processing Plasmas," Presented at the Thirty-First Annual Meeting of the APS Division of Plasma Physics (4U14), Anaheim, CA. 13-17 Nov, 1989.

38. Morris, D. Brent. "The Thermionic System Evaluation Test (TSET): Description, Limitations, and the Involvement of the Space Nuclear Power Community," American Institute of Physics Conference Proceedings 271, 10th Symposium on Space Nuclear Power and Propulsion. 1251-1256. New York: American Institute of Physics. 1993.

39. Murray, C. S. Experimental and Theoretical Studies of a High Temperature Cesium-Barium Tacitron, with Application to Low Voltage-High Current Inversion. PhD dissertation. University of New Mexico, Albuquerque, NM, 1993

40. Nichols, Don F. "Space Nuclear Reactor Integration Study," Proceedings of the 25th Intersociety Energy Conversion Engineering Conference, Vol. 1: 94-99. 1990.

41. Nighan, William L. "Electron Transport Phenomena in Thermionic Converter Plasmas," IEEE Conference Record of the Thermionic Conversion Specialist Conference. 276-286. New York: IEEE, 1966.

42. Norcross, D. W. and P. M. Stone. "Recombination, Radiative Energy Loss and Level Populations in Nonequilibrium Cesium Discharges," J. Quant. Spectrosc. Radiat. Transfer , Vol. 8: 655-684. (1968).

43. Ponomarev-Stepnoi, N. N., V. A. Usov, V. P. Nickitin, B. G. Oglobin, J. I. Lutov, A. N. Lupov, V. N. Gabrusev, A. M. Klimov, J. V. Nicolaev, R. J. Kucherov, and S. A. Eremin. "Space Nuclear Power System Based on Thermionic Reactor with Single Cell TFE's and Zirconium Hydride Moderator," American Institute of Physics Conference Proceedings 271, 10th Symposium on Space Nuclear Power and Propulsion. 973-980. New York: American Institute of Physics. 1993.

44. Prewett, P. D. and Allen, J. E., "The Double Sheath Associated with a Hot Cathode," Proc. R. Soc. Lond. A. 348: 435-446. (1976).

45. Ramalingam, M. L. Advanced Thermionic Technology Initiative Program. Task 1, An intermediate Evaluation of Thermionic Technologies. WL-TR-92-2004. Dayton, OH: Wright Laboratories. 21 February, 1992.

46. Rasor, Ned S. "Chapter 5: Thermionic Energy Conversion" in Applied Atomic Collision Physics, Volume 5. Edited by H. Massey, E. McDaniel, and B. Bederson. New York: Academic Press, 1982.

47. Rasor, Ned S. "Thermionic Energy Conversion Plasmas," IEEE Transactions on Plasma Science, Vol. 19, No. 6: 1191-1208. (Dec 1991).

48. Schwager, L. A. and C. K. Birdsall. "Collector and Source Sheaths of a Finite Ion Temperature Plasma," Physics of Fluids B. Vol. 2 No. 5: 1057-1068. (May 1990).

49. Shaw, David Tai-Ko. "Analysis of the Electron Energy Distribution Function in an Ignited Thermionic Converter," IEEE Conference Record of the Thermionic Conversion Specialist Conference. 298-305. New York: IEEE, 1966.

50. Sommerer, T. J. "Models of Low Pressure Plasma-Aided Materials Processing," AIAA 23rd Plasmadynamics and Lasers Conference, AIAA92-3017, Washington: AIAA, 1992.

51. Vender, David and Rod. W. Boswell. "Numerical Modeling of Low-Pressure RF Plasmas," IEEE Transactions of Plasma Science, Vol. 18, No. 4: 725-731. (August, 1990).

52. Verboncoeur, J. P. et al. PDP1, PDC1, PDS1 Plasma Device 1 Dimensional Bounded Electrostatic Codes Reference Manual, version 2.0, Berkeley, CA: Regents of University of California, 1990.

53. Warner, Charles. "A Theory of the Ignited Mode," IEEE Conference Record of the Thermionic Specialist Conference. 269-275. New York: IEEE, 1966.

54. Warner, Charles. "Theoretical Considerations of the Ignited Mode," Second International Conference on Thermionic Electrical Power Generation. 931-942. Euratom Center for Information and Documentation, 1968.

Vita

Captain Don F. Nichols was born in Arlington, Virginia on 8 July 1957. In 1981 he enlisted in the United States Air Force and served for three years as an aircraft mechanic at Lakenheath, England. In 1984, he was selected for the Airman Education and Commissioning Program, and three years later was awarded a B. S. in nuclear engineering "with high distinction" by the Pennsylvania State University. After graduating from Officer Training School, he attended the Air Force Institute of Technology, graduating as an honor graduate, with a M. S. in nuclear engineering in 1989. At graduation, he received the Commandant's Award for scholarship and thesis performance and the Mervin Gross Award for overall academic achievement. Following graduation, he served in the Space Power Branch of the Air Force Weapons Laboratory (now part of the Phillips Laboratory), where his duties included overseeing the Air Force's investment in the Thermionic Fuel Element Verification Program, in-house nuclear reactor modeling, determining Air Force requirements for space nuclear power systems, and managing the development of space nuclear reactor simulation codes. He entered the doctoral program of the Air Force Institute of Technology School of Engineering in 1991.

Permanent Address: 216 Meadowbrook Dr.
New Wilmington, PA 16142

September 1994 Doctoral Dissertation

A THREE REGION ANALYSIS OF A BOUNDED PLASMA USING PARTICLE IN CELL AND FLUID TECHNIQUES

Don F. Nichols, Captain, USAF

Air Force Institute of Technology, WPAFB OH 45433-6583 AFIT/DS/ENP/94-03

Dr. Frank Thome
NMERI/TOPAZ
901 University Blvd. S.E.
Albuquerque, NM 87106

Approved for public release; distribution unlimited

A detailed collisionless sheath theory and a three-region collisional model of a bounded plasma are presented, and the suitability of the collisional model for analysis of ignited mode thermionic converters is investigated. The sheath theory extends previous analyses to regimes in which the sheath potential and electron temperatures are comparable in magnitude. In all operating regimes typical of an ignited mode thermionic converter, the predicted sheaths extend several mean-free paths. The apparent collisionality of the sheaths prompted development of a collisional, three-region model of the converter plasma. By interfacing Particle-in-Cell regions (for the sheaths) and fluid regions (for the bulk of the plasma), a time-dependent, wall-to-wall model of the plasma in the inter-electrode space is created. The components of the model are tested and validated against analytic solutions and against one another, then applied to the analysis of an ignited mode thermionic converter. Under ignited mode operating conditions, the electron velocity distribution at the plasma/sheath boundary is found to be inconsistent with that assumed in the model development, and the calculation diverges. The observed distribution is analyzed and a new basis set of distribution functions is suggested that should permit application of the hybrid model to ignited mode thermionic converters.

Cesium, Hybrid Simulation, Computerized Simulation, Thermionic Converters			219
Unclassified	Unclassified	Unclassified	UL

GENERAL INSTRUCTIONS FOR COMPLETING SF 298

The Report Documentation Page (RDP) is used in announcing and cataloging reports. It is important that this information be consistent with the rest of the report, particularly the cover and title page. Instructions for filling in each block of the form follow. It is important to **stay within the lines to meet optical scanning requirements.**

Block 1. Agency Use Only (Leave Blank)

Block 2. Report Date. Full publication date including day, month, and year, if available (e.g. 1 Jan 88). Must cite at least the year.

Block 3. Type of Report and Dates Covered. State whether report is interim, final, etc. If applicable, enter inclusive report dates (e.g. 10 Jun 87 - 30 Jun 88).

Block 4. Title and Subtitle. A title is taken from the part of the report that provides the most meaningful and complete information. When a report is prepared in more than one volume, repeat the primary title, add volume number, and include subtitle for the specific volume. On classified documents enter the title classification in parentheses.

Block 5. Funding Numbers. To include contract and grant numbers; may include program element number(s), project number(s), task number(s), and work unit number(s). Use the following labels:

C	- Contract	**PR**	- Project
G	- Grant	**TA**	- Task
PE	- Program Element	**WU**	- Work Unit Accession No.

Block 6. Author(s). Name(s) of person(s) responsible for writing the report, performing the research, or credited with the content of the report. If editor or compiler, this should follow the name(s).

Block 7. Performing Organization Name(s) and Address(es). Self-explanatory.

Block 8. Performing Organization Report Number. Enter the unique alphanumeric report number(s) assigned by the organization performing the report.

Block 9. Sponsoring/Monitoring Agency Names(s) and Address(es). Self-explanatory.

Block 10. Sponsoring/Monitoring Agency. Report Number. (If known)

Block 11. Supplementary Notes. Enter information not included elsewhere such as: Prepared in cooperation with...; Trans. of ..., To be published in .... When a report is revised, include a statement whether the new report supersedes or supplements the older report.

Block 12a. Distribution/Availablity Statement. Denote public availability or limitation. Cite any availability to the public. Enter additional limitations or special markings in all capitals (e.g. NOFORN, REL, ITAR)

DOD	- See DoDD 5230.24, "Distribution Statements on Technical Documents."
DOE	- See authorities
NASA	- See Handbook NHB 2200.2.
NTIS	- Leave blank.

Block 12b. Distribution Code.

DOD	- DOD - Leave blank
DOE	- DOE - Enter DOE distribution categories from the Standard Distribution for Unclassified Scientific and Technical Reports
NASA	- NASA - Leave blank
NTIS	- NTIS - Leave blank.

Block 13. Abstract. Include a brief (Maximum 200 words) factual summary of the most significant information contained in the report.

Block 14. Subject Terms. Keywords or phrases identifying major subjects in the report.

Block 15. Number of Pages. Enter the total number of pages.

Block 16. Price Code. Enter appropriate price code (NTIS only).

Blocks 17. - 19. Security Classifications. Self-explanatory. Enter U.S. Security Classification in accordance with U.S. Security Regulations (i.e., UNCLASSIFIED). If form contains classified information, stamp classification on the top and bottom of the page.

Block 20. Limitation of Abstract. This block must be completed to assign a limitation to the abstract. Enter either UL (unlimited) or SAR (same as report). An entry in this block is necessary if the abstract is to be limited. If blank, the abstract is assumed to be unlimited.